Universidade de Aveiro Departamento de Física
2017

Sandra Filipa Henriques Correia

Materiais híbridos orgânicos-inorgânicos para fotónica sustentável: concentradores solares luminescentes

Organic-inorganic hybrid materials for green photonics: luminescent solar concentrators

Universidade de Aveiro Departamento de Física
2017

Sandra Filipa Henriques Correia

Materiais híbridos orgânicos-inorgânicos para fotónica sustentável: concentradores solares luminescentes

Organic-inorganic hybrid materials for green photonics: luminescent solar concentrators

Dissertação apresentada à Universidade de Aveiro para cumprimento dos requisitos necessários à obtenção do grau de Doutor em Física, realizada sob a orientação científica da Doutora Maria Rute de Amorim e Sá Ferreira André, Professora Associada com Agregação do Departamento de Física da Universidade de Aveiro, do Doutor Luís António Ferreira Martins Dias Carlos, Professor Catedrático do Departamento de Física da Universidade de Aveiro e do Doutor Paulo Sérgio de Brito André, Professor Associado com Agregação do Departamento de Engenharia Eletrotécnica e de Computadores do Instituto Superior Técnico da Universidade de Lisboa.

Trabalho desenvolvido no âmbito do projeto CICECO-Instituto de Materiais de Aveiro, POCI-01-0145-FEDER-007679 (UID/CTM/50011/2013), e Instituto de Telecomunicações (UID/EEA/50008/2013), financiado por fundos nacionais através do FCT/MEC e cofinanciado pelo FEDER sob o acordo PT2020. O autor agradece o apoio financeiro dado pela FCT através da bolsa SFRH/BD/91263/2012.

Aos meus pais.

o júri

presidente

Prof. Doutor Manuel João Senos Matias
professor catedrático da Universidade de Aveiro

Prof. Doutor Jorge Manuel Ferreira Morgado
professor catedrático do Instituto Superior Técnico da Universidade de Lisboa

Prof. Doutora Maria Rute de Amorim e Sá Ferreira André
professora associada com agregação da Universidade de Aveiro

Doutor José Manuel de Nunes Vicente Rebordão
investigador coordenador da Faculdade de Ciências da Universidade de Lisboa

Prof. Doutor Manuel Joaquim Bastos Marques
professor auxiliar da Faculdade de Ciências da Universidade do Porto

Prof. Doutor João Pedro Santos Hall Agorreta de Alpuim
professor auxiliar da Universidade do Minho

agradecimentos

A primeira palavra de agradecimento é dirigida aos meus orientadores, Professora Maria Rute André, Professor Luís Carlos e Professor Paulo André, pela oportunidade que me deram, pela ajuda e disponibilidade ao longo dos últimos quatro anos.
À Doutora Patrícia Lima pelo auxílio no laboratório e pela síntese dos materiais utilizados.
Ao Mestre João Prata pelo apoio técnico e ao Doutor Paulo Antunes pela disponibilidade.
Ao Professor Sidney Ribeiro e ao Doutor Édison Pecoraro pela ajuda e hospitalidade, enquanto estive em Araraquara. Ao César Polachini pela ajuda técnica no fabrico de fibra ótica.
A todos os meus colegas do Grupo dos Híbridos Funcionais que, de uma forma ou de outra, contribuíram para o desenvolvimento deste trabalho.
Um agradecimento especial à Vânia Freitas e à Ana Rita Frias pela constante companhia e ajuda.
À Fundação para a Ciência e Tecnologia pela ajuda financeira.
À Graça pela companhia e amizade.
Ao Sérgio pela compreensão, companheirismo e paciência.
A todos os meus amigos que me acompanharam neste processo, em especial, à Marília por ser a amiga de todas as horas e à Rita pelas tão necessárias doses de autoestima.
O agradecimento mais importante é dirigido à família, em especial aos meus pais, avós, Joana e Dalila pela presença e apoio.

A todos, muito obrigada!

palavras-chave

Híbridos orgânicos-inorgânicos, concentradores solares luminescentes, fibra ótica de plástico, corantes orgânicos, iões lantanídeos.

resumo

Os concentradores solares luminescentes são dispositivos de baixo custo que têm como objetivo aumentar a eficiência de células fotovoltaicas e promover a integração de dispositivos fotovoltaicos em elementos do dia-a-dia, tornando possível a captura de energia solar, através da fachada de edifícios, mobiliário urbano ou em têxteis. Geralmente, consistem numa matriz transparente coberta ou dopada com centros óticos ativos, capazes de absorver a radiação solar incidente e reemiti-la com um comprimento de onda específico que será transportada, através de reflexão interna total, para as extremidades da matriz onde se encontra(m) a(s) célula(s) fotovoltaica(s). O principal objetivo deste trabalho consiste na produção de concentradores solares luminescentes cuja camada ótica ativa é baseada em materiais híbridos orgânicos-inorgânicos dopados com iões lantanídeos (európio, Eu^{3+}) ou corantes orgânicos, nomeadamente, Rodamina 6G e Rodamina 800. A Rodamina 800, ao contrário dos iões de európio e da Rodamina 6G que emitem na gama do visível, emite na região espetral do infravermelho próximo (NIR), que se revela uma vantagem quando a célula fotovoltaica em uso é composta de silício cristalino, cuja gama de maior eficiência é no NIR. Neste trabalho, apesar de serem abordados concentradores solares luminescentes com geometria planar, o principal foco é a utilização da geometria cilíndrica. Este tipo de geometria permite que o efeito de concentração seja superior, relativamente à geometria planar, uma vez que a razão entre a área exposta e a área das extremidades é aumentada. A geometria cilíndrica é explorada, através da produção de concentradores solares luminescentes com base em fibra ótica polimérica (plástica) em que a camada ótica ativa se encontra no exterior (como um revestimento) ou no interior (como um preenchimento do núcleo oco). Além disso, a possibilidade de aumentar a área exposta foi, também, abordada com o fabrico de uma matriz de concentradores solares luminescentes colocados lado a lado e, também, com o fabrico de concentradores solares luminescentes na escala do metro.

keywords

Organic-inorganic hybrids, luminescent solar concentrators, plastic optical fibre, organic dyes, lanthanide ions.

abstract

Luminescent solar concentrators are inexpensive devices that aim to increase the efficiency of photovoltaic cells and promote the urban integration of photovoltaic devices, with unprecedented possibilities of energy harvesting through the façade of buildings, urban furniture or wearable fabrics. Generally, they consist of a transparent matrix coated or doped with active optical centres that absorb the incident solar radiation, which is re-emitted at a specific wavelength and transferred by total internal reflection to the edges where the photovoltaic cells are located. The main objective of this work is the production of luminescent solar concentrators whose optically active layer is based on organic-inorganic hybrid materials doped with europium ions or organic dyes, in particular, Rhodamine 6G and Rhodamine 800. Rhodamine 800, as opposed to europium ions and Rhodamine 6G which emit in the visible range, emits in the near infrared (NIR) range, which is an advantage for crystalline Si-based photovoltaic cells, whose efficiency is greater in the NIR. In this work, although the luminescent solar concentrators with planar geometry are addressed, the main focus is the use cylindrical geometry. The use of this type of geometry allows the effect of concentration to be higher relative to the planar geometry, since the ratio between the exposed area and the area of the edges is increased. The cylindrical geometry is exploited by producing luminescent solar concentrators based on polymer optical fibre (plastic) where the optically active layer is on the outside (as a coating) or inside (as a filling in the hollow core) of the optical fibre. Furthermore, the possibility of increasing the exposed area was also dealt with the production of bundles of luminescent solar concentrators in which the plastic optical fibres are placed side by side and, also, by fabricating luminescent solar concentrators with length in the metre scale.

Index

List of acronyms and symbols

A	Absorbance	**c-Si**	Crystalline silicon
α	Absorption coefficient	**Γ**	Damping factor
η_{abs}	Absorption efficiency	**d**	Diameter
λ_{abs}	Absorption range	**DC**	Down-conversion
$I_{AM1.5G}$	AM1.5G spectrum intensity	**DS**	Down-shifting
a-Si	Amorphous silicon	**DSL**	Down-shifting layer
α_{at}	Attenuation coefficient of the LSC	A_e	Edge surface area
η_{solar}	Average efficiency of the photovoltaic cell relatively to the total solar spectrum	L_c	Effective length
η_{PV}	Average responsivity value of the photovoltaic cell with respect to the total solar spectrum	L_s	Effective solar irradiation path length in the atmosphere
M4	Bipyridine-based bridged silsesquioxane	P_e	Electrical power ratio
e	Charge of the electron	λ_p	Emission peak position
F	Concentration factor	η_{yield}	Emission quantum yield
η_{sf}	Conversion efficiency	**C**	Emission ratio
θ_c	Critical angle	I_{em}	Emission spectrum intensity

E_v	Energy of the incident photons	**LPLSC**	Linearly polarized luminescent solar
I_x	Excitation spectrum intensity	η_{LDS}	Luminescent DS efficiency
EQE	External quantum efficiency	**LSC**	Luminescent solar concentrator
FWLSC	Fibre waveguiding luminescent solar concentrator	**LR305**	Lumogen Red 305
FF	Fill factor	**NP**	Nanoparticle
FT-ATR	Fourier Transform – Attenuated Total reflectance	**NREL**	National Renewable Energy Laboratory
FT-IR	Fourier Transform – Infrared Spectroscopy	**NIR**	Near Infrared
ω	Frequency	V_0	Open-circuit voltage
R	Fresnel reflection coefficient	η_{opt}	Optical conversion efficiency
fwhm	Full-width-at-half-maximum	**ORMOCER**	Organically modified ceramic
G	Geometrical gain	**ORMOSIL**	Organically modified silicate
ε_∞	High frequency relative dielectric constant	ω_0	Oscillator resonant frequency
P_{in}	Incident optical power	d_{out}	Outer diameter
λ_i	Incident wavelength	P_{out}	Output optical power
IR	Infrared	**PTMS**	Phenyltrimethoxysilane
d_{in}	Inner diameter	**PV**	Photovoltaic
O	Overlap integral	**POF**	Plastic optical fibre
ICPTES	Isocyanate-propyl-triethoxysilane	**PVA**	Poly(vinylalcohol)
L	Length	**PC**	Polycarbonate

p-Si	Polycrystalline silicon	ΔI_{SC}^{L}	Temporal relative variation of the short-
PDMS	Polydimethylsiloxane	**F5**	Tetracarboxamide-based organic-inorganic hybrid
PMMA	Polymethylmethacrylate	**THF**	Tetrahydrofuran
PS	Polysiloxane	**t**	Thickness
PCE	Power conversion efficiency	L_A	Thickness of the atmosphere
P_0	Power value at the shortest distance	A_s	Top surface area
η_{PV}	PV cell efficiency at λ_p	**TIR**	Total internal reflection
P567	Pyrromethene	η_{tr}	Transport efficiency
QD	Quantum dot	η_{trap}	Trapping efficiency
Δn	Refractive index contrast	**TOP**	Trioctyl phosphine
n_i	Refractive index of the emitting medium at λ_i	**tU5**	Tri-ureasil hybrid matrix
n_p	Refractive index of the emitting medium at λ_p	**UV**	Ultraviolet
R_{PV}	Responsivity of the PV cell at λ_p	**UC**	Up-conversion
Rh6G	Rhodamine 6G	**UCL**	Up-converting layer
Rh800	Rhodamine 800	**UPTES**	Ureapropyltriethoxysilane
η_{SA}	Self-absorption efficiency	**Vis**	Visible
Isc	Short-circuit current	**phen**	1,10-phenanthroline
Jsc	Short-circuit current density	**bpeta**	1,2-bis(4-pyridil) ethane
ε_s	Static relative dielectric constant	**dpbt**	2-(N,N-diethylanilin-4-yl)-4,6-bis(3,5-
η_{Stokes}	Stokes efficiency	**tta**	2-thenoyltrifluoroacetone

GLYMO	3-glycidoxypropyltrimethoxysilane
DCJTB	4-(dicyanomethylene)-2-t-butyl-6-(1,1,7,7-tetramethyljulolidyl-9-enyl)-4H-pyran
btfa	4,4,4-trifluoro-1-phenyl-1,3-butanedione
ephen	5,6-epoxy-5,6-dihydro-[1,10] phenanthroline
q	$^5D_0$ quantum efficiency

Chapter 1. Introduction

1.1 Context and state of the art

The increase in the world's population and the growing demand for comfort have caused an enormous increment in energy consumption over the last 150 years (Figure 1.1), making the depletion of fossil fuels predictable in the midterm [1]. It is, then, imperative to use alternative forms of energy, namely natural and renewables ones to minimize CO_2 emissions.

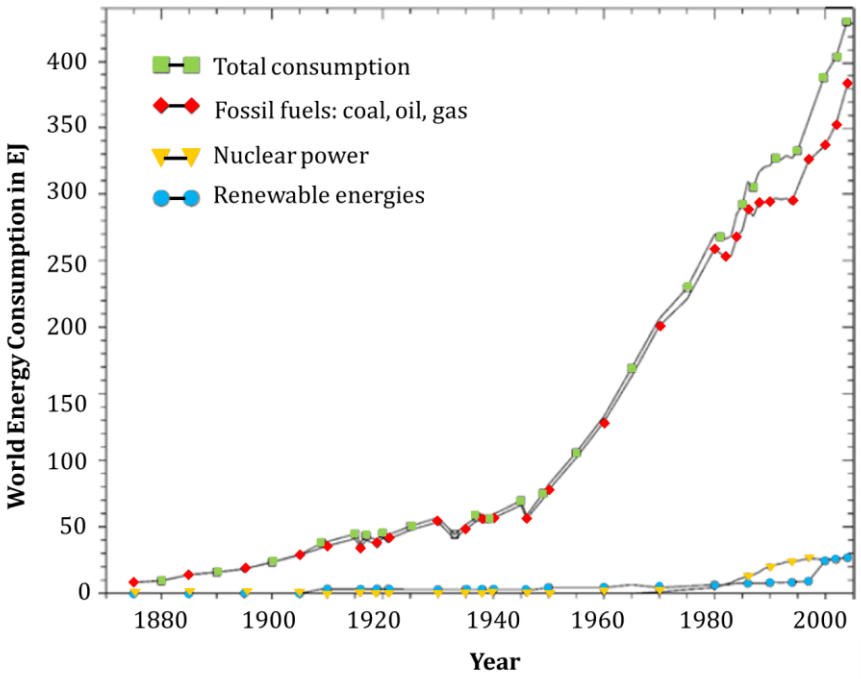

Figure 1.1 *World's energy consumption in EJ (10^{18} Joule) as a function of time [1].*

Solar energy has great potential compared with other energy sources, since solar irradiation on Earth is 14 000 times higher than world's energy consumption and, if stored for a year, it becomes superior to the energy delivered by any of the fossil fuels [1]. Thus, harvesting sunlight energy through photovoltaic (PV) technologies is an encouraging approach to produce the huge amount of electricity required to face the expected growth of comfort and mobility levels of the world's population [2-4]. Despite the development of PV systems over the last decades (Figure 1.2), the conversion of solar energy into electricity is not efficient enough and cost-competitive yet [2].

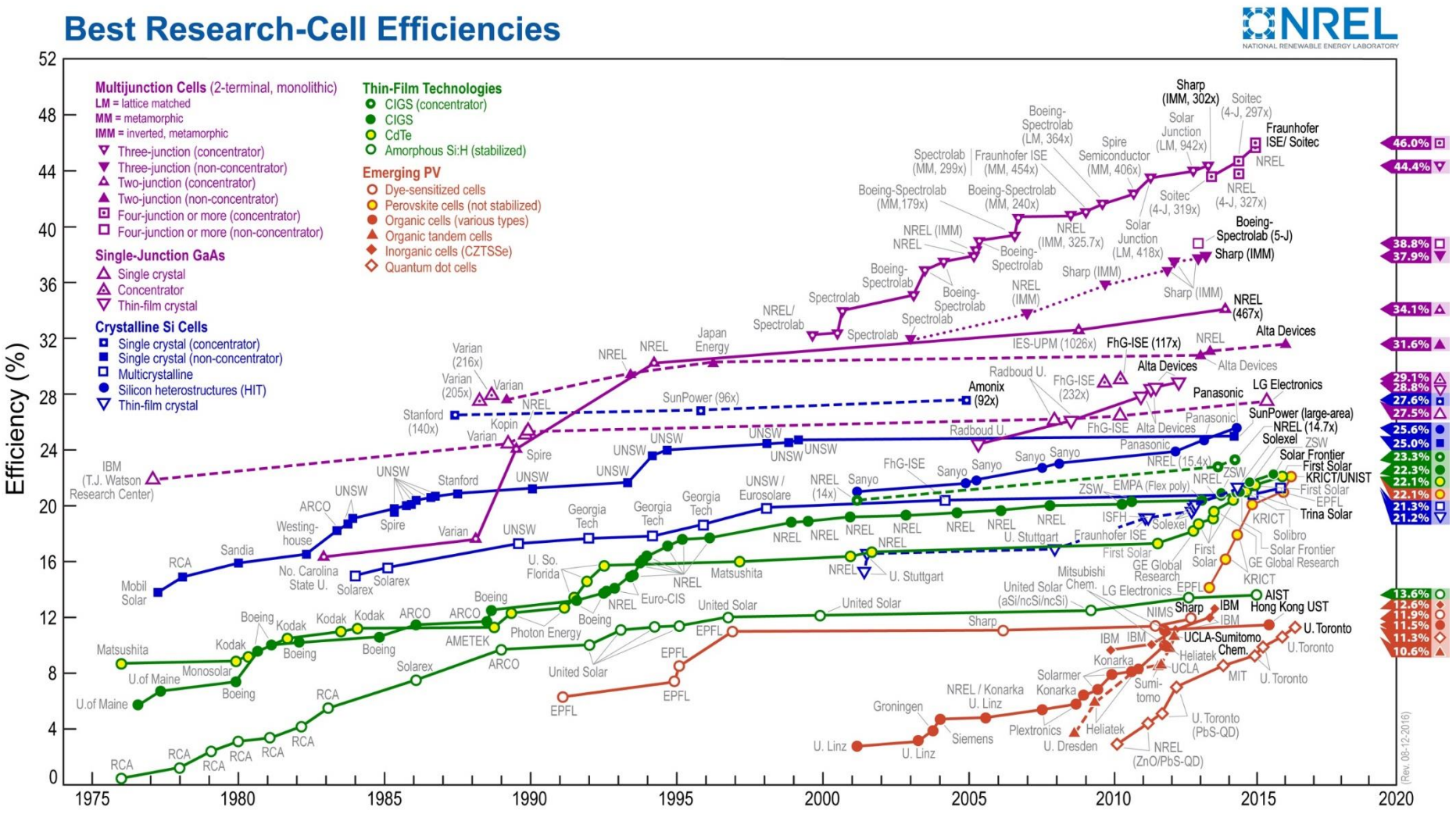

Figure 1.2 *PV cells efficiency values evolution over the last years. Source:* NREL – *National Renewable Energy Laboratory [5].*

The most efficient PV cells are based on III-V semiconductors [3], such as GaAs with power conversion efficiency (*PCE*, which is a ratio between the output electrical power and the input optical power, taking into account the PV cell features) of ~29 % [6] and multi-layered structures of GaAs, GaInP, InGaAs, GaInNAs and Ge (*PCE* values of up to ~46 %) that are, however, too expensive to become competitive [6]. Although presenting lower *PCE*, the most common PV cells are based on single crystalline Si (c-Si), polycrystalline Si (p-Si) and amorphous Si (a-Si) (*PCE* values of ~28, ~21 and ~10 %, respectively) [3,6]. All-organic and dye-sensitized PV cells are emerging classes that have the potential to compete with Si-based ones in terms of *PCE* under diffuse light conditions, which is a significant advantage for integration in urban buildings [7]. These cells still, however, display low *PCE* values (maximum of ~12 %) and high fabrication cost, compared to the Si-based cells. It is worth noting the emerging field of perovskite PV cells. Over the last years, perovskite PV cells have gained visibility due to unprecedented increase in its *PCE* values in such a short period of time (~6 years) [8,9]. Although not presented in the NREL chart (Figure 1.2), the 25.5 % world record for a tandem PV cell composed by perovskite and silicon was recently reported by a research group in Hong Kong Polytechnic University [10,11].

Let us focus our attention on the c-Si PV cells, because they are the most common in commercial PV systems, the *PCE* values of which are nowadays very close to the theoretical maximum established by the Shockley-Queisser limit of ~33 % [12]. One of the major factors limiting the *PCE* is the mismatch between the solar spectrum and the Si response curve [2].

Figure 1.3 shows the standard solar irradiance spectrum given as AM1.5G, where *G* stands for global sun, including both direct and diffuse light, AM stands for air mass and 1.5 is the ratio between the effective solar irradiation path length (L_S) in the atmosphere and that corresponding to a vertical position of the sun (considering the thickness of the atmosphere as L_A). For an incident angle θ relative to the normal of the Earth's surface and an irradiation of 1000 W·m^{-2} (1 sun) [3]:

$$\frac{L_S}{L_A} = \frac{1}{\cos\theta} \tag{1.1}$$

The AM coefficient varies with latitude, time of the day and season of the year. The AM1.5 values correspond to an angle of 48.2 º, which is characteristic of temperate latitudes, where most of the world urban populations live. The AM1.5G is the standard spectrum considered when evaluating the PV cells performance. AM0 describes the solar spectrum outside the

atmosphere, which is the irradiance of a 5800 K black body and it is about 28 % more intense than AM1.5G [3]. Figure 1.3 also shows the fractions of the total energy available for down-conversion (DC) and/or down-shifting (DS) (~16 %) and up-conversion (UC) processes (~17 %). In DC, one high-energy photon absorbed (typically in the UV-Vis region) is converted in two lower-energy photons (typically in the Vis-IR regions); DS is a single photon process that involves transformation of one absorbed high-energy photon into one lower-energy photon; in UC, one high-energy photon (typically in the UV-Vis regions) is emitted after excitation of the sample by two (or more) low-energy photons (typically in the IR region) [2].

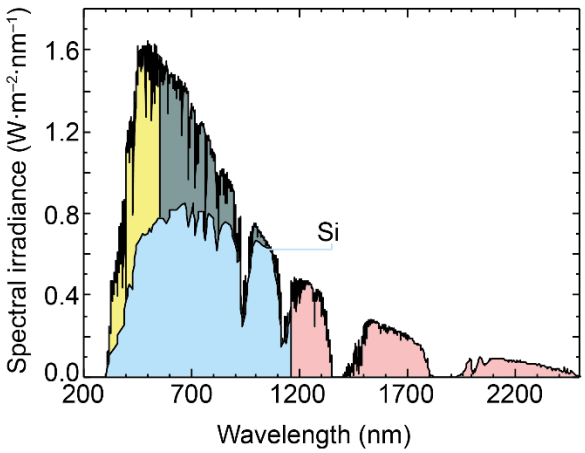

Figure 1.3 *Air-Mass 1.5G (AM1.5G) solar irradiance spectrum. The shadowed areas represent the available fraction for down-conversion (26 %, up to 550 nm), down-shifting (81 %, up to 1100 nm) and up-conversion (16 % in the 1200-2500 nm range) processes for a c-Si wafer. The fraction absorbed by a thick c-Si wafer [13] is also displayed.*

The claimed improvements in the conversion yield of Si-based cells obtained by altering the cell architecture with trivalent lanthanide ions (Ln^{3+})-containing materials range from 0.3 to 2.0 % (Table 9 of Bünzli and Chauvin [3]). Another drawback that limits the PV cells efficiency and the effective usage of the remaining solar energy is the fact that sunlight exists in a diffuse non-concentrated form, requiring the usage of large mirrors to track the solar energy and direct the radiation to the cell. Besides increasing the cost, these mirrors are often large, demanding additional cooling, and the assembly must be done with care to avoid shadowing regions in the cell [16]. For all the mentioned reasons, further increasing the PV cells efficiency without external devices would be very difficult.

One way to cope with the above mentioned problems is through the usage of luminescent solar concentrators (LSCs). LSCs consist of a film (or layer) containing optically active centres, that, when exposed to light, converts part of the absorbed radiation into a specific emitting

wavelength. Part of the emitted signal will be lost at the surface (as detailed in section 3.1) and the remaining light will be trapped inside the layer and guided to the edges through total internal reflection (TIR), where it can be collected by a PV cell (Figure 1.4). This process endows a LSC with the ability of concentrating the maximum amount of light energy at its edges for electrical power generation. The light available at the edges of a LSC depends on:

- The total surface area of the layer;
- The total amount of incident light collected on the layer;
- The type of layer;
- The emission quantum yield of the active species.

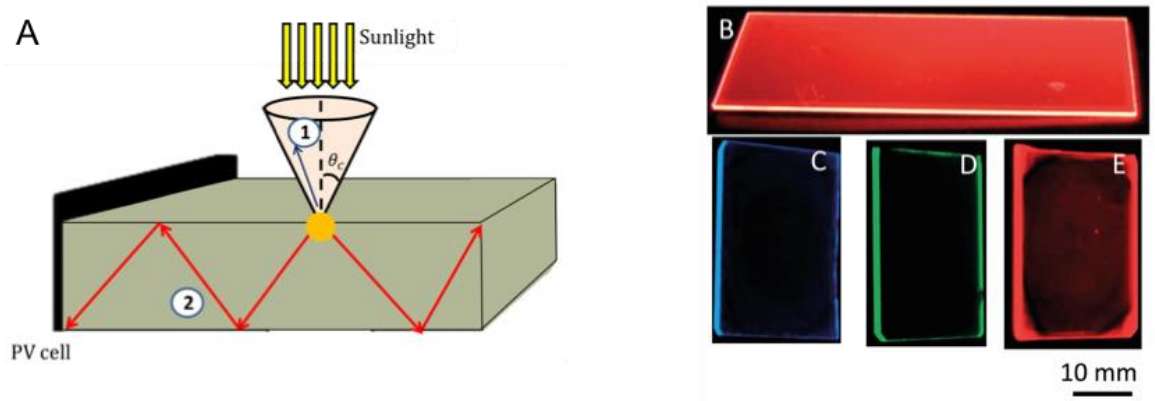

Figure 1.4 *(A) Schematic 3D view of a luminescent solar concentrator: sunlight is incident on the top. The radiation is absorbed by the optically active centre, and its re-emitted radiation is spatially random. Part of the emission is lost through the escape cone (1) and the remaining is guided by total internal reflection until it reaches the PV cell on the edge (2). Extracted from ref. [212]. Photographs of some LSCs under UV irradiation (365 nm) based on (B) a di-ureasil organic-inorganic hybrid doped with* $Eu(btfa)_3(MeOH)_2 \cdot bpeta$, *(*$btfa^-$*=4,4,4-trifluoro-1-phenyl-1,3-butanedione,* $bpeta^-$*=1,2-bis(4-pyridil)ethane, MeOH=methanol) and on bipyridine-based bridged silsesquioxanes (C) lacking metal activator centres and doped with (D)* Tb^{3+} *and (E)* Eu^{3+} *ions.*

Different optically active centres have been tested in LSCs, including organic dyes [16-30], quantum dots (QDs) [31-48], Ln^{3+} ions [49-62] and, recently, metal halide clusters [63]. Moreover, the usage of LSCs boosts the reduction of the area of the PV cell (with the consequent reduction of the amount of material used), decreasing, therefore, the cost associated with energy PV conversion [64]. Nevertheless, it is estimated that LSCs will only be economically viable if the cost per generated electrical power can be reduced to about 1€/Watts-peak, meaning that the ratio between the cost of the LSC itself and the cost of the PV material in use should be <1/5 [65].

Despite the simple mechanism behind the LSC working principle, several factors must be taken into consideration while designing efficient devices. The first issue is related with the type of the target PV cell, in particular the energy band gap of the material that is used to produce the PV cell. The knowledge of the material band gap will determine both the sunlight wavelength region not absorbed by the PV cell and the wavelength emission range of the LSC emissive layer. To be effective in this application, the optically active centres in the emissive layer should present [66]:

- Broad spectral absorption;
- High absorption efficiency over the whole absorption spectrum;
- Large Stokes shift;
- High luminescence efficiency (emission quantum yield);
- Emission energy resonant with the PVcell responsivity (input–output gain).

In the past decade, Ln^{3+}-based materials have been considered good candidates for application in LSCs due to an appropriate balance between relatively high emission quantum yield values (η_{yield}>0.30 [67]) and negligible self-absorption (quantified by the self-absorption efficiency, η_{SA} ~1).

The first LSCs (initially termed as fluorescent/luminescent collectors) reported by W. Weber and J. Lambe in 1976, included active layers of Nd^{3+}- or Rhodamine 6G (Rh6G)-doped glasses [18]. This work was followed by the theoretical study of A. Goetzberger and W. Greubel pointing out that concentration factors (ratio between the light emitted at surface and guided to the edges) around 100 appeared feasible [68]. In the following year, R. Reisfeld and S. Neuman announced the fabrication of LSCs made of uranyl-doped glass [69] whose performance was later improved by R. Reisfeld and Y. Kalisky in 1980 through the incorporation of Nd^{3+} and Ho^{3+} ions [70]. The presence of the Ln^{3+} ions induced an increased conversion efficiency with respect to that observed in LSCs based solely on uranyl-doped glass [69] because the energy absorbed by the uranyl group could be efficiently transferred to the Nd^{3+} and Ho^{3+} ions that emit in the near infrared (NIR) spectral range, closer to the maximum sensitivity of the c-Si PV cells [70]. Transition metal utilization, such as trivalent chromium and manganese, was reviewed by Reisfeld and Jørgensen [71] and Reisfeld [72] in the 1980s.

A substantial increase in the LSCs research occurred over the past three decades, with the major advances of the field highlighted in several reviews published in the last years. Key concepts related with loss sources (*e.g.* reabsorption and escape cone) and the role of long term

photostability, a crucial issue common to distinct optical species, was discussed by B. Rowan *et al.* [73]. Another approach pointed out is the usage of NIR emitting QDs, despite the low intrinsic emission quantum yields which are still a severe drawback. According to these authors, challenges for organic-inorganic hybrids are envisaged, because it is unlikely that a single organic or inorganic material can overcome the losses issues and, so, the integration of the positive characteristics of each one into a hybrid material would be considerably more attractive [73].

The optical losses associated with a LSC were further reviewed in more recent works. For instance, R. Reisfeld [74], reported the use of an organic-inorganic hybrid ORMOCER matrix to incorporate luminescent dyes in order to enhance the dye optical properties, namely reduce the reabsorption and increase the photostability. Other works discussed the possibility of maximising the light trapped inside the substrate through the application of selective mirrors that will reflect the light emitted at the surface back inside the substrate [66]. Photonic structures constructed at the surface of the LSC were also employed to increase the trapping efficiency [74]. The increase of the emission quantum yield was also discussed by using plasmonic structures [30,66].

Several other works focused on the emitting species. For example, a review on the role of QDs as emitting species for LSC applications emphasized that the low quantum yields measured in organic matrices, large emission-absorption overlaps, unknown photostability and toxicity are still relevant issues to be addressed [33]. The incorporation of multiple stacks in which organic (dyes) and inorganic (QDs) species are joint together may result in an enlargement of the absorption range to achieve *PCE* values well above 10 % [65]. J.-C. G. Bünzli and A.-S. Chauvin [3] reviewed the work done on the role of Ln^{3+} in PV systems. The energy conversion mechanisms are explained and their role in improving the solar energy conversion efficiency described and proven. A quantitative general assessment is made predicting that improvements on the order of 5 % in conversion yield are feasible [3].

Despite the potential for generating low-cost solar power, LSC development faces various challenges, most of which related to the materials used in their design [73], and various authors (even since the very beginning of the field [71]) concluded that the combination of organic and inorganic counterparts into single hybrid materials should play a key role on the design optimization [3,73,74].

The term 'organic-inorganic hybrid' started to be employed in the last decades due to the appearance and development of the so-called ORMOCER, which means organically modified ceramics (ORMOSIL if the inorganic part is based on silicon) [75-77]. Organic-inorganic hybrid

materials are composed by organic and inorganic components with complementary features that, when combined, give a material with distinct characteristics of the original ones, due to the chemical nature of the materials from which they originate, although being macroscopically homogeneous [75]. Such materials are, then, homogeneous systems, derived from monomers of miscible organic and inorganic components, or could be heterogeneous systems (nanocomposites) [76].

The main feature of organic-inorganic hybrid materials is the fact that their properties are not just the sum of the individual contributions of each one of the constituents, but there is also a synergy between both parts. Also, the interface between the two domains is of extreme importance, and is what defines the classification of the hybrids in class I (organic and inorganic domains interact through weak bonds, such as hydrogen, Van der Waals or ionic bonds [78]) or class II (the two phases are linked together through strong chemical bonds, such as covalent or ionic-covalent bonds and is the class where ORMOSILs are included [75]) [75-77]. Such materials caused impact in the industrial and academic fields, since hybrid materials give the possibility of obtaining products with high levels of sophistication and miniaturization, recyclable and with low energy consumption. Hybrid materials processing starts from molecular precursors or nanobuilding blocks and, then, materials are directly processed to become particles, fibres, coatings, foams or monoliths. In this way, a wide range of applications for hybrid materials appears, taking as examples smart coatings and membranes, fuel and PV cells, therapeutic (bio)vectors, (bio)sensors, catalysts (including bio- and photocatalysis), O–I textiles, and automotive parts [76].

Despite the quite limited use of hybrid materials in the fabrication of LSC, their optical conversion efficiency, η_{opt}, which is the ratio between the output and the incident power on the LSC (Table 1.1) are of the same order of magnitude as those of pure organic LSCs [17,23,79,80]. Namely, Ln^{3+}- doped silica-based organic-inorganic hybrids were used in planar LSCs with η_{opt} values of ~9 % (from theoretical calculations) [52] and 12.3 % [55], considering the absorbing spectral region. Also, a bulk dye-doped organic-inorganic hybrid was used to produce a flexible LSC with η_{opt} of 14.5 % in the 300-800 nm range, when using a white scattering background (9.2 % with absorbing background) [25]. More recently, ureasil organic-inorganic hybrid materials doped with a perylene carboxdiimide-bridged triethoxysilane which is covalently linked to the siliceous network were suggested to be, in future, applied in LSCs [81].

Table 1.1 *Optical features of organic-inorganic hybrid materials tested in LSCs including the absorption range (λ_{abs}), the emission peak position (λ_p), the absolute emission quantum yield (η_{yield}), the Stokes shift, the optical conversion efficiency (η_{opt}) and the concentration factor (F) are presented.*

Hybrids	λ_{abs} ***(nm)***	λ_p ***(nm)***	η_{yield}	***Stokes shift (nm)***	η_{opt} ***(%)***	***F***
Perylimide-GLYMO [82]	420-620	540	0.98	97	18.8	0.08
		613	0.96	94		
Red 305-PS and Red 305/Au NPs-PS [83]	400-580	590		95		
PbS-PMMA [32]	600-950	750		83	6.5	0.27
PbS-toluene- sealed into quartz panels [43]	400-900	870	0.30	86	1.4	0.15
CdSe/ZnS-toluene- sealed into quartz panels [43]	400-650	625	0.50	96	0.5	0.06
CdSe/ZnS-toluene- sealed into glass panels [31]	376	623	0.50	60	0.3	0.05
CdSe-propylene solution [31]	300-650	623	0.50	60		
CdSe/ZnS-polyurethane [84]	560	650	0.60	86	2.1	0.8
Tb-PVA/PMMA [85]	280-400	546	0.40	53	8.8 (290 nm)[a]	1.32
Eu-M6 [54]	350	612	0.34	262	4.3 (350 nm)[a]	0.31
Eu-M4 [53]	270	612	0.08	342	1.2 (290 nm)[a]	0.09
Tb-M4 [53]		544	0.12	274	1.7 (290 nm)[a]	0.13
Eu-tU5 [52]	240-450	613	0.63±0.06	233	9.0 (360 nm)[a]	0.69
Eu-ormosil [86]	300	610		49	10-15 % increase on PV cell efficiency	
CdSe/CdS-LMA/EGDM [38]	300-500	650		150		
Coumarin/Ag/Au NPs-PMMA [30]	300-700	600		50	53 % increase on PV cell efficiency	
Mn/ZnSe/ZnS/toluene/LMA/ EGDM/TOP [39]	350-450	582		186		
$CaAlSiN_3:Eu^{2+}$/PMMA [57]	350-550	630		112	1.44	0.14
CdSe/CdS-PMMA [37]	380-500	640	0.45	160	10.2[b]	4.4
Lumogen Red F/di-ureasil [25]	300-580	615	0.88±0.06	35	9.2	0.30
$CuInS_2$/ZnS-PMMA [87]	300-400	550	0.56	200		
CdSe-PMMA [88]	400-500	550		80	2.01	2.01
$Eu(tta)_3$phen-parylene [56]	250-400	613		266	0.19	0.01
$Eu(tta)_3{\cdot}2H_2O$-F5 [55]	240-400	612	0.23±0.02	232	12.3[b]	0.68
P567-PDMS [19]	450-550	539	0.93	18		
PDI-SiL-ureasils [81]	300-600	610	0.76-0.87	20		

GLYMO=3-glycidoxypropyltrimethoxysilane; PS=polysiloxane; PMMA=poly(methyl methacrylate); PVA=poly(vinylalcohol); M4=bipyridine-based bridged silsesquioxane; tU5= tri-ureasil hybrid matrix; TOP=trioctyl phosphine; F5=Tetracarboxamide-based organic-inorganic hybrid; P567=pyrromethene 567; PDMS=polydimethylsiloxane; [a]η_{opt} *calculated by Eq. (3.3), section 3.3;* [b]η_{opt} *calculated only considering the absorbed radiation.*

Besides the influence of materials design, the emission mechanisms (energy conversion) play also a role in enhancing the LSCs performance. Although the three distinct mechanisms DS, DC and UC can be involved in the solar energy conversion, to the best of our knowledge, only LSCs based on DS hybrid materials have been reported until now.

The active layer is a key component in LSCs. It is usually a layer on glass or a sheet of a polymer within which the active species are dispersed (or encapsulated). The term *dispersed* regards here dispersion, dissolution, doping, or emulsifying. Owing to their high transparency, mechanical flexibility and durability under exposure to sunlight [89,90], polycarbonate (PC), polysiloxane (PS) and polymethylmethacrylate (PMMA) thermoplastics have been the most extensively employed polymers in the fabrication of sheets for LSCs. Thermoplastic copolymers are also considered to be good candidates for this purpose [91].

Buffa *et al* [83] demonstrated the potential of substrates based on the PS rubber for the production of flexible LSCs offering sizable benefits and extended applicability with respect to standard, rigid LSCs (Figure 1.5). The efficiency of light collection of PS rubbers doped with the Lumogen Red 305 (LR305) BASF fluorescent dye at different concentrations was comparable to that of PC substrates with the same dye concentration. Unlike in PC-based substrates, in PS-based substrates a LR305 concentration of 0.01 % weight was the upper limit beyond which self-absorption and quenching effects took place with detrimental consequences on light output (for PC this value is 0.05 wt. %). The dissimilar behaviour of LR305 in PS and PC at higher concentration was associated with the lower solubility of the dye in the apolar environment of PS.

Figure 1.5 *Photograph of LR305-doped PS-based LSCs. Taken from ref. [83].*

Bhaumik *et al.* [91] developed a LSC composed of a dual-layer sheet or panel operatively connected to a light energy converter. The sheet comprised a first layer composed of a polymer

in which a fluorescent dye (a perylene, a daylight fluorescent dye with a maximum absorption wavelength of 600 nm and a maximum emission wavelength range between 600 to 650 nm) was dispersed and a second layer comprising the second polymer in which a dye compound (quantum yield of more than 80 %, a maximum absorption wavelength between 600 and 650 nm and a maximum emission wavelength of 650 nm, or greater) was also dispersed. Both dyes absorbed light and converted it to longer wavelengths. A fluorescent brightener was also included together with the fluorescent dye, since the dye combination led to an increase of the emissions intensity. Typically, the concentration of the dyes ranged from 10^{-4} to 1.0 weight %. Both layers were made of PC, with a light transmittance greater than 55 %, or PMMA. This design enabled the transmission of light radiated from the first fluorescent dye and the dye compound to the light energy converter. Such "dye cascade" approach allowed capturing more of the light energy to which the sheet was exposed. The sheet, with dimensions 60×60×3.2 mm^3, exhibited an edge emission output of at least 450 $W \cdot m^{-2}$ when exposed to a radiation intensity of ca. 1000 $W \cdot m^{-2}$. The LSC could alternatively include a reflective backside layer.

In 2014, Daorta *et al.* reported a new concept of cascade planar LSCs, composed of a large LSC, named the primary, surrounded by four smaller LSCs, named secondaries, having PV cells attached on their small facets, in which the area covered by PV cells is independent of the area where sunlight is collected (Figure 1.6) [26]. The working principle is based on the combination of two different kinds of LSCs: the primary LSC contains optically active centres that are able to absorb in the desired spectral region of the incident radiation and the secondary LSCs contain optically active centres whose absorption spectrum is matched to the emission range of the primary LSC. With this configuration, the spectral and the geometrical light concentration are enhanced and the area covered by PV cells is strongly reduced [26].

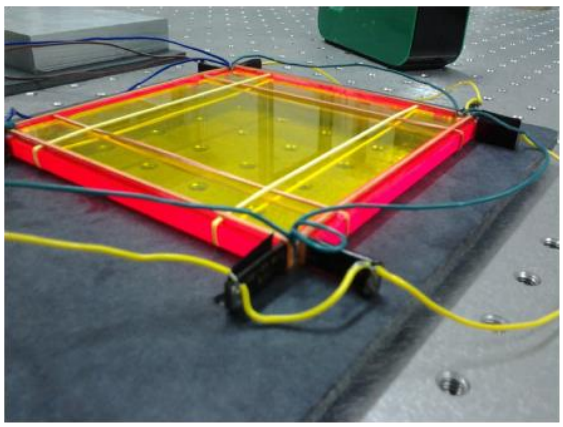

Figure 1.6 *Photograph of the prototype in PMMA of the cascade LSC assembled. Extracted from [26].*

Comparing different emitting centres, organic dyes present the highest solubility in water and organic solvents [92], the highest emission quantum yields (above 80 %) and largest absorption coefficients [66]. The most common dyes used for LSCs are rhodamines [18,93-99], coumarins [47,80,94,95,97-100] and perylene (bisimide) derivatives [23,28,47,80,82,89,99-108]. The main drawbacks related with the use of organic dyes are the small Stokes shift (<50 nm) and the photobleaching process. In particular, the latter effect determines the lifetime of the LSC and occurs when a fluorophore permanently loses the ability to fluoresce due to photon-induced chemical damage and covalent modification [109].

Another class of emitting centres includes QDs. The quantum confinement effect describing the dependence of the absorption wavelength on their particle sizes is of particular interest. It is possible to tune the absorption spectra using different semiconductor materials of different sizes [33]. Besides, there is the possibility of fabricating QDs with core-shell structure, in which the QD used in the core has a band gap energy different from that of the shell [110]. The emission quantum yields vary within 10-80 % [43,84,92] and the main drawbacks are connected with the possible toxicity and photoblinking. The photoblinking mechanism results in an "*on-off*" emission behaviour that would be disadvantageous for LSC applications since the device performance would not be constant over time [111-115].

Transition metal ions display absorption spectra spanning the ultraviolet-visible (UV-Vis) spectral range with broad and sometimes strong intraconfigurational *d-d* transitions. Emission is also observed for some of them (Cr^{3+}, Mn^{2+} and Fe^{3+} for example) and application in LSCs is therefore foreseen. Although the first papers stressing the potential application in LSCs were published in the 1980s [62,71,72], very few works were published ever since [116].

Lanthanide ions, usually coordinated to organic ligands to enhance the intrinsic *f-f* low-absorption cross-section [67], are good candidates for applications in LSCs, not only because of their large Stokes shift (>200 nm), compared to those of organic dyes or QDs, but also because of their relatively high emission quantum yields. The challenge is the choice of the best ligand that enhances the Ln^{3+} emission (through the optimization of the balance between the ligands absorption, generally in the UV range, ligand-to-Ln^{3+} energy transfer and non-radiative deactivations). The highest quantum yield values ever reported, ~80 %, were for Eu^{3+} β-diketonate complexes [52,117-119]. Ln^{3+} complexes can also be incorporated into organic-inorganic hybrid materials favouring the photostability of the active centres [52,120] and allowing the easy processing as thin films [53,54,121-133]. Moreover, despite the fact that, in general, complex incorporation is disadvantageous from the emission quantum yield point of

view, there are some examples in which the emission quantum yield is preserved after the incorporation of the Ln^{3+} complex into hybrid matrices [134,135].

The intensity of the emitting centres may be enhanced through the use of metallic nanoparticles (NPs), *e.g.* Ag and Au, due to the surface plasmon resonance effect [136-143]. In particular, it was demonstrated that the transition probabilities from the ground to the excited state of dyes are favoured by the interaction of the electronic state of the dye with metallic plasmons [74] and the increase of emission of dyes in presence of Ag NPs in sol–gel organic-inorganic hybrid films was reported [143-150]. The presence of Ag NPs on a luminescent plate increases its collection efficiency by 12 %, when compared with identical plate without them [74]. Luminescence intensification of lanthanide complexes by Ag NPs incorporated in organic-inorganic hybrids was also demonstrated [144,145]. For instance, zirconia-GLYMO films doped with Eu^{3+} complexes show an intra-$4f^6$ fluorescence enhancement of 289–440 % depending on the concentration of Ag NPs [145].

The above mentioned optically active centres convert energy through DS, DC and UC mechanisms which is one of the attractive properties displayed by Ln^{3+}-doped materials, as mentioned above. Since the seminal work performed in the 1960s on UC, the energy transfer process involving different Ln^{3+} ions has been explored, with many different applications being proposed [151-157]. Concerning PV cells, Ln^{3+}-based up-converters have been observed to lead to efficiency enhancement. Some of the examples include: GaAs with a GeO_2-PbF_2 vitroceramic doped with Er^{3+} and Yb^{3+} [158], c-Si with $NaYF_4$:Er^{3+} [159], a-Si with $NaYF_4$:Yb^{3+}(18 %)Er^{3+}(2 %) [160] and also dye-sensitized PV cells using $Y_3Al_5O_{12}$ transparent ceramics containing Yb^{3+}(3 %) and Er^{3+}(0.5 %) [161] or Er^{3+}/Yb^{3+} co-doped LaF_3-TiO_2 [162]. Most of the UC materials used for enhancing PV cells efficiency are Ln^{3+}-based NPs dispersed in polymers (e.g. PMMA [160,163] or acrylic adhesive medium [164,165]) or organic-inorganic matrices (e.g. polydimethylsiloxane, PDMS) [166,167] to make possible the deposition on the PV cells surface.

Efficient energy transfer rates and phonon energy of the host are key features in this energy conversion efficiency. Energy transfer rates are directly connected to the overall efficiency of the conversion process, while phonon energy is closely related to multiphonon relaxation of excited levels. Particular interest involves low phonon energy hosts with the consequent decrease in multiphonon relaxation for Ln^{3+} excited levels. Fluoride and chalcogenide hosts (crystals or glasses) are indeed attractive hosts concerning energy conversion.

General properties of Ln^{3+} (namely UC) in fluoride and chalcogenide glasses have been extensively explored [168,169]. Interesting examples are the fluorozirconate glasses (mainly based on ZrF_4, BaF_2, LaF_3, AlF_3 and NaF) and the fluoroindates glasses (mainly based on InF_3, ZnF_2, BaF_2 and SrF_2). For example, for the latter, energy UC has been observed in single-doped (Er^{3+} [170-172], Nd^{3+} [173,174], Pr^{3+} [175], Ho^{3+} [174], Tm^{3+} [174]) and also co-doped (Yb^3/Ho^{3+} [176], Yb^{3+}/Tb^{3+} [174,177], Yb^{3+}/Pr^{3+} [178,179], Yb^{3+}/Tm^{3+} [180-182], Pr^{3+}/Nd^{3+} [174]) samples.

Materials showing UC, potentially useful for PV cells, have been reviewed by several groups worldwide [153,157,183-185]. Comprehensive tables comprising several low phonon hosts (crystalline or amorphous) for which efficient Ln^{3+} UC is observed were reported by Wang and Liu [153] and Strümpel *et al.* [184], whereas the hosts effectively tested in PV cells were reviewed by Wang *et al.* [183] and de Wild *et al.* [185]. Of particular interest are the $NaYF_4$:Ln^{3+} NPs, mentioned in all the reviews. The possibility of obtaining these NPs with controlled sizes and morphology [154,186] leads to potential new applications, as, for instance, pH-induced thermally controlled drug release for *in vivo* bioimaging and cancer therapy [187]. Maximum quantum yields of 50 % would be expected, but only in rare examples this value is higher than 10 % [3]. The published papers reporting UC energy conversion for c-Si PV cells show a small improvement in its efficiency (<1 %) [168,188].

In any case, we must remember that UC is a non-linear effect that can be efficient as long as very high power density excitation is provided. In fact, all the works cited above mention the utilization of monochromatic excitation. Under direct sunlight the process is very inefficient. There are two approaches that could be considered to increase efficiencies. In the first one broad excitation bands are used [189,190]. An enhancement of quantum efficiencies is observed in comparison to monochromatic excitation conditions because all the Er^{3+} transitions involved are excited resonantly. The second approach being investigated concerns the use of the plasmon resonance of metal NPs at the surroundings of the UC material. In fact, large enhancement of UC of Er^{3+} with Au plasmon resonance was well demonstrated [191]. The utilization of this principle in PV cells was verified, both theoretically [192] and experimentally [193].

DC is also possible to be observed in Ln^{3+}-containing materials. Among many possible applications, the one attracting special interest nowadays includes the application of down-converters in PV cells. In the case of c-Si based cells, photons with energy above the Si band gap, otherwise converted in heat, could be split in low energy photons that will be converted in electricity [194].

Ln^{3+}/Yb^{3+} couples have been proposed, where the energy absorbed by the Ln^{3+} ion in the UV-Vis region is down-converted to two or more nearby Yb^{3+} ions. The Yb^{3+} ion with its single excited state $^2F_{5/2}$ emits at around 1000 nm, close to the Si band-gap. This process was first demonstrated in Tb^{3+}/Yb^{3+} co-doped yttrium-phosphate hosts [195] but other couples have been studied afterwards, such as, Pr^{3+}/Yb^{3+} [196-203], Tm^{3+}/Yb^{3+} [204], Ce^{3+}/Yb^{3+} [205], Er^{3+}/Yb^{3+} [206], and Nd^{3+}/Yb^{3+} [207].

Theoretically, a quantum yield value of 200 % could be achieved, but there are very few reports of well-succeeded DC experiments with PV cells, being 158 % the maximum DC quantum yield reported for a c-Si PV cell equipped with a DC glass layer doped with Pr^{3+} and Yb^{3+} (Figure 1.7) [208]. Numerical modelling of a c-Si cell and a DC glass layer doped with Pr^{3+} and Yb^{3+} led to a DC quantum yield of 186 % [209].

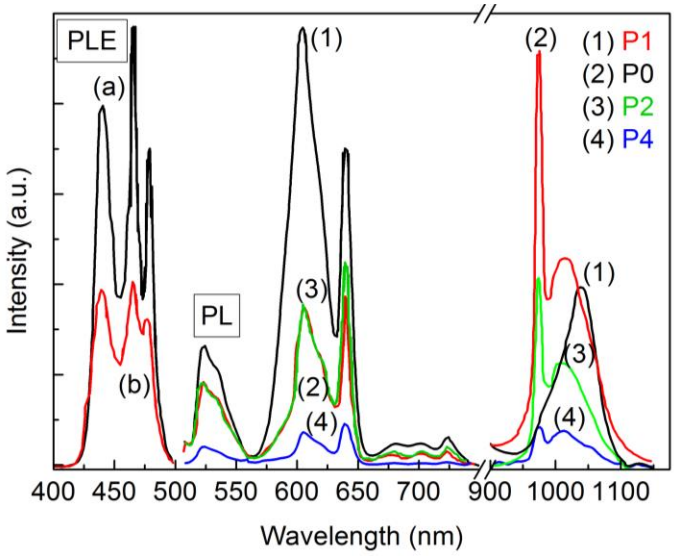

Figure 1.7 *Excitation (PLE), monitored at (a) 606 nm and (b) 974 nm, and emission (PL), excited at 482 nm, spectra of Pr^{3+}/Yb^{3+}-doped DC glass layer with different doping concentrations (P0 to P4). Taken from ref. [208].*

All the examples mentioned above involve inorganic hosts. Organic hosts, with relatively high energy vibrational modes, are almost useless. However, the organic-inorganic hybrid concept may be well applied in this field. Nanoparticulate systems may be incorporated into organic hosts while keeping the optical properties of the inorganic host. Ln^{3+} emission in the NIR spectral region, with potential application in optical amplification, is observed in organic-inorganic hybrids and several examples were reported in the last years [67,210-212].

UC in Er^{3+}/Yb^{3+}-containing hybrids is also observed under 980 nm excitation [213,214]. Zou *et al.* [215,216] introduced a breakthrough concept based on UC of NIR photons in hybrid

materials that can eventually overcome the Shockley–Queisser efficiency limit of the PV cells. An organic NIR dye was used as an antenna for β-$NaYF_4$:Yb,Er NPs in which the UC process occurs and the overall UC by the dye-sensitized NPs was dramatically enhanced (by a factor of ~3300) as a result of increased absorptivity and overall broadening of the absorption spectrum of the up-converter (Figure 1.8).

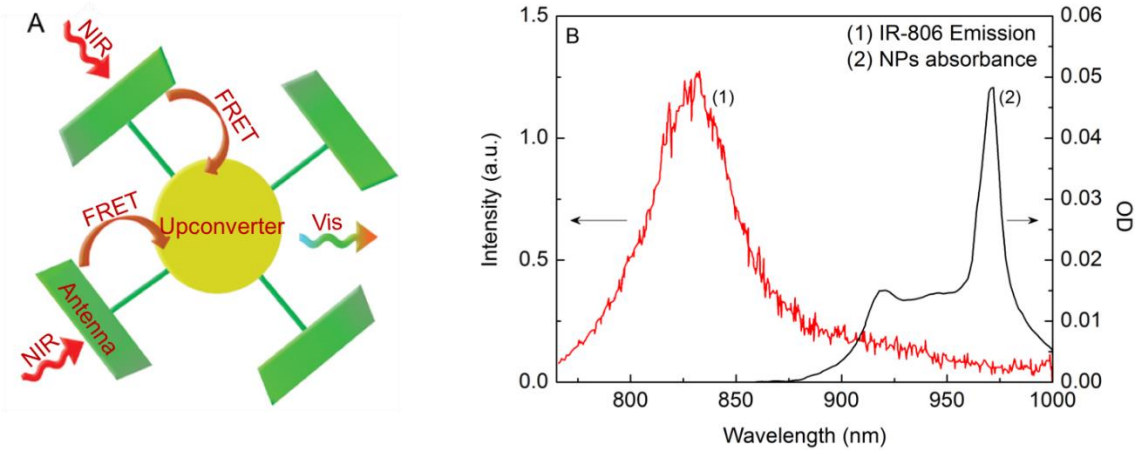

Figure 1.8 *(A) Scheme illustrating IR-806 dye molecules working as antennas for upconverting oleylamine-coated β-$NaYF_4$:Yb,Er NPs. Antenna dyes (green) absorb NIR solar energy (red wavy arrows) and transfer it (brown arrows) to the NPs (in yellow), where UC occurs (the energies of two NIR quanta are summed to emit a quantum of higher energy in the green-yellow region, green-yellow wavy arrow). (B) Emission spectrum of IR-806 in $CHCl_3$ (red line) and absorption spectrum of the oleylamine-coated β-$NaYF_4$:Yb,Er NPs in $CHCl_3$ (green line). OD, optical density. Taken from ref. [215].*

To the best of our knowledge, UC and DC processes have not been used yet for LSCs based on hybrid materials.

Focusing our attention on the η_{opt}, the larger values for planar LSCs were found for hybrid materials containing dyes, e.g. perylimide incorporated into GLYMO (18.8 %), and QDs, e.g. CdSe/CdS/ZnCdS/ZnS in a mixture of oleic acid in lauryl methacrylate and ethylene glycol dimethacrylate (15.3 % with a white reflector background, Figure 1.9) [42]. The cylindrical hollow QD LSC made of PbS incorporated into PMMA (Figure 1.10) showed a η_{opt}~6.5 % [32] and CdSe/ZnS dispersed in polyurethane and then casted into PMMA moulds presented a maximum value of η_{opt} ~2.1 % [84].

Using a theoretical expression that accounts for all the losses in LSCs (Eq. (3.3), section 3.3) for selected excitation wavelengths (Table 1.1), values of η_{opt} ~9 % for $Eu(tta)_3$.ephen (ephen=5,6-epoxy-5,6-dihydro-[1,10] phenanthroline) embedded into a tri-ureasil hybrid [52] and η_{opt} ~8.8 % for Tb^{3+}/SA-doped PVA/PMMA films [85] were found. Playing with the effect

of the substituent position on the bipyridine ring in Eu^{3+}- and Tb^{3+}-bridged silsesquioxanes (M4 and M6 hosts) [53,54] a maximum value of η_{opt} ~4.3 % was reported for the Eu^{3+}-based LSCs [54]. We should note that the values reported for Tb^{3+}/SA-doped PVA/PMMA and Eu^{3+}- and Tb^{3+}-bridged M4 silsesquioxane were obtained under excitation of 290 nm, a wavelength lying outside the AM1.5G spectral range and, then, not useful for PV conversion.

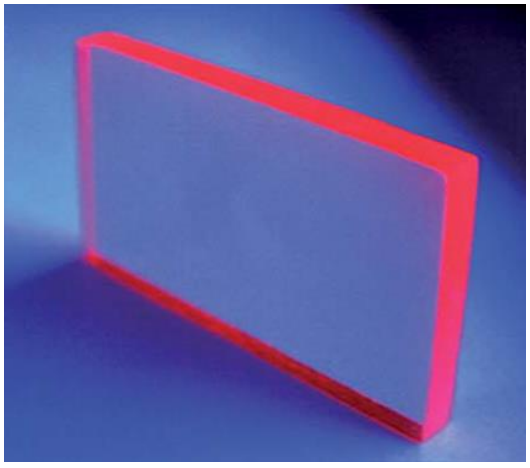

Figure 1.9 *Photograph of the QD-LSC (illuminated by a UV lamp) illustrating the concentration effect. Taken from ref.[42].*

Figure 1.10 *Hollow cylinder LSCs of PMMA doped with PbS QDs. Taken from ref. [32].*

The performance of PV cells in the presence of LSCs was also reported using others figures of merit (besides η_{opt}). For PbS and CdSe/ZnS QDs dispersed in toluene sealed into quartz LSCs and CdSe/CdS/ZnCdS/ZnS QDs in a mixture of oleic acid dispersed in lauryl methacrylate and ethylene glycol dimethacrylate, tested with Si PV cells, *PCE* values of 3.2 %,

1.2 % (full perimeter) [43] and 2.8 % (single edge) [42], respectively, were obtained. For the latter case, the short-circuit current density (J_{sc}) was 95.7 mA·cm^{-2} [42]. The LSC based on PMMA and 3-aminopropyl triethoxysilane returned a short-circuit current (I_{sc}) of 7.2 mA, when using a multi-crystalline Si PV cell. The PS rubber waveguides doped with dyes were tested with a Si photodiode and a GaAs PV cell. The J_{sc} values ranged from 66 to 102 A·m^{-2}, for the Si photodiode, and from 158 to 214 A·m^{-2}, for the GaAs PV cell. The maximum power density delivered was between 8 and 19 W·m^{-2} and 97 and 120 W·m^{-2}, for the photodiode and GaAs PV cell, respectively [83]. Some other examples involve LSCs made by PVB-doped with Eu(tta)$_3$dpbt (tta= 2-thenoyltrifluoroacetone and dpbt=2-(N,N-diethylanilin-4-yl)-4,6-bis(3,5-dimethylpyrazol-1-yl)-1,3,3-triazine) and Eu(tta)$_3$phen (phen=1,10-phenanthroline) complexes [60]. Values of *PCE* of 0.0499 and 0.0441 %, for single edge, and 0.176 and 0.200 %, for full perimeter, respectively, were obtained for tests with c-Si PV cells, corresponding to J_{sc} values of 0.150 mA·cm^{-2}, Eu(tta)$_3$phen, and 0.168 mA·cm^{-2}, Eu(tta)$_3$dpbt, were reported [60].

The ormosil-based LSC with Eu(phen)$_2$ allowed an increase in the PV current of the Si PV cell of about 10-15 %, when compared to the bare cell [86] and the LSC based on PC substrates coated by PMMA doped with mixed coumarin, Au and Ag NPs showed an increase in the a-Si PV cell of ~53 % [30]. A LSC of Lumogen Red-doped di-ureasil organic-inorganic-hybrid yielded a single edge electrical power output of 4.9 mW and therefore a *PCE* of 0.54 % over the entire spectral AM1.5G range, using a scattering background [25]. A LSC made of PMMA doped with large Stokes shift $CuInS_2/ZnS$ QDs attained a J_{sc} of 14.8 mA·cm^{-2}, comparing to 7.2 mA·cm^{-2} for the pure PMMA waveguide coupled to a commercial c-Si PV cell [87].

These values (*PCE*, J_{SC} and increase in the PV current of the Si PV cell) can be compared with those reported for organic LSCs. Some illustrative examples involve LSCs made by PMMA and Lumogen F Red 305, that showed *PCE* values of 0.51 %, which represents a *PCE* gain relative to the bare PV cell under direct illumination of 41 % [217] and, also, a LSC of PMMA doped with 4-(dicyanomethylene)-2-t-butyl-6-(1,1,7,7-tetramethyljulolidyl-9-enyl)-4H-pyran (DCJTB) dye showed J_{SC} values varying from 4.48 to 6.38 mA·cm^{-2}, leading to *PCE* values from 1.25 % to 1.96 %, according to the dopant concentration [218]. The same authors reported a LSC based on the PMMA/DCJTB thin-films with J_{SC} values varying from 23.01 to 29.47 mA·cm^{-2}, according to the thin-film thickness increased from 1.36 to 4.00 μm [20]. Also,

Currie *et al.* reported LSCs based on DCJTB and rubrene in an tris(8-hydroxyquinoline) aluminum (Alq_3) host that showed *PCE* values of 5.9 and 5.5 %, respectively [16].

Besides choosing the appropriate optically active layer and host for the specific target PV cell in use, the LSC geometry is a parameter of major importance, since it will also condition the light concentration ability of the LSC device. Thus, many researchers have studied and compared LSCs with distinct geometries. McIntosh *et al.*[219] made a theoretical comparison between square-planar and cylindrical LSCs, introducing and proposing a new geometry composed of various cylinders, one after another. They found that the optical concentration of a cylindrical LSC can be 1.9 times higher than that of the square-planar LSC of equivalent collection area and volume. If the new multi-cylindrical geometry is considered, a small increase in optical concentration could be obtained for all angles of incidence of radiation, due to multiple reflections between subsequent cylinders. Inman *et al.* [32] fabricated both solid and hollow cylindrical LSCs using NIR QDs of PbS in PMMA matrices (Figure 1.10). Their results showed that the hollow structures can lead to higher absorption and less self-absorption, comparing to the solid cylindrical LSC, thus giving better performance results. Furthermore, for QDs-doped LSCs the influence of the geometry in the efficiency was modelled showing no substantial gain between three different shapes of LSCs: hexagonal, square and a right-angle triangle [47].

Taking advantage of the cylindrical geometry of PMMA-derived plastic optical fibres (POFs) and of the large Stokes shift typical of Eu^{3+} β-diketonate complexes, a zero self-absorption loss LSC was made with a POF doped with $Eu(tta)_3phen$. The cylindrical geometry provides a geometric gain up to ~1500 (for a typical diameter of 1 mm and a length of 1 m) [49]. Moreover, Edelenbosch *et al.* reported a study claiming that coated cylindrical LSCs are more efficient when compared to homogeneously doped ones [220]. Additionally, the usage of cylindrical LSCs allows the assembling of several LSCs in such a way that a bundle structure can be obtained, with each hollow-core POF behaving as an individual LSC [27].

Apart from the use of LSCs, also DS and UC layers (so-called DSL and UCL, respectively) have been also used to enhance the PV cell performance [221]. The layer containing the luminescent species is used as PV cell coating. In this case, the light emission is transmitted directly to the PV cell, without optical guidance. Potentially, the performance of this solution can exceed the LSCs one, since the propagation losses are much smaller due to the inexistence of optical guidance (the trapping losses are identical).

Ln^{3+}- and QDs-containing hybrid DSL have been used to improve the short-wavelength response of PV cells. The coating of a Si PV cell with an Eu^{3+}-doped ormosil was tested with an increased performance of 18 %, compared to the uncoated c-Si PV cell [222]. Another example is the improvement of the external quantum efficiency (*EQE*) of a InGaAs photodetector from 1.8 to 21 % using a DSL consisting of PbS/CdS core/shell QDs embedded in PMMA [223]. Likewise, a DSL with CdSe/CdS core/shell QDs mixed with PMMA provided an enlargement of the *EQE* of CdTe PV devices from 4 to 20 % [224]. An intriguing example of a PV module multilayer coating in which the DSL is $Eu(tta)_3phen$ encapsulated into a sol-gel derived silica glass reported the increase in J_{SC} of 1.03 $mA \cdot cm^{-2}$, compared with the value measured in the absence of the DSL [225].

The use of an UCL of Yb^{3+}/Er^{3+}-doped silicone gel increased the *EQE* of a bifacial Si PV cell in 5.9×10^{-6} %, demonstrating a better performance than using a spin-on oxide to embed the UC particles, with an increase in the *EQE* of 4.0×10^{-7} % [226]. The potential of PbS QDs to enhance the performance of the UCLs mentioned above was tested dissolving PbS QDs together with the UC particles, both in the spin-on oxide and in the silicone gel. The results showed that, in both cases, the UC performance is enhanced in the presence of the PbS QDs, with an improvement in the photocurrent detected of 60 %, due to the increase of light coupling to Er^{3+} atoms [226].

Using Ln^{3+}-containing polymers as DSL for PV cells, similar figures of merit can be reached, comparing with LSCs. For instance, comparing the variation of the *EQE* of a c-Si PV cell uncoated, coated with undoped polyvinyl acetate film and coated with Eu^{3+}-doped polyvinyl acetate films, the cell coated with DSL displays an increase in the J_{SC} from 35.67 to 36.38 $mA \cdot cm^{-2}$, whereas the overall energy conversion efficiency increases from 16.05 % to 16.37 % [227]. Another example showed an increase in the total delivered power of a c-Si cell coated with a Eu^{3+}-doped PVA DSL, relatively to the case of undoped PVA coating [228].

The role of the DS mechanism in the potential enhancement of the *EQE* of a PV cell was recently predicted [229]. This model attempts to estimate the *EQE* of a PV cell coated with a DS layer, demonstrating that two main factors must be maximized; the luminescent DS efficiency (η_{LDS}, efficiency of down-shifting absorbed photons and sending them towards the underlying PV cell) that depends on the emitting layer properties (quantum yield, emission and absorption spectral range and refractive index) and on the emission spectral matching between the DS emission spectrum and the PV cell *EQE*) (Eq. 4 of ref. [229]). Figure 1.11 exemplifies

the values for these two parameters (η_{LDS} and emission spectral matching) experimentally accessed for distinct types of PV cells coated with distinct DS layers.

Focusing our attention into the case of the c-Si PV cell that is coated with the above mentioned Eu^{3+}-complexes [227] it is possible to infer that although a high emission spectral matching value is attained (~87 %) for all the cases, the η_{LDS} parameter increases from 39 to 63 % due to the different absorption and emission properties of the complexes, namely the absorption coefficient and the emission quantum yield.

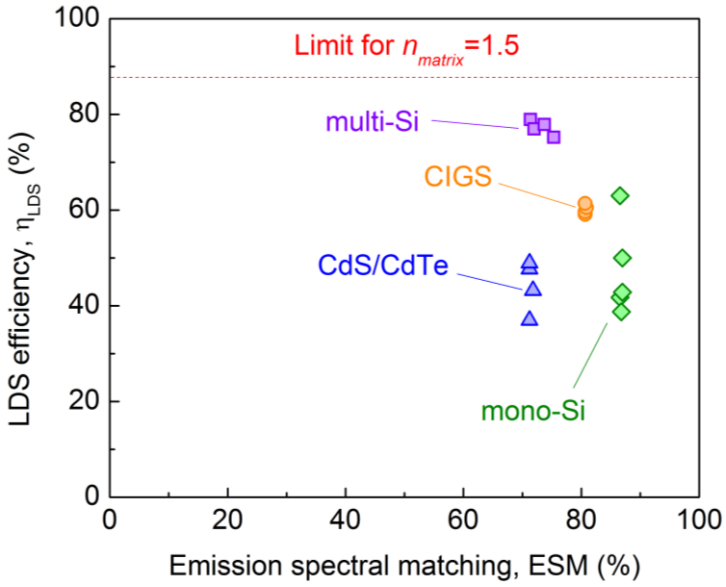

Figure 1.11 *LDS efficiency and emission spectral matching for various LDS materials and PV cell technologies. Taken from [229].*

1.2 Objectives of the thesis

In the late 1970s, the concept of LSC appeared as an effective approach towards collecting sunlight economically and without additional sun trackers with potential to overcome the limiting factors of PV conversion efficiency.

Over the past decades, several researchers have dedicated their works studying LSCs and its loss sources, with the objective of overcoming such issues. In this scope, several optically active centres were tested, as well as the substrate or matrix in which the optically active centres are deposited or embedded on, emphasizing the potential of the organic-inorganic hybrid materials for this type of application. Also, the geometry of the LSC has been seen as a factor of major importance, since it will determine the light concentration ability of the LSC. In this field, cylindrical geometry is proven to be very promising due to the easiness of large-scale

fabrication (optical fibre technology) and also because the possibility of having a larger ratio between the exposed and edge areas, known as geometrical gain. Following these theoretical results reported in the literature, the objectives of this work are the fabrication and characterization of LSCs based on organic-inorganic hybrids, using different geometries.

Although planar LSCs have been fabricated in the scope of this project, the main work is focused on the production of cylindrical LSCs, with different lengths, varying from 10^{-2} m to the metre scale, increasing the geometrical gain and, consequently, the concentration factor F that quantifies the overall performance of a LSC (which is, in most cases, lower than 1). Different configurations of LSC based on bulk-coated and hollow-core devices, in which the active layer is deposited on top of the substrate as a coating or used to fill the hollow-core, respectively, were also tested. These variations in the LSC configuration would result in distinct light propagation paths and, so, one of the objectives of the work is, also, to study light propagation in LSC with different lengths and configurations and also different materials, which have distinct optical properties, namely in terms of refractive index. Also, one of the goals of this work is to modify the outer geometry of the LSCs to allow an easier coupling between them, to compose a LSC matrix (the so-called *bundle*), that would maximize the coverage area of a square PV cell.

Seeking for the optimization of LSC devices to be used with coupled Si PV cells, which maximum response is in NIR wavelength range, NIR emitting optically active centres are of interest for this application. In this work, besides visible emitting optically active centres, also a NIR emitting organic dye was tested in a cylindrical hollow-core LSC.

The LSC performance quantification is an important issue to be addressed, since there are several ways to do that reported in the literature. In this work, the main parameters are described and estimated for the fabricated LSCs, both using theoretical expressions and expressions using electrical parameters measured in the coupled PV device.

1.3 Organization of the thesis

This thesis is divided in 7 chapters, as follows:

In Chapter 1, the state of the art and the context of the work are described, as well as the main motivations and goals.

In Chapter 2, the synthesis of the used materials, including the organic-inorganic hybrids and the dopants (Eu^{3+} complexes and organic dyes) are described and analysed.

Chapter 3 deals with the background information of LSCs, in what concerns to working principles and performance quantification, in the absence or presence of PV cells. In this chapter, the concepts of optical conversion efficiency, overlap integral, concentration factor, geometrical gain, power conversion efficiency and external quantum efficiency are addressed.

In Chapter 4, the fabrication of short-length (10^{-2} m) planar and cylindrical LSCs is described, as well as their performance quantification. Those LSCs are based on transparent glass (planar) and plastic (cylindrical) substrates coated with an organic-inorganic hybrid material doped with Eu^{3+} complexes.

Chapter 5 addresses the fabrication of LSCs, with length of 10^{-1} m based on hollow-core POFs filled with tripodal t-U(5000) organic-inorganic hybrid material doped with an Eu^{3+} complex or organic dyes (Rh6G and Rhodamine 800, Rh800). Those LSCs have a triangular geometry which allows the formation of a bundle structure with optimized coverage of the coupled PV cell.

In Chapter 6, the scale-up of the top surface area from centimetre to the metre scale of POF-based LSCs is proposed, both in coated and hollow-core configurations. The active layers used are d-U(600) and t-U(5000) organic-inorganic hybrids doped with an Eu^{3+} complex or Rh6G organic dye.

Finally, in Chapter 7 the general conclusions and future perspectives are presented. In Appendix A, the description of some devices and experimental techniques is detailed and a list of publications resulting from this work is presented in Appendix B.

Chapter 2. Eu^{3+}- and dye-based organic-inorganic hybrids

2.1 Synthesis

In this work, organic–inorganic hybrids, named ureasils, formed by polyether-based chains grafted to a siliceous backbone through urea cross linkages, were used as hosts for incorporation of the optically active centres. Di-ureasil, d-U(600), and tripodal tri-ureasil, t-U(5000), organic-inorganic hybrids were doped by the $Eu(btfa)_3(MeOH)_2$·bpeta ($btfa^-$=4,4,4-trifluoro-1-phenyl-1,3-butanedione, $bpeta^-$=1,2-bis(4-pyridil) ethane and MeOH=methanol) and $Eu(tta)_3 \cdot 2H_2O$ (tta= 2-thenoyltrifluoroacetone) complexes and Rhodamine 6G (Rh6G) and Rhodamine 800 (Rh800) organic dyes. The materials synthesis details are described below.

2.1.1. Sol-Gel process

The organic-inorganic hybrid materials were prepared by the sol-gel process and thus, this section summarises the main aspects of this method that are considered to be relevant for this work. The sol-gel method presents some features that are advantageous for the synthesis of organic-inorganic hybrids, such as the possibility of mixing organic and inorganic components at the nanometric scale, in mild synthesis conditions, including accessible and cheap precursors, the use of organic solvents, low processing temperatures and versatility of the colloidal state processing [78].

A colloid is a suspension in which the dispersed phase is so small (~1−1000 nm) that gravitational forces are negligible and interactions are dominated by short-range forces, such as van der Waals attractions and surface charges. In the sol-gel process, the precursors used for the preparation of a colloid consist of a metal or metalloid element surrounded by various ligands. The most widely used class of precursors in sol-gel research are the alkoxides, namely, the metal alkoxides, with formula $M(OR)_z$, where M is a metal, O is oxygen, R is an alkyl group and z is the number of alkoxy groups (OR) linked to the metal. The most studied example is silicon tetraethoxide (or tetraethoxysilane, or tetraethyl orthosilicate, TEOS) [77,230].

Metal alkoxides are popular precursors because they react rapidly in the presence of water. The reaction is called hydrolysis, since a hydroxyl ion becomes attached to the metal atom [77]:

$$Si(OR)_4 + H_2O \rightarrow HO{-}Si(OR)_3 + ROH.$$

where ROH is an alcohol. Depending on the amount of water and catalyst present, hydrolysis may be completed, in a way that all the OR groups are replaced by OH [77]:

$$Si(OR)_4 + 4H_2O \rightarrow Si(OH)_4 + 4ROH$$

Or it may stop while the metal is only partially hydrolysed. Two partially hydrolysed molecules can link together in a condensation reaction:

$$(OR)_3Si{-}OH + HO{-}Si(OR)_3 \rightarrow (OR)_3Si{-}O{-}Si(OR)_3 + H_2O$$

or

$$(OR)_3Si{-}OR + HO{-}Si(OR)_3 \rightarrow (OR)_3Si{-}O{-}Si(OR)_3 + ROH$$

By definition, condensation liberates a small molecule, such as water or an alcohol. This type of reaction can continue to build larger and larger silicon-containing structures by the process of polymerization [77].

The gel point is the time (or degree of reaction) at which the last bond is formed. So, a gel contains a continuous solid skeleton enclosing a continuous liquid phase. Moreover, gelation can occur after a sol is cast into a mould, producing objects in the desired shape (monolith) [77].

The sol-gel process involves multiple variables, such as time, temperature, nature of catalysts, reagents concentration, among others, that will condition the final features of the produced materials. The versatility in the processing of these materials is directly linked to the success of their development, together with the low cost and the availability of the precursors and of the processing equipment. Since the rheology of the hybrid colloidal suspension can be controlled and adjusted, there is a wide range of processing methodologies, such as: film deposition methods, fibre extrusion, fibre pulling, electrospinning, electro- chemical deposition, (soft) lithography based techniques, aerosol or spray, ink-jet printing, among others [76,78], which allows the easy coating of plastic optical fibres (POFs) or hollow-core filling to fabricate the LSCs in this work.

2.1.2 Formation of the urea cross-linked non-hydrolysed precursors, d-UPTES(600) or t-UPTES(5000)

The di-ureasil hybrid material is formed by polyether chains (with average molecular weight of 600 $g \cdot mol^{-1}$) covalently linked to a siliceous inorganic skeleton by urea bridges (Figure 2.1A) [231]. The non-hydrolysed precursor, d-UPTES(600), was prepared by the addition of isocyanate-propyl-triethoxysilane (ICPTES, Sigma-Aldrich, 95%) to a solution of Jeffamine ED–600® (Sigma-Aldrich, 97%) in dried tetrahydrofuran (THF, Sigma-Aldrich, 99.9%) (the molar ratio Jeffamine ED–600® to ICPTES was 1:2). This solution was kept under stirring at room temperature for 24 h [231]. Then, the non-hydrolysed d-UPTES(600) was obtained as a transparent liquid after evaporation of THF at room temperature under vacuum. The t-UPTES(5000) was synthesised in an identical way to that of d-UPTES(600), except for the Jeffamine® used, which presents a branched chain structure with the amino groups located at the end of each branch, with a molecular mass of 5000 $g \cdot mol^{-1}$ (Huntsman) [232].

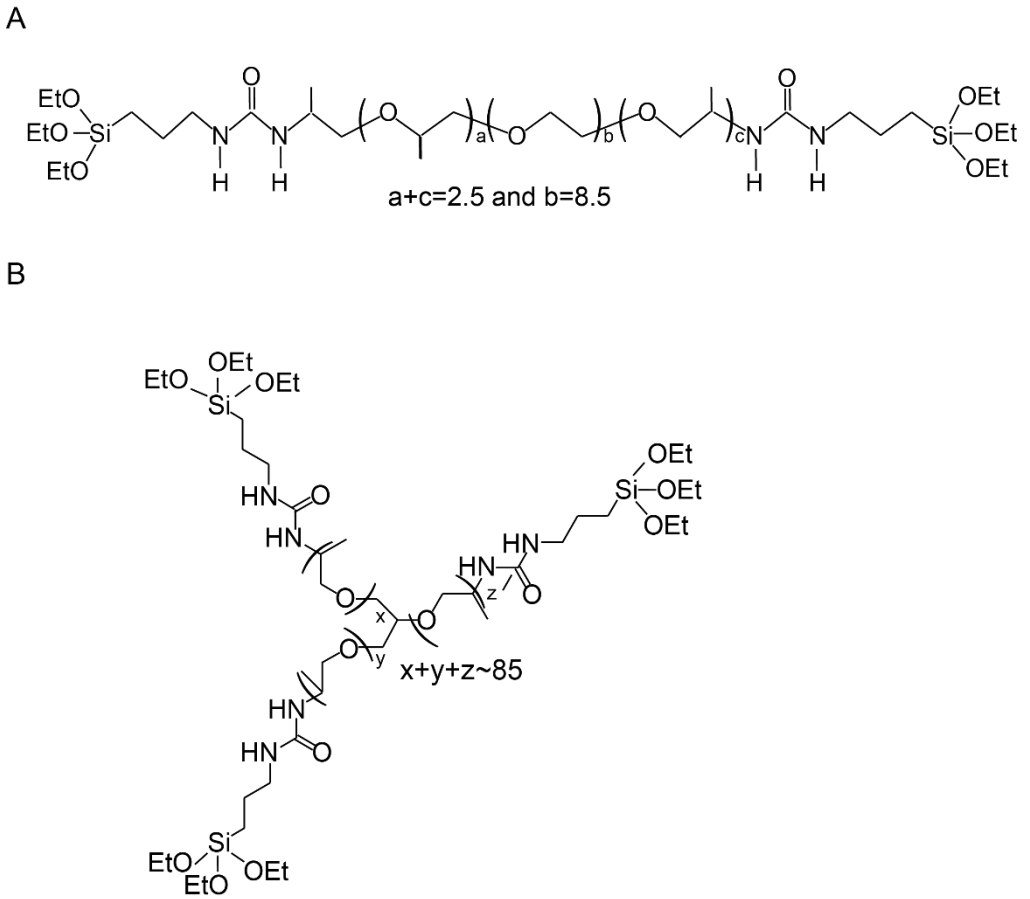

Figure 2.1 *Scheme of the chemical structure of non-hydrolysed organic-inorganic precursors (A) d-UPTES(600) and (B) t-UPTES(5000).*

2.1.3 Synthesis of the $Eu(btfa)_3(MeOH)_2$·bpeta complex

The synthesis of the $Eu(btfa)_3(MeOH)_2$·bpeta complex (Figure 2.2A) follow the steps described in the literature by Lima *et al.* [135]. The chemicals europium chloride ($EuCl_3·6H_2O$, Sigma-Aldrich, 99%), 4,4,4-tri- fluoro-l-phenyl-1,3-butanedione (Hbtfa, Sigma-Aldrich), 1,2-bis(4-pyridyl)ethane (bpeta, Sigma-Aldrich), ethanol (EtOH, Merck), methanol (Merck), and sodium hydroxide (NaOH, Merck) were used as received; 0.1 mmol of $EuCl_3·6H_2O$ and 0.3 mmol of Hbtfa were dissolved in 1 mL of MeOH. The pH of the solution was adjusted to 6.5 with a methanolic solution of NaOH. Then 0.1 mmol of bpeta was added to this solution. The resulting mixture was stirred for 24 h at room temperature. The solvent was slowly evaporated at room temperature during 48 h. The compound formed was washed with water and recrystallized in MeOH.

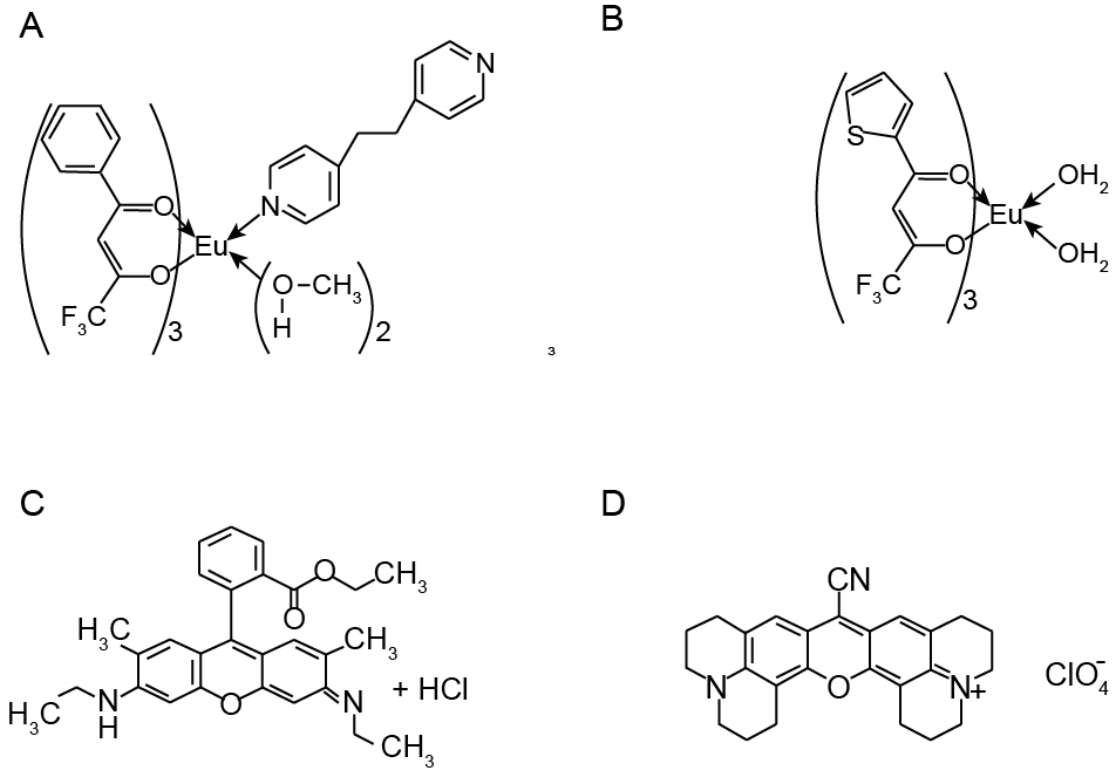

Figure 2.2 *Scheme of the chemical structures of the (A) $Eu(btfa)_3(MeOH)_2$·bpeta and (B) $Eu(tta)_3·2H_2O$ complexes, and of the (C) Rhodamine 6G and (D) Rhodamine 800 organic dyes.*

The $Eu(btfa)_3(MeOH)_2$·bpeta complex was chosen due to its high η_{yield} value of 0.58±0.06, which remains constant after its incorporation into a hybrid host (η_{yield}=0.60±0.06) [135]. Moreover, the strongly coordinating oxygen atoms of the urea C=O groups of the host hybrid displace the labile MeOH molecules from the Ln^{3+} coordination sphere and replace them. Also,

the bpeta ligand remains close to the metal centre, contributing to the sensitization process and, ultimately, to the enhancement of its photoluminescence [135].

The results of elemental analysis for C, H and N (details in Appendix A) are in agreement with the proposed complex formula. Anal. Calcd (%) for $C_{44}H_{38}EuF_9N_2O_8$: C 50.49, H 3.63, N 2.68, found; C 50.41, H 3.54, N 2.63.

Mid-infrared spectra of the $Eu(btfa)_3(MeOH)_2$·bpeta complex were recorded at room temperature (details in Appendix A). Selected FT-IR data (cm^{-1}): 3443, 3048, 1617, 1578, 1489, 1436, 1064, 631.

2.1.4 Synthesis of the $Eu(tta)_3·2H_2O$ complex

The synthesis of the $Eu(tta)_3·2H_2O$ complex (Figure 2.2B) follow the steps described by Charles *et al.* [233-235]. The chemicals europium chloride ($EuCl_3·6H_2O$, Sigma-Aldrich, 99%) and 2-thenoyltrifluoroacetone (Htta, Sigma-Aldrich) were used as received; 1 mmol (0.3662 g) of $EuCl_3·6H_2O$ was dissolved in 1.5 mL de ethanol (EtOH, Fisher Scientific, 99.9 %), under stirring. Then, 3 mmol (0.6664 g) of Htta were added dropwise to the ethanolic solution of $EuCl_3·6H_2O$. The pH of this solution was adjusted to 6-7 by adding an appropriate amount of an ethanolic sodium hydroxide (NaOH, Merck, 98%) solution. The resulting mixture was stirred for 24 h at room temperature and then the solvent was slowly evaporated during 48 h. The yellow solid obtained was washed with water and hexane (Sigma-Aldrich, ≥95 %) and recrystallized in EtOH and dried at 45 ºC during 48 h.

The rationale behind the selection of the $Eu(tta)_3·2H_2O$ complex lies on its high $^5D_0$ quantum efficiency (q=74 %) [236], that must corresponds to one of the highest η_{yield} values of hybrid materials as q is the theoretical maximum value for η_{yield}. Moreover, after incorporation on the hybrid host the water molecules coordinated to the Eu^{3+} ions will be replaced by the oxygen atoms from the carbonyl groups of the urea crosslinkages contributing to suppress the Eu^{3+} emission quenching.

The results of elemental analysis for C, H and N are in good agreement with the proposed formula of $Eu(tta)_3·2H_2O$. Anal. Calcd. (%) for $C_{24}H_{16}EuF_9O_8S_3$: C, 33.84; H, 1.90; S, 11.30; Found C 33.73, H 1.81, S 11.88.

FT-ATR spectra of the $Eu(tta)_3·2H_2O$ complex were recorded (details in Appendix A). The complexation of the tta^- ligand is furnished by the C=O stretching band. The displacement of the C=O stretching from 1650 cm^{-1} in tta^- ligand to 1608 cm^{-1} in the complex, provide good

evidence that Eu^{3+} ion is coordinated through the oxygen atoms. The presence of the band at 3364 cm^{-1} in the FT-ATR spectra of $Eu(tta)_3 \cdot 2H_2O$ indicates the coordination of the water molecules.

IR (ATR) bands: 3364, 3115, 1608, 1579, 1448, 1404, 1358, 1292, 1137, 1067, 926, 862, 800, 779, 748, 733, 584 cm^{-1}.

2.1.5 Synthesis of the di-ureasil and tripodal tri-ureasil doped with Eu^{3+} and organic dyes

The Eu^{3+} complexes described above and the organic dyes Rh6G (Figure 2.2C) and Rh800 (Figure 2.2D) were incorporated into the non-hydrolysed precursors. The organic dyes Rh6G (Sigma-Aldrich, dye content 99%) and Rh800 (Sigma-Aldrich) were used as received from the manufacturer.

The Rh6G organic dye was selected due to its absorption and emission features, associated with a high η_{yield} both in ethanolic solution (reported η_{yield} value of 0.94 in ethanol [237]) and when incorporated into a hybrid host (η_{yield}=0.70±0.07). The Rh800 organic dye was chosen mostly because of its emitting spectral range in the NIR.

The d-U(600)-based hybrids were prepared using 8.5 mg of the $Eu(tta)_3 \cdot 2H_2O$ complex or 0.7 mg of Rh6G dissolved in 0.41 mL of EtOH and added to 0.955 g of d- UPTES(600) in the presence of 55 × 10^{-3} mL of HCl 1 M (short-length fibre LSCs) or 10-37 × 10^{-3} mL of HCl 0.75 M (long-length fibre LSCs).

The $Eu(btfa)_3(MeOH)_2 \cdot$bpeta complex was incorporated in the t-UPTES(5000) by dissolving 20 mg of the complex in 1.0 mL of EtOH and added to 1.5 g of the hybrid precursor in the presence of 0.27 mL of HCl 0.05 M.

The t-U(5000)-based hybrids were prepared using 60 mg of $Eu(tta)_3 \cdot 2H_2O$ complex or 1.8 mg of Rh6G dissolved in 2.250 mL of EtOH with 0.30 mL of phenyltrimethoxysilane (PTMS) and added to 3.0 g of t-UPTES(5000) in the presence of 7.0 × 10^{-2} mL HCl 1 M (in ethanol). For the Rh800-doped hybrid, 2.8 mg of Rh800 were dissolved in 1.2 mL of EtOH and added to the t-UPTES(5000) in the presence of 8.6×10^{-2} mL of HCL 1M. It has been shown that the addition of chromophore molecules to the t-U(5000) hybrid contributed to an increase (up to 80%) of the absorption coefficient [41]. Thus, the t-U(5000) host used based on $Eu(tta)_3 \cdot 2H_2O$ and Rh6G was modified by the addition of PTMS (Sigma-Aldrich, 97%), in order to enhance the UV/vis light harvesting of the LSC device.

Chapter 3. Luminescent solar concentrators - background

3.1 Working principles

A LSC may be represented as a transparent substrate doped with optically active ions. The principle of operation of a LSC is illustrated on Figure 3.1. The sunlight is incident on the top of the transparent substrate, with a refractive index *n*. Since there are optically active centres in the substrate, they will absorb the sunlight and re-emit it at a specific wavelength. The emitted radiation is transported to the edge, until it reaches the PV cell attached, by total internal reflection (TIR), if the emission angle is greater than the critical angle, θ_c. The other sides of the LSC should be covered with a reflective coating (or PV cells) to trap photons inside the transparent substrate avoiding the escape.

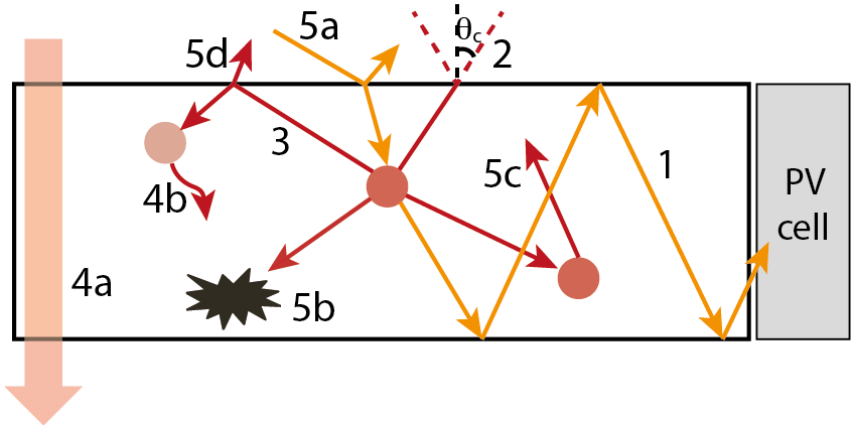

Figure 3.1 *Schematic representation of the working principle of a LSC and of the main loss mechanisms: 1) total internal reflection; 2) radiation emitted through the escape cone; 3) re-absorption of the emitted radiation by an optical active centre (solid sphere); 4a) non-absorbed radiation; 4b) non-radiative deactivations; 5a) surface reflection; 5b) internal waveguide scattering; 5c) self-absorption; 5d) surface scattering. Although not represented for simplicity, the photostability of the emitting centres could also be a loss source in LSCs. Adapted from [66].*

The principle of TIR is based on the refraction and reflection phenomena resulting from the fact that light propagates in a dielectric medium with distinct refractive indexes (Figure 3.2) [238]. There is a limit situation in which the incident beam with an angle smaller than 90 º, called

critical angle θ_c, originates a refracted beam that propagates parallel to the interface between the dielectrics. Any incident beam with an angle greater than θ_c will not be refracted, but totally reflected instead.

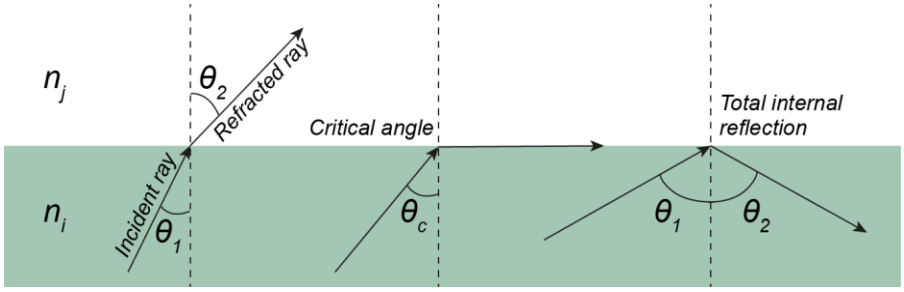

Figure 3.2 *Schematic representation of total internal reflection principle.*

Nevertheless, some amount of the emission is lost through the escape cone at the surface of the concentrator. The escape cone is determined by θ_c (through Snell's law) [65]:

$$\theta_c = sin^{-1}\left(\frac{n_j}{n_i}\right) \tag{3.1}$$

Several loss mechanisms may be present in LSCs which reduce the amount of radiation reaching the PV cells [66]. The main ones are represented in Figure 3.1. As mentioned above, the emitted light is only trapped inside the waveguide if the angle of incidence is greater than θ_c. If it is less than θ_c, the light leaves the waveguide through the escape cone and is lost (2). Also, if the absorption spectrum overlaps the emission one, re-absorption of the emitted light may occur (3). The absorption range of the optically active centre is important because, in the case of optically active centres with limited absorption range, some non-absorbed incident radiation can pass through the waveguide (4a). Moreover, if the optically active centre has a non-unity η_{yield}, emission may not occur and the absorbed photon is lost (4b). A small fraction (~4%, assuming a typical n_i~1.5) of incident radiation is reflected from the surface of the waveguide (5a) through the so-called Fresnel reflection. The emitted light may also be scattered (5b) or absorbed (5c) by the waveguide material and lost. Also, some surface scattering may occur (5d).

3.2 Light trapping

In a LSC in which the optically active layer is deposited on top of a transparent substrate as layer, light trapping may occur only in the optically active layer or in the combined system of

the optically active layer and the substrate, according to the refractive index contrast, $\Delta n_{i,j}=n_i-n_j$ with i, j=1,2,3, between the (1) air, (2) optically active layer and (3) substrate (Figure 3.3) [239].

In cases where $\Delta n_{2,3}<0$ (Figure 3.3A), light propagation of converted radiation would occur mostly in the substrate than in the optically active layer. If $\Delta n_{2,3}>0$ (Figure 3.3B), trapping will occur within the external interface with air and also in the optically active layer-substrate interface, with most of the propagation occurring in the optically active layer.

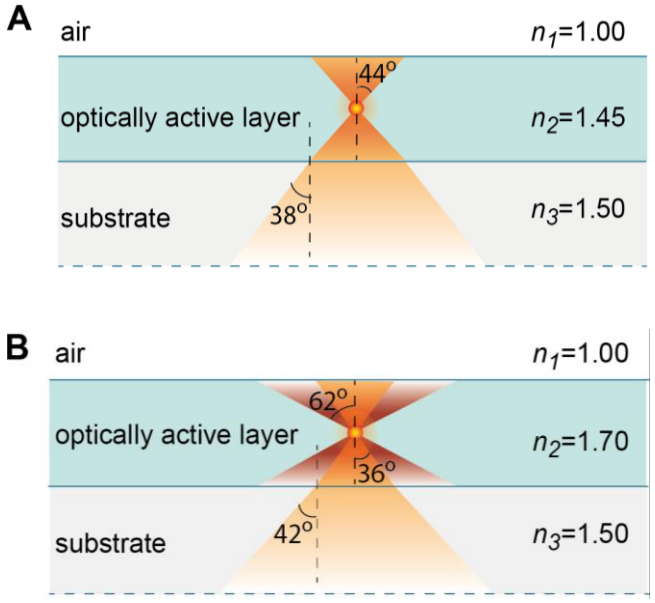

Figure 3.3 *Schematic representation of the cross-section of example LSCs with (A) $\Delta n_{2,3}<0$ and (B) $\Delta n_{2,3}>0$, with the escape cones and light trapped in the substrate and in the optically active layer (orange) and only in the hybrid (brown). The critical angles θ_c are also indicated.*

3.3 Performance quantification

The LSCs performance quantification has been reported in several distinct ways in the literature. Here, we revise the different approaches.

3.3.1 Planar and cylindrical geometries

The performance of a LSC is quantified by the optical conversion efficiency (η_{opt}) which is a measure of ratio between the output power at the LSC edges (P_{out}) and the incident optical power (P_{in}) [17,33,80,240,241]:

$$\eta_{opt}=\frac{P_{out}}{P_{in}} \tag{3.2}$$

The η_{opt} can be described by weighting all the losses (Figure 3.1) in the LSC, given by the product of several terms [241]:

$$\eta_{opt}=(1\text{-}R)\eta_{abs}\eta_{SA}\eta_{yield}\eta_{Stokes}\eta_{trap}\eta_{tr} \quad (3.3)$$

in which:

- $R=(n_f-n_i)^2/(n_f+n_i)^2$ is the Fresnel reflection coefficient for perpendicular incidence, in which n_i represents the refractive index of the optically active layer at the incident wavelength (λ_i).
- $\eta_{abs}=1-10^{-A}$ is the ratio of photons absorbed by the emitting layer to the number of photons falling on it, with A representing the absorbance value at λ_i. For LSCs with a non-planar geometry, η_{abs} is not constant along the device surface and, then, the thickness must be estimated accordingly. For instance, for cylindrical geometry, and perpendicular incidence of sun radiation, the optical absorption path increases from the middle to the surface along the radial direction.
- η_{SA} is the self-absorption efficiency, arising from self-absorption of the emitting centres. When the spectral overlap between the excitation and emission spectra of the emitting centres is null, $\eta_{SA}=1$, as in the case of Ln^{3+}. If this overlap is not null, $\eta_{SA}<1$, as typically observed for dyes and QDs.
- η_{yield} is the emission quantum yield of the optically active centre at λ_i.
- $\eta_{Stokes}=\lambda_i/\lambda_p$ is the Stokes efficiency calculated by the energetic ratio between the average energy of the emitted photons (the emission peak position, λ_p, in energy units) and the incident energy (corresponding to λ_i).
- $\eta_{trap}=(1-1/n_p^2)^{1/2}$ is the trapping efficiency, where n_p is the refractive index of the emitting medium at λ_p, is defined as the fraction of photons confined within the substrate, i.e., the fraction of photons emitted from the edge versus the photons emitted from the face and edge combined. This term accounts for the emission losses at the surface through a so-called escape cone (Figure 3.1).
- η_{tr} takes into account the transport losses due to matrix absorption and scattering, frequently it is considered that $\eta_{tr}=1$, as the transport and scattering losses are neglected. Nevertheless, Graffion *et al.* reported that scattering plays an important role, which

readily contributes to decrease η_{tr} [54]. In particular, the emission ratio C, defined as the ratio between the intensity at the surface and at the edges, was modelled by:

$$C=\frac{\eta_{opt}}{\frac{\eta_{sf}}{2}}\frac{A_t}{A_e}=\frac{2\eta_{trap}}{(1-\eta_{trap})}\frac{A_s}{A_e} \tag{3.4}$$

where

$$\eta_{sf}=(1-R)\eta_{abs}\eta_{yield}\eta_{Stokes}\eta_{trap}(1-\eta_{tr})\eta_{SA} \tag{3.5}$$

is the conversion efficiency of the signal emitted at the surface of the film (in which the trapping efficiency is replaced by its complementary value, $(1-\eta_{trap})$, A_s and A_e are the top surface area and the edge surface area of the LSC (assuming all of the other faces with reflective coatings and a white diffuser on the rear side [33]), respectively, and the factor 1/2 takes into account the emission regards only one film surface. The C factor predicted by Eq. (3.4) should be compared with that measured experimentally [54]. It was demonstrated in the literature that, for LSCs based on bridged silsesquioxane hybrids doped with Eu^{3+}, the value estimated by Eq. (3.4) was substantially higher (C=57) than the experimental value (C=6). Such discrepancy was explained by considering that the signal trapped in the waveguide will lose part of its intensity due to scattering effects along the propagation in the film, in a similar way that was performed in the estimation of the losses incurred by self-absorption in LSCs of liquid solutions of PbS QDs [43]. Therefore, Eq. (3.4) was rewritten as follows:

$$C_{eff}=\frac{2\eta_{tr}\eta_{trap}}{(1-\eta_{trap})+(1-\eta_{tr})}\frac{A_s}{A_e} \tag{3.6}$$

Although not usually mentioned in the literature, notice that η_{opt} is dependent on the excitation wavelength. Therefore, the calculus of the overall η_{opt} through Eq. (3.3) requires integration over the excitation spectrum limits (λ_1 and λ_2):

$$\eta_{opt}=\eta_{trap}(\lambda_p)\frac{1}{(\lambda_2-\lambda_1)}\times\int_{\lambda_1}^{\lambda_2}(1-R(\lambda_i))\eta_{abs}(\lambda_i)\eta_{yield}(\lambda_i)\eta_{Stokes}(\lambda_i,\lambda_p)d\lambda_i \tag{3.7}$$

assuming $\eta_{SA}=\eta_{tr}=1$ [54,241]. Obviously, integration limits that lie outside the AM1.5G spectral range are not useful for PV conversion. In this sense, an effective η_{opt} can be calculated replacing

the limits in Eq. (3.7) by those of the overlap integral between the excitation and the AM1.5G spectra, given by [52]:

$$O = \int_{\lambda_1}^{\lambda_2} I_{AM1.5G}(\lambda) \times I_x(\lambda) d\lambda \qquad (3.8)$$

where λ_1 and λ_2 are the limits of the spectral overlap between the excitation spectrum of the optical active layer and the AM1.5G spectrum. The use of the excitation spectra in normalized units for the calculation of the overlap integral O has some limitations, since it could induce some differences in the overlap absolute area. This means that using the absorption spectra in A units could be a better approximation. The drawback of using the absorption spectra comes from the fact that not all absorbed photons are capable of inducing emission of the active layer, overestimating the overlap absolute area. Thus, the use of the excitation spectra in normalized units for the calculation of O is a good approximation whenever A~1.

The variation of the percentages of the AM1.5G solar irradiance (Figure 3.4) points out that for excitation wavelengths between 280 and 320 nm only 0.15 % is available for DS conversion and that between 280 and 400 nm that percentage increases to 4.6 % [3]. The η_{opt} values calculated through Eq. (3.7) can be directly compared with those estimated by Eq. (3.2) and represent a valuable tool to describe the performance of a LSC in the absence of a solar simulator. The reported η_{opt} values for LSCs based on organic-inorganic hybrid materials are listed on Table 1.1.

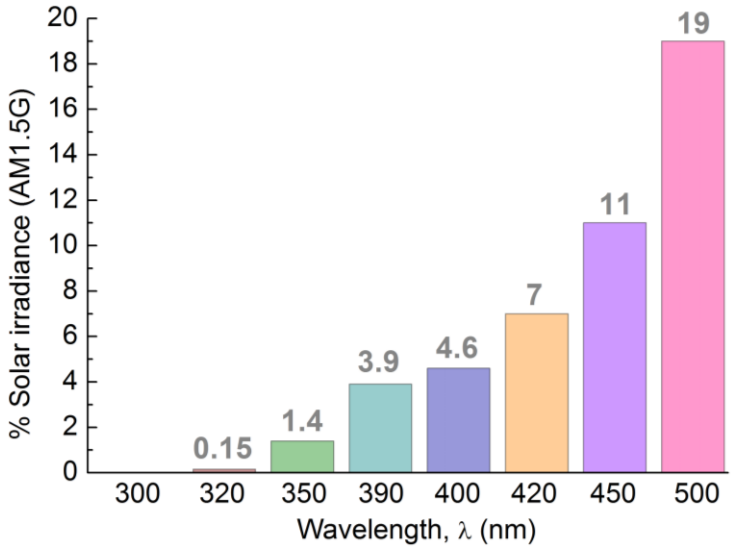

Figure 3.4 *Calculated percentages of the AM1.5G solar spectrum emitted between 280 nm and wavelength λ. Adapted from [3].*

The predictable maximum limit for η_{opt} was theoretically studied [18,31,68,82,242] not taking into account the excitation wavelength dependence. For instance, efficiency calculations with conventional PV cell theory applied to LSCs in a stack of transparent sheets involving dyes and semiconductors (Ge, Si, GaAs) yield a theoretical maximum conversion efficiency of 30 %, although more realistic values around 20 % have been mentioned under optimum conditions [68]. Monte-Carlo studies (taking into account the absorption and emission probabilities) on LSCs based on perylimide dyes embedded in GLYMO [82], liquid solutions of Rhodamine B and Red305 encapsulated in glass tubes [31], and commercial CdSe-CdTe QDs [242] were also performed. Moreover, a mathematical assessment of LSCs accounting for all the intrinsic (size, shape, design and materials) and extrinsic (geographical, seasonal and spectral distribution of solar radiation) factors that influence the performance of such devices was also reported [71]. In all these works, the main limiting factor is the high spectral overlap between emission and absorption spectra that yield maximum values of η_{opt} within 20-30 %.

The maximum limit for η_{opt} can be also inferred through a simpler analysis of Eq. (3.3), considering that all the involved parameters can be near the unit, except η_{trap} and η_{Stokes}. For typical values of the refractive index around 1.5, η_{trap} ~75 % and for a wavelength shift from the UV/blue to the red spectral region around 690 nm (around the wavelengths at which the a-Si PV cells are more efficient) [3] η_{Stokes} ~50 %, the maximum predictable value for η_{opt} is ~40 %.

Besides η_{opt}, another parameter that is also often used to quantify the performance of a LSC is the concentration factor [33]:

$$F = G \times \eta_{opt} \tag{3.9}$$

in which G is the geometrical gain factor $G = A_s / A_e$.

3.3.2 Prototype coupled to photovoltaic cells

When the LSCs are coupled to a PV cell, the η_{opt} can be calculated by [82]:

$$\eta_{opt} = \frac{P_{out}}{P_{in}} = \frac{I_{SC}^{L} V_0^{L}}{I_{SC} V_0} \frac{1}{G} \frac{\eta_{solar}}{\eta_{PV}} \frac{\int I_{AM1.5G}(\lambda) d\lambda}{\int_{\lambda_1}^{\lambda_2} I_{AM1.5G}(\lambda) d\lambda} \tag{3.10}$$

where η_{PV} is the PV cell efficiency at λ_p and η_{solar} is the average efficiency value of the cell with respect to the total solar spectrum [82]. The parameters I_{SC}^{L} and V_0^{L} stand for the short-circuit

current and the open-circuit voltage, respectively, when the PV cell is coupled to the LSC under AM1.5G illumination. I_{sc} and V_0 represent the short-circuit current and the open-circuit voltage, respectively, when the PV cell is directly exposed to AM1.5G illumination (in the absence of the LSC). The ratio:

$$\frac{\eta_{solar}}{\eta_{PV}} = \frac{\int EQE_{PV}(\lambda) I_{AM1.5G}(\lambda) d\lambda}{\int EQE_{PV}(\lambda) I_{em}(\lambda) d\lambda} \tag{3.11}$$

where EQE_{PV} is the external quantum efficiency of the PV device coupled to the LSC and I_{em} is the LSC active layer emission spectrum intensity.

In the literature, Eq. (3.10) is often presented in simplified formulations given by Eq. (3.12), Eq. (3.13) [17,31-33,43,80,240] and Eq. (3.14) [20,32,43,56,107], that are not considered to be comparable to the ones previously described, since they will only take into account the current delivered by the PV cell, instead of the total electrical power, despising the voltage and, thus, overestimating the η_{opt} values:

$$\eta_{opt} = \frac{I_{SC}^{L}}{I_{SC}} \frac{R_{PV}}{R_{solar}} \frac{1}{G} \tag{3.12}$$

in which R_{PV} is the responsivity of the PV cell to λ_p and R_{solar} are the average responsivity value of the cell with respect to the total solar spectrum,

$$\eta_{opt} = \frac{I_{SC}^{L}}{R_{PV}} \frac{1}{\int I_{AM1.5G}(\lambda) d\lambda} \frac{1}{G} \tag{3.13}$$

and

$$\eta_{opt} = \frac{I_{SC}^{L}}{I_{SC}} \frac{1}{G} \tag{3.14}$$

Also, the following expression can be found in the literature, which does not account for the mismatch between the emission of the active layer and the spectral response of the PV cell in use, and thus is not comparable to Eq. (3.10) [84]:

$$\eta_{opt} = \frac{P_{out}}{A_s \cdot \int I_{AM1.5G}(\lambda) d\lambda} \tag{3.15}$$

When the LSC coupled to a PV cell is put under simulated solar illumination, the overall *PCE* is defined as the ratio between the output electrical power and the input optical power, given by:

$$PCE=\frac{I_{SC}^{L}V_{0}^{L}}{A_s\cdot\int I_{AM1.5G}(\lambda)d\lambda}\times FF \tag{3.16}$$

where *FF* is the fill factor of the PV cell.

The performance of a LSC when coupled to a PV cell may also be quantified in terms of *EQE* [20,24,38,42,65,107,243-245]. The *EQE* can be defined as the ratio of the number of generated charge carriers that actually contribute to the generated current to the number of incident photons. The *EQE* of a PV cell can then be expressed in terms of the incident optical power and the current generated as [246]:

$$EQE=\frac{I_{SC}\cdot E_v}{P_{in}\cdot e} \tag{3.17}$$

where, I_{sc} is the generated short-circuit current, E_v is the energy of the incident photons, P_{in} is the power of the incident beam and e is the charge of the electron.

Chapter 4. Eu^{3+}-based luminescent solar concentrators: planar and short-length POF

4.1. Introduction

The LSC geometry is a very important factor on the device design. Despite the fact that most of the devices are planar, theoretical works suggest that cylindrical geometry allows an increase of the concentration factor, yielding more efficient LSCs [32,219,220,247]. For instance, the *F* value of a cylindrical LSC can be twice higher than that of a square-planar LSC of equivalent collection area and volume, because the ratio between the absorption and collection areas is greater [219]. As vitreous and polymer fibres are already produced on large scales, optimized and low manufacturing costs can be achieved for cylindrical LSCs [32,219,220,247]. Moreover, when diffuse radiation is considered instead of direct light, the higher *G* value of cylindrical LSCs, comparing to that of planar ones, has great advantages in cloudy weather conditions, shaded locations and whenever direct irradiance is scarce or absent [247]. Despite these advantages, very few examples of LSCs with cylindrical geometry can be found in literature: i) POFs based on PMMA doped with Rh6G or $Eu(tta)_3phen$ [49]; ii) solid and hollow cylindrical LSCs fabricated by doping PMMA with PbS QDs [32]; iii) a fluorescent fibre solar concentrator made of 150 QDs-doped acrylic fibres symmetrically embedded into a PMMA plate [248]; and iv) a low-weight and mechanically flexible fibre LSC bundle assembled from multiple dye-doped POFs [27,249].

In this chapter, it is reported the fabrication of short-length LSCs, with exposed area of the order of 10^{-2} m, both with planar and cylindrical geometries. These LSCs are based on a transparent substrate coated with a Eu^{3+}-doped organic-inorganic hybrid layer.

4.2 Planar geometry

The first LSC prototype fabricated in the scope of this work was a planar LSC, based on a square glass substrate coated with t-U(5000) doped with $Eu(btfa)_3(MeOH)_2$·bpeta [135]. The doped organic-inorganic hybrid synthesis routine is described in section 2.1.

4.2.1 LSC fabrication

The Eu^{3+}-doped t-U(5000) hybrid was processed as thin film deposited on a glass substrate (2.5×2.5×1.0 cm^3) by spin-coating. To enable the substrate to be spun, they were held by suction on a chuck, placed on the axis of the spin coater (SPIN150-NPP, APT) accelerated at 1500 rpm for 60 s. The films were then dried at 50 °C for 12 h, for complete solvent removal.

4.2.2 LSC characterization

The experimental techniques for the optical characterization, including photoluminescence, UV-Vis absorption and emission quantum yield are described in Appendix A.

The electrical power at the LSC output was estimated using a commercial Si PV cell (AM-1456, Sanyo), whose surface dimensions, 2.5×1.0 cm^2, match the edge of the glass substrate, by measuring the short-circuit current and the open-circuit voltage. These I–V measurements were performed under UV irradiation at 365 nm using a 6 W UV lamp (Spectroline E-Series UV lamp, Z169625, Sigma-Aldrich).

4.2.3 Results and discussion

Figure 4.1 shows the planar LSC under room illumination and UV irradiation. The emission, visible to the naked eyes, is ascribed to the Eu^{3+} transitions (Figure 4.2A) and is guided, through total internal reflection, to the edges of the device. In one of the edges, the PV cell is attached and all other edges of the LSC are covered with reflective silver ink, so that all emitted radiation can be collected in the PV cell.

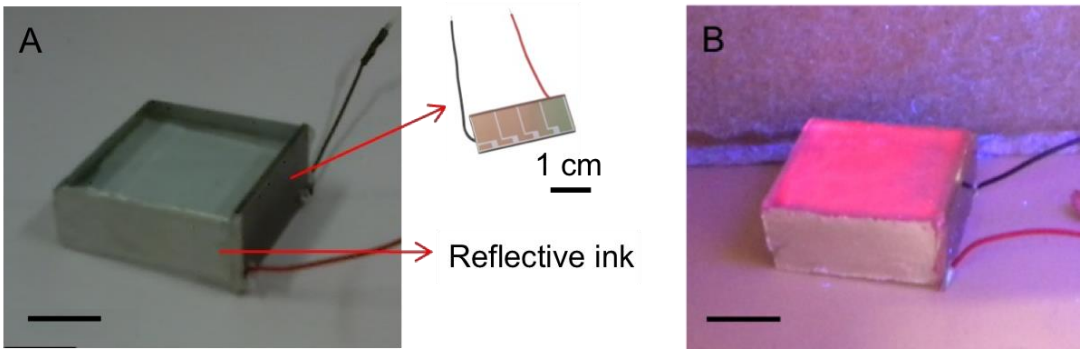

Figure 4.1 *Photograph of the fabricated planar LSC attached to a Si PV cell under (A) room illumination and (B) UV exposure at 365 nm. The scale bar corresponds to 1 cm.*

The emission spectrum of the Eu^{3+}-doped t-U(5000) organic-inorganic hybrid displays the intra-$4f^6$ lines between the $^5D_{0,1}$ excited states and the $^7F_{0-4}$ levels of the ground state. The excitation spectrum of the active layer was monitored within the emission peak position ($^5D_0 \rightarrow {}^7F_2$ transition, Figure 4.2B). The excitation spectrum of the active layer is formed of a broad band, which present a full-width-at-half-maximum (fwhm) of ~130 nm in the UV spectral region with two main components at ~280 nm and at ~370 nm mainly ascribed to the hybrid host and to the tta triplet states [52,236]. The high-relative intensity of the tta-related band readily indicates that the ligand-excited states are the main intra-$4f^6$ population path.

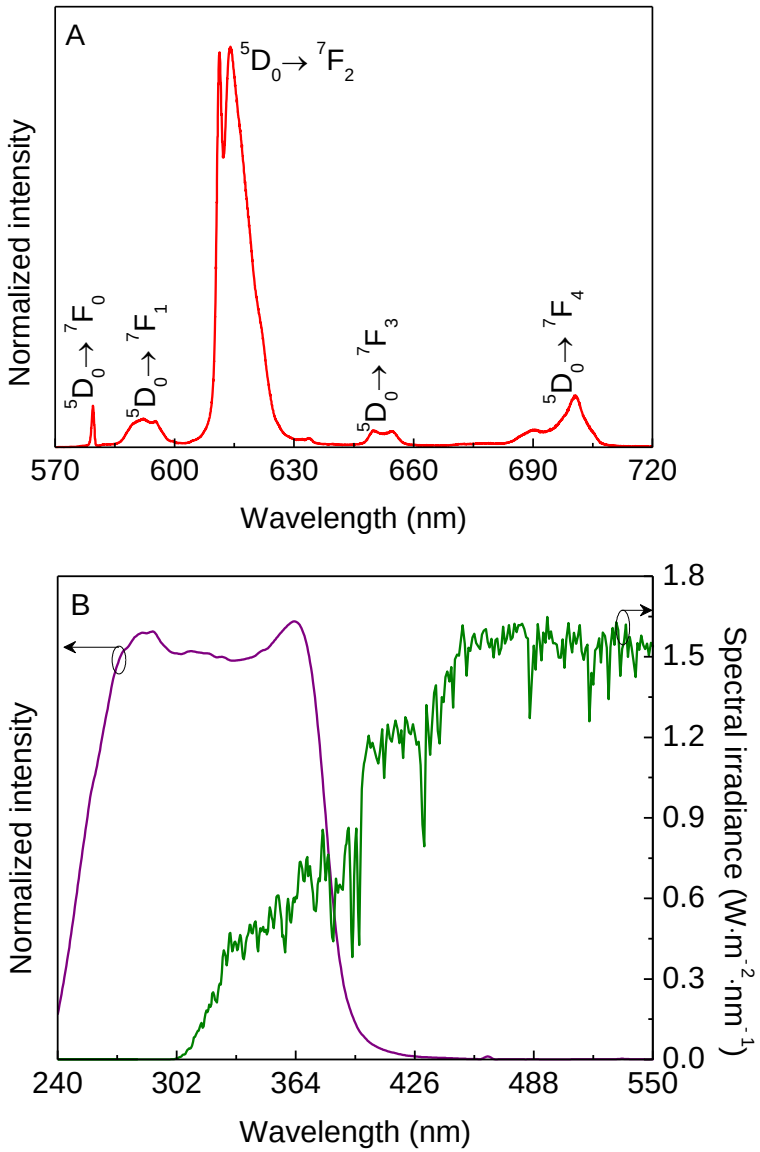

Figure 4.2 *(A) Emission spectrum of the hybrid layer excited at 360 nm and (B) excitation spectrum monitored at 611 nm, AM1.5G solar spectrum (green line) and overlap integral O (shadowed area).*

The LSC performance was quantified by estimating the overlap integral O, η_{opt}, F and PCE. The overlap integral was estimated to be ~33 $W \cdot m^{-2}$, which means that the optically active layer has the potential to absorb 22 % of the extra sunlight intensity available for DS conversion that Si would not use (149 $W \cdot m^{-2}$) [2,3,13,73].

As previously mentioned in section 3.3, the η_{opt} measured values can be rationalized through Eq. (3.3), section 3.3. Here, we consider that such as η_{SA}, η_{tr} is equal to the unity, because the t-U(5000) tri-ureasil is transparent in the visible spectral region [250]. We also consider $n_i=n_p=1.5$ and the absorption spectrum in Figure 4.3. Thus, the remaining parameters R, η_{abs}, η_{yield}, η_{Stokes} and η_{trap}, were considered to be, respectively, ~0.04, ~0.34, ~0.27, ~0.48 and ~0.75. From Eq. (3.3), section 3.3, we get η_{opt}~3.2 %. Considering G=2.5, the concentration factor F~0.09. When considering the electrical parameters of the coupled PV cell, a value of PCE of 0.007 % (through Eq. (3.16), section 3.3) for single edge was also attained, considering PV cell FF=0.75.

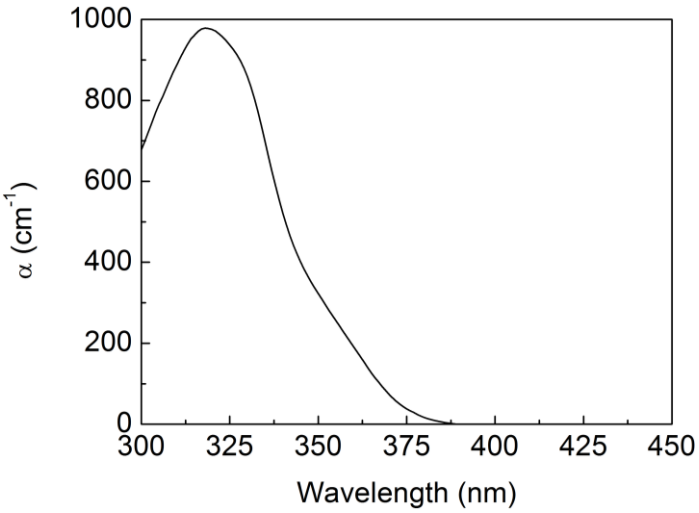

Figure 4.3 *Absorption coefficient (α) of the Eu^{3+}-doped t-U(5000) layer. As the glass substrate displays a very high absorbance for wavelengths lower than 300 nm α is not recorded in that spectral region.*

The estimated η_{opt} value for this planar LSC is of the same order of similar reported ones, also based on square glass substrates, coated with Eu^{3+}-doped organic-inorganic hybrids, whose performance was estimated by the same expression [52-55], namely, Ln^{3+}- doped silica-based organic-inorganic hybrids were used in planar LSCs with η_{opt} values of ~9 % [52] and ~4 % [54], considering the absorbing spectral region. We should call the attention for the fact that this

device is essentially transparent in the visible spectral region, which is an important requirement when thinking about urban integration of LSCs as windows, for instance.

4.3 Cylindrical geometry

The coating of commercial POFs with an emitting layer will allow the easier production of long cylindrical LSCs, with the consequent cost reduction and scalable fabrication, when compared with that attained when a cylindrical LSC is fabricated by Eu^{3+}-doping PMMA [32,49]. Moreover, theoretical studies also reported that dye-coated PMMA transparent cylinders are more efficient as LSCs, when compared to homogeneously doped ones due to a higher trapping efficiency [220,251]. Also, the parasitic losses due to self-absorption and scattering from impurities can be greatly reduced when compared to the case of a LSC based on bulk cylinders in which the optical centres are embedded [102,220].

So, here we report a cylindrical LSC based on a POF coated with a d-U(600) organic-inorganic hybrid doped with $Eu(tta)_3 \cdot 2H_2O$ complex.

4.3.1 Fibre-based LSC fabrication

The PMMA-based POFs (Jiangsu TX Plastic Optical Fibres Co., Ltd) with refractive index of ~1.49 in the visible spectral region and a diameter of 3.0×10^{-3} m were cut into segments of 5.0×10^{-2} m. The selection of such diameter was because commercial photodiodes with cylindrical geometry have active region diameters of this order. Then, approximately half-length of the fibre segments were vertically immersed in the Eu^{3+}-doped d-U(600) solution at a velocity of 1.4×10^{-3} m·s^{-1} using a homemade dip-coating system. Three POFs were coated under the same experimental conditions to ensure the reproducibility of the deposition process. After the deposition, the fibre waveguiding LSCs were transferred to the oven at 45 °C for 48 h.

One key parameter in the LSC design is the thickness (t) of the deposited Eu^{3+}-doped d-U(600) di-ureasil layer, as it determines η_{abs}.

For a cylindrical substrate (like the POFs) of radius r_1 coated with an optical active layer with thickness $t=r_2-r_1$, η_{abs} will depend on the radial position (along the x axis, Figure 4.4A). Due to the cylindrical geometry, the optical path inside the absorbing optical active layer for a collimated perpendicular AM1.5G incidence depends on the radial position. In particular, two distinct regions are identified: i) Region 1 ($|x| \leq r_1$), the absorption optical path is comprised

between the POF surface (non-absorbing region) and the LSC external radius and ii) Region 2 ($|x|>r_1$), the absorption optical path is defined by the thickness of the optical active layer (Figure 4.4A). Therefore, η_{abs} dependence on the radial position, $\eta_{abs}(x)$, is described by:

$$\begin{cases} \eta_{abs}(x,\lambda) = 1 - 10^{\left(-2\alpha(\lambda)\sqrt{r_2^2 - x^2}\right)}, & |x| > r_1 \\ \eta_{abs}(x,\lambda) = 1 - 10^{\left(-\alpha(\lambda)\sqrt{r_2^2 - x^2} - \sqrt{r_1^2 - x^2}\right)}, & |x| \le r_1 \end{cases} \quad (4.1)$$

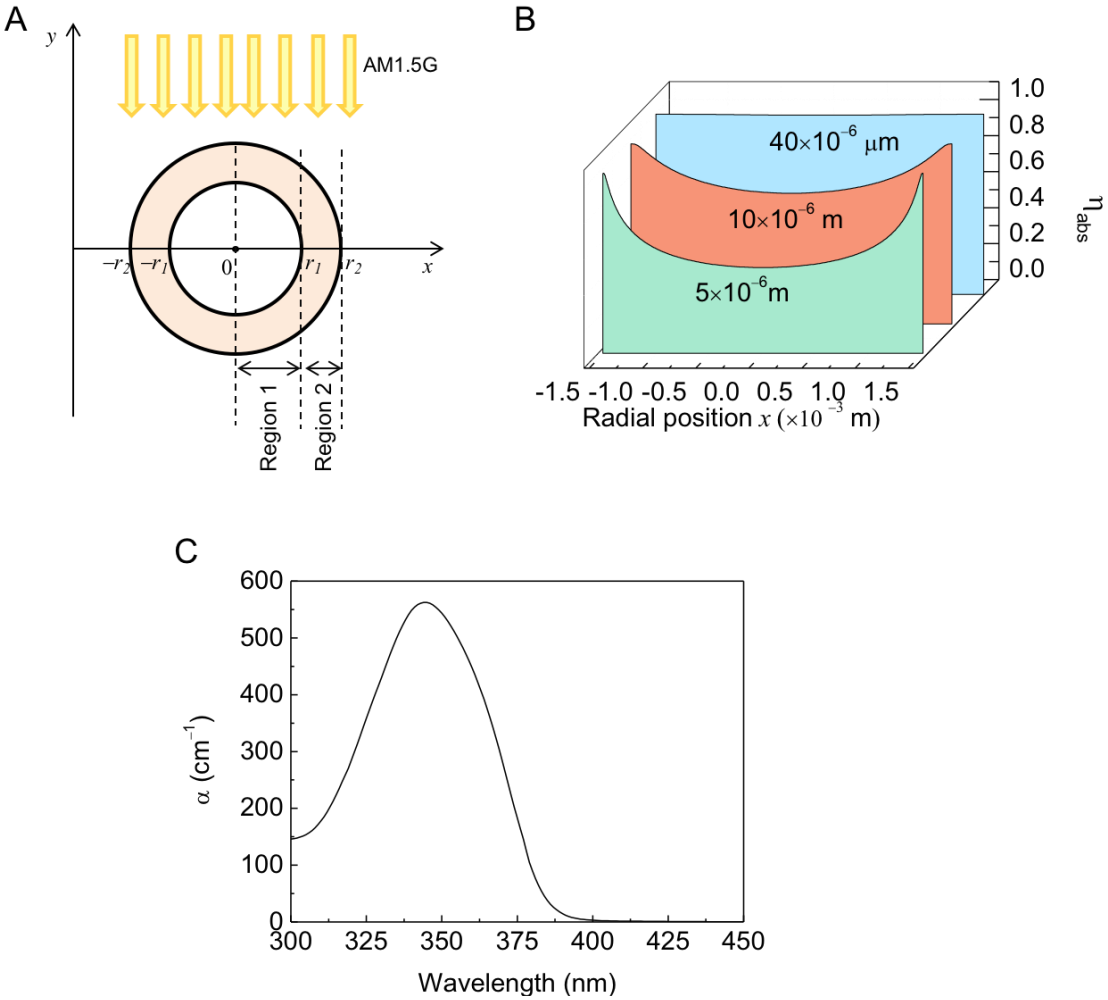

Figure 4.4 *(A) Schematic representation of the LSC cross section where r_1 is the radius of the POFs coated with an optical active layer with thickness $t=r_2-r_1$ and (B) η_{abs} variation for the optical active layers with distinct thickness values (5-40×10^{-6} m). The absorption coefficient (α) spectrum of the optically active layer is shown in (C).*

The absorption coefficient α (cm^{-1}) was estimated in a thin Eu^{3+}-d-U(600) layer using $\alpha=\frac{A}{t}$, where A stands for the absorbance and t (the layer thickness) was measured by ellipsometry, using the same conditions as for the planar LSC described in section 4.2. The maximum absorption coefficient is $\alpha=562\ cm^{-1}$ at 345 nm (Figure 4.4C) and the average value of η_{abs} can be obtained by integration of Eq. (4.1) along the LSC radial position.

The thickness of the Eu^{3+}-doped d-U(600) layer was optimized to maximize η_{abs} (Figure 4.5). Figure 4.4B shows the absorption profile for cylindrical LSCs with distinct thickness values for the Eu^{3+}-doped d-U(600) layer.

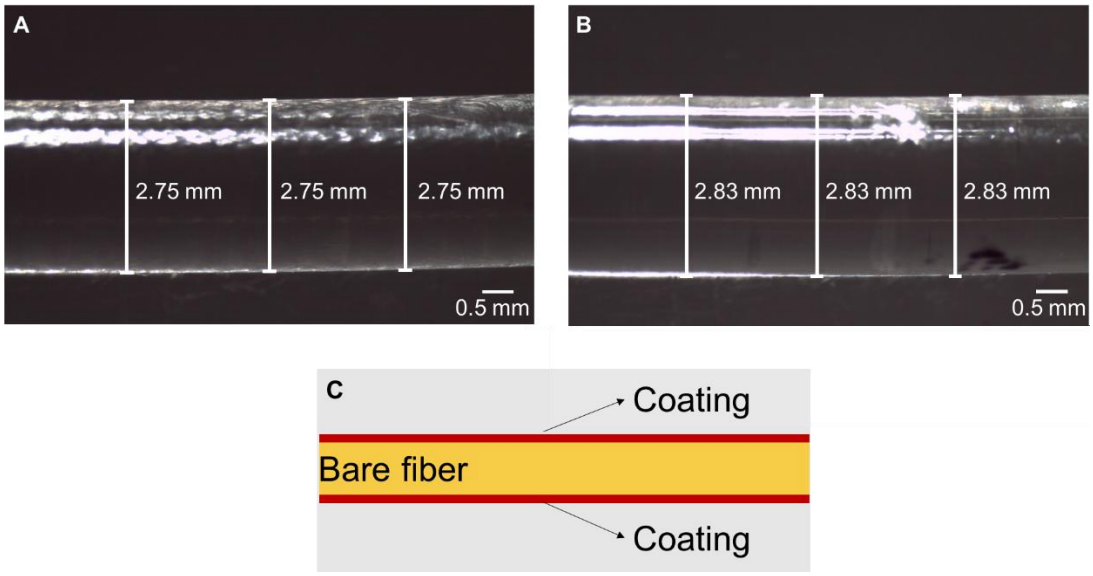

Figure 4.5 *Optical microscopy images (obtained with a stereomicroscope, EZ40 HD, Leica) of a top view of the (A) bare optical fibre and (B) a portion of the LSC surface. The figure in (C) is a scheme of the cross-section of the LSC. The thickness of the active layer is given by the total thickness of the LSC subtracting the measured thickness of the base fibre, and then dividing it by two.*

For values higher than ~40×10^{-6} m, η_{abs} ~1, meaning that an optimal value was attained and that there is no need for thicker depositions. Therefore, three LSCs with an Eu^{3+}-doped d-U(600) layer with $(42\pm3)\times10^{-6}$ m were produced. Aiming at emphasizing the role of the thickness optimization in the LSC performance, six other cylindrical LSCs with a thinner hybrid layer were manufactured, three with a thickness of $(18\pm1)\times10^{-6}$ m and three with $(21\pm2)\times10^{-6}$ m, decreasing the viscosity of the depositing solution. The Eu^{3+}-d-U(600) hybrids were also processed as thin films deposited on glass substrates ($6.00\times2.50\times0.15\ cm^3$, Normax) to allow the characterization by UV-vis absorption spectroscopy and ellipsometry, using the spin-coating conditions described in section 4.2.

As illustrated in Figure 4.4B, η_{abs} converges to the unit as the film thickness tends to ~40×10^{-6} m. Therefore, we will focus on the performance of LSCs in which the thickness of the Eu^{3+}-doped di-ureasil layer is around such value (Figure 4.5).

4.3.2 LSC characterization

The experimental techniques for the optical characterization, including photoluminescence, UV-Vis absorption and emission quantum yield are described in Appendix A.

The dispersion curve of the Eu^{3+}-doped d-U(600) hybrid material was experimentally determined through spectroscopic ellipsometry (Appendix A for details). The thickness of the substrate was considered infinite and the refractive index was obtained by direct inversion of the ellipsometric data (not shown). To describe the refractive index values the Lorentz model was used, which expresses the relative complex dielectric constant as a function of the frequency (ω) described by:

$$\varepsilon(\omega)=\varepsilon_{\infty}+\frac{(\varepsilon_{S}-\varepsilon_{\infty})\times\omega_{0}^{2}}{(\omega_{0}^{2}-\omega^{2})+i\Gamma\omega} \qquad (4.2)$$

where ε_{∞}, ε_{s}, ω_0 (eV), Γ (eV) are the high frequency relative dielectric constant, the static relative dielectric constant, the oscillator resonant frequency and the damping factor, respectively [252]. The fitting method used was described by Fernandes *et al.* in [253].

Due to the lack of commercially available PV cells with similar dimension and shape of the POF edges, the optical power at the LSC output was estimated using a commercial photodiode (Appendix A for details). To reduce the reflection within the fibre and at the photodiode interfaces an index matching gel (NyoGel® OC-431A-LVP, Nye Lubricants) was used. Nevertheless, the I-V measurements performed in the presence of the index matching gel are similar to those measured without the gel, pointing out an efficient mechanical coupling between the fibre and the photodiode. Moreover, the outcoupling of the guided light due to fibre bending is disregarded, as negligible leakage losses are reported for PMMA-derived fibres with a bending angle of 180 ° and a curvature radius higher than 3.0×10^{-2} m [254].

The electrical power at the photodiode was calculated by measuring the short-circuit current I_{sc} and the open-circuit voltage V_0. These I–V measurements were performed under AM1.5G illumination (at 1000 $W\cdot m^{-2}$) using a 150 W xenon arc lamp class A solar simulator

(Abet Technologies, model 10500). The light intensity was calibrated by adjusting the distance between the light source and the LSC, in order to get a ~35×10^{-3} m diameter illuminated field.

For the three hybrid layer thicknesses, all the measurements were performed in one representative cylindrical LSC. Accurate and reproducible values were obtained for the other cylindrical LSCs produced.

4.3.3 Results and discussion

Figure 4.6 shows the cylindrical LSC under room and UV illumination. The intense red emission, visible to the naked eyes, is ascribed to the $^5D_0\rightarrow{}^7F_{0-4}$ transitions (Figure 4.7A) and is guided, through total internal reflection, to the edges of the device. The energy, relative intensity and fwhm of the intra-$4f^6$ lines resemble those previously measured for monolithic samples [236].

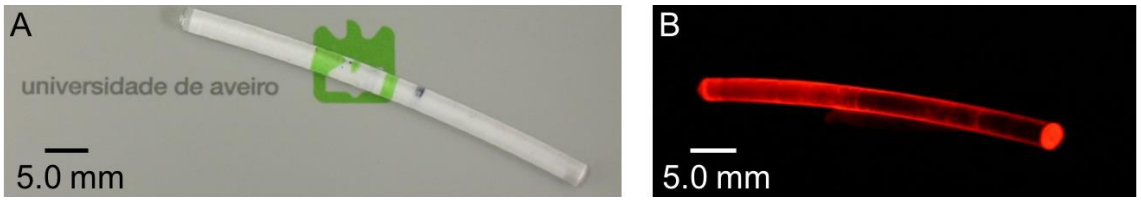

Figure 4.6 *Photograph of the LSC (A) under room illumination and under (B) UV illumination (365 nm, Spectroline E-Series UV lamp, Z169625, Sigma-Aldrich).*

The excitation spectrum was monitored within the $^5D_0\rightarrow{}^7F_2$ transition, being formed of a broad band (fwhm of ~130 nm) in the UV spectral region (300-380 nm) with two main components at ~280 nm and at ~330-370 nm, mainly ascribed to the hybrid host [255] and to the tta triplet states [52,236], respectively (Figure 4.7B)

The higher η_{yield} value found, 61.0±6.1 % (excitation wavelength range 270-400 nm), is one of the highest reported so far for Ln^{3+}-containing organic-inorganic hybrids [54,67]. The $^5D_0$ quantum efficiency (q) and η_{yield} are related by $\eta_{yield}=kq$ [256] where the rate k includes all processes involved in the efficiency of light absorption by the sensitizer, the energy transfer to the emitting state, and the decay rates populating the emitting state. In the present case k=0.82, which indicates a very efficient process of light absorption and energy transfer from the hybrid matrix and tta ligands to the Eu^{3+} ions.

Also for this case, the overlap integral was calculated to infer about the ability of the LSC to absorb the sunlight available for DS conversion through Eq. (3.18), section 3.3 [52]. The

overlap integral *O* is ~25 $W \cdot m^{-2}$ indicating that this LSC has the potential to convert 17 % of the extra sunlight intensity available for DS conversion that Si would not absorb (149 $W \cdot m^{-2}$) [2,3,13,73].

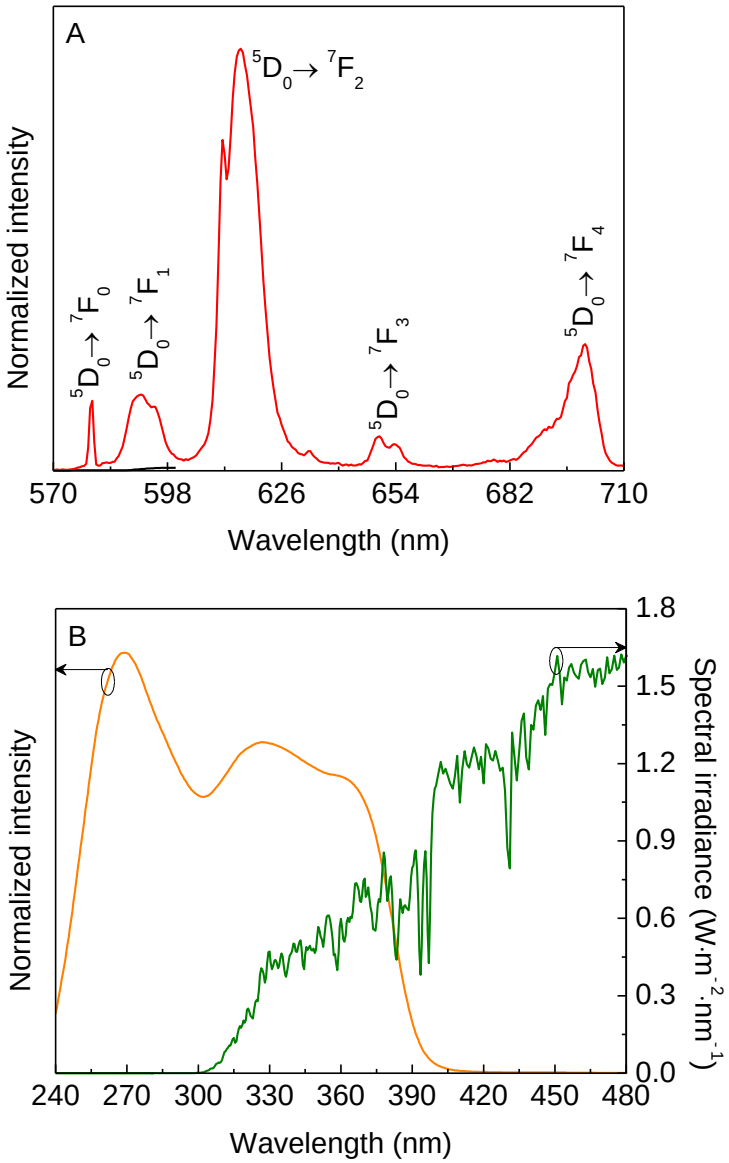

Figure 4.7 *(A) Emission spectrum of the hybrid layer excited at 360 nm and (B) excitation spectrum monitored at 615 nm, AM1.5G solar spectrum (green line) and overlap integral O (shadowed area)*

The LSC's performance were quantified measuring η_{opt} (Eq. (3.10), section 3.3), *F* (Eq. (3.9), section 3.3) and *PCE* (Eq. (3.17), section 3.3). As mentioned in section 3.3, η_{opt} is defined in different ways in the literature. In this case, we follow the definition expressed in Eq. (3.10), section 3.3 [257]. We note that despite the photodiode is coupled to a single edge, *G* is calculated considering A_e as the area of the two extremities, as it is expected the same light concentration

at each LSC end. Considering the total number of photons absorbed by the device, $\frac{\eta_{solar}}{\eta_{PV}}$=1.15 and η_{opt}=26.5±1.3 %. Aiming at compare the device performance, Table 4.1 lists η_{opt} values calculated using Eq. (3.10), section 3.3, or an identical definition, under AM1.5G solar illumination. Examples involving illumination using other standard conditions (*e.g.*, diffuse cloudy day indoor illumination [257]) are not considered. In addition, Table 4.1 includes only single-layer LSCs, as the use of stacked layers and external devices (*e.g.*, mirrors and white diffusers) boosts concentrator's performance. Moreover, Table 4.1 lists η_{opt} values calculated considering both the absorbed photons and the total incident ones, as η_{opt} depends on it. For instance, considering the total solar irradiance the value measured for the optimized cylindrical LSC η_{opt} =1.5±0.1 %.

Table 4.1 *Figure of merit of the optical conversion efficiency (η_{opt}) of single-layer LSCs. The excitation source and the absorbing spectral range of the optical active layer are also indicated.*

Active layer	***Geometry (Area, cm²)***	***η_{opt} (%)***	***Excitation source***	***Absorbing spectral range (nm)***
d-U(600)/Eu(tta)$_3$·2H$_2$O	cylindrical (*L*=5.0×*d*=0.3)	20.7[a]	Solar simulator	300-380
PMMA/Red305 [28]	planar (5.0×5.0)	16.3 [a]		400-620
PMMA/CdSe/CdS [37]	planar (21.5×1.3)	10.2[a]		350-550
Commercial laser organic dyes [258]	planar [c] (40×40)	32[a]	–	360-550
PMMA/PbS [32]	cylindrical (*L*=2.5×*d*=1.2)	6.5[b]	Solar simulator	600-920
PMMA/Lumogen F/Red305 [107]	planar (5×2.5)	2.8[b]		400-650
Red F/toluene [31]	planar (7.5×2.5)	3.4[b]		Peaks at 413
Rhodamine B/toluene [31]	planar (7.5×2.5)	2.6[b]		Peaks at 550
CdSe/ZnS/toluene [31]	planar (7.5×2.5)	0.3[b]		300-650
PbS/toluene [43]	planar (4.5×1.2)	1.4[b]		400-850
PMMA/Oxazine 750/benzene [259]	planar (15.3×7.5)	~6.0[d]	daylight	–

GLYMO=3-glycidoxypropyltrimethoxysilane; L=length; d=diameter; η_{opt} was calculated considering the a) absorbed optical power and b) total incident power. c) It is not clear if the η_{opt} value reported arises from a single- or a double-layer planar device. d) Average value obtained during one year. For the references [258] and [259] no complete information is provided.

To have a closer estimation of the η_{opt} values in daylight conditions, the mismatch in the UV spectral region between the AM1.5G solar irradiance and that of the Xe lamp of the solar simulator used (Figure 4.8) should be taken into account. Then, replacing $I_{AM1.5G}$ in Eq. (3.10), section 3.3, by the emission spectrum of the solar simulator (including the contribution in the UV range down to 250 nm, inset Figure 4.8), we have $\frac{\eta_{solar}}{\eta_{PV}}$=0.9 and corrected η_{opt} values of 20.7±1.3 % and 1.2±0.1 %, considering the absorbing region ($53\ W{\cdot}m^{-2}$) and the total AM1.5G spectrum ($1000\ W{\cdot}m^{-2}$), respectively. We should note, however, that this procedure is not habitually adopted in the literature. Generally, no information about the irradiance of the solar simulator used is provided. The large majority of the reported efficiency values reported using a solar simulator are uncorrected by the potential mismatch between the AM1.5G solar irradiance and that of the Xe lamps used. Thus, we include in Table 4.1 the excitation source employed to simulate the solar AM1.5G solar irradiance and the absorbing region of the optical layer.

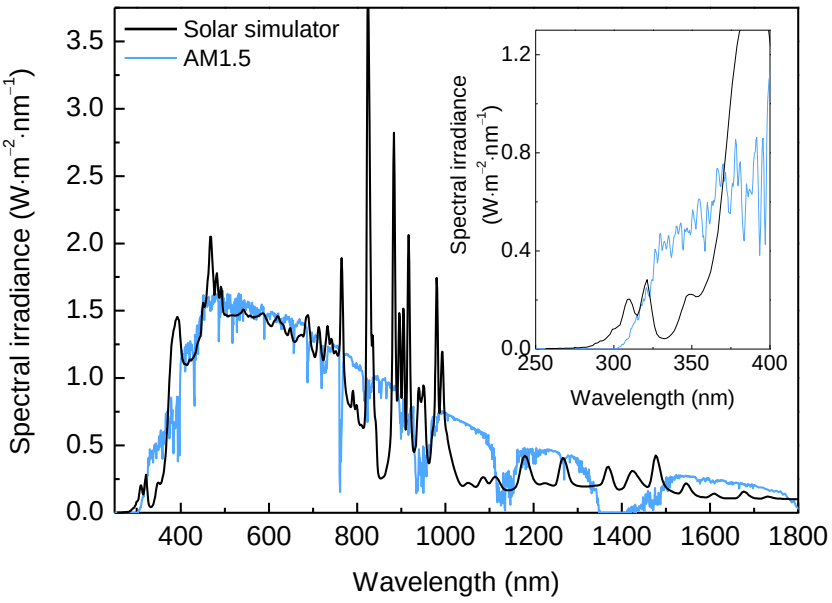

Figure 4.8 *Spectral irradiance of the Abet Technologies model 10500 solar simulator (black line) and of the standard AM1.5 (blue line) spectra. The inset shows a magnification in the UV region (250-400 nm).*

In any case, we emphasize that the calculated η_{opt} values are attained for a LSC device that is essentially transparent in the visible spectral region. This is an essential requirement for building integrated applications, as recently highlighted for CdSe and CdS QDs in PMMA in which η_{opt} =10.2 % or 1.0 %, depending if we consider the absorbing region (350-550 nm) or

the total AM1.5G solar irradiance, respectively [37]. We may thus conclude that the η_{opt} values here reported are among the larger ones known for UV-excited transparent LSCs (rigid and flexible with planar and cylindrical geometries and incorporating dyes, QDs or Ln^{3+} ions, Table 4.1). The concentration factor F~1 (with G~4), is also one of the highest reported so far for cylindrical LSCs (*e.g.* F~0.27 for PbS QDs-doped PMMA hollow cylindrical LSCs [32]).

The photostability of the LSC was assessed by measuring the I_{SC}^{L} under continuous AM1.5G illumination. The temporal relative variation of the short-circuit current (ΔI_{SC}^{L}) reveals that the LSC is stable with a minor variation (ΔI_{SC}^{L}~0.5 %) after 8 h. In agreement to the model used to optimize the LSC design (section 4.3.1), η_{opt} decreases with decreasing the hybrid layer thickness below the optimum value (~40×10^{-6} m). In fact, an average η_{opt} value of 15.7±1.3 % (in the absorbing region, 300-380 nm) was measured in the LSCs fabricated with an average hybrid coating thickness of $(20\pm1)\times10^{-6}$ m.

The *PCE* was calculated by Eq. (3.17), section 3.3, considering FF=0.75. The calculated *PCE* values are 3.6±0.2 % and 0.20±0.01 %, considering the irradiance values in the Eu^{3+} absorption region (300-380 nm) and in the total AM1.5G solar irradiance. Similarly to that discussed for the η_{opt} calculation, the *PCE* must also be corrected for the spectral mismatch between the AM1.5G and solar simulator irradiance spectra (Figure 4.8), yielding *PCE* values of 2.5±0.2 % and 0.14±0.01 %, taking into account the absorbing region and the total solar irradiance, respectively.

These values, the first *PCE* quantification for cylindrical LSCs, are of the same order of magnitude than the ones that can be found in literature for planar LSC measured with a Si photodiode (0.46-0.57 %) [17]. In accordance to that above mentioned for the case of η_{opt}, *PCE* will vary with the illumination conditions and the use of mirrors at the sides or backside, adding the fact that *PCE* will be strongly dependent on the number and type of detectors coupled to the LSC. Therefore, unless the same photodiode (or PV cell) was used, comparison between values cannot be made.

As previously mentioned in section 3.3, the η_{opt} measured values can be rationalized through Eq. (3.7), section 3.3. Once again, we will consider that η_{SA} and η_{tr} are equal to the unity, because of the transparency of the d-U(600) di-ureasil in the visible spectral region [250]. The dispersion curve for the refractive index of Eu^{3+}-doped d-U(600) was estimated considering

a layered structure model composed of the substrate, the hybrid layer and air as ambient medium, yielding to the refractive index dispersion curve in Figure 4.9.

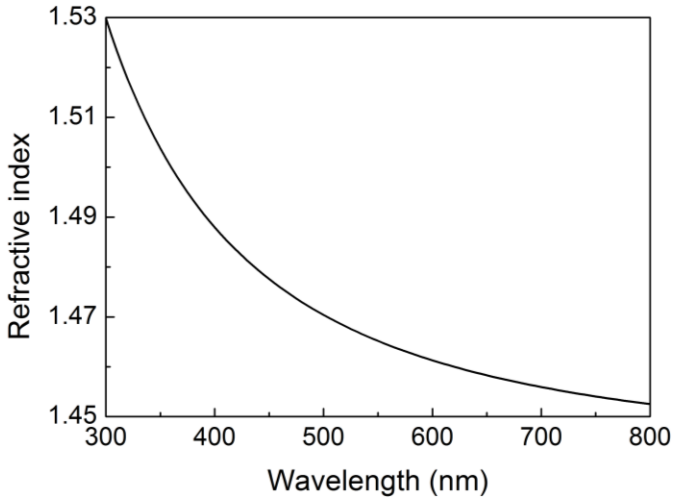

Figure 4.9 *Refractive index dispersion curve of the Eu^{3+}-doped hybrid optically active layer.*

From Eq. (2.7), we get η_{opt}=22±1 %. This value compares well with that experimentally measured through Eq. (3.4), η_{opt}=20.7±1.3 %, stressing the appropriateness of this procedure. Moreover, this agreement points out that the assumptions made concerning η_{SA} and η_{tr} being close to the unit are adequate (contrarily to that found in the planar Eu^{3+}-based LSC for which η_{tr}=0.40 [54]).

4.5 Conclusions

The described planar LSC displays η_{opt}, F and PCE values of ~3 %, 0.09 and 0.007 %, respectively, under UV irradiation at 365 nm. Also, the fabricated LSC presents self-absorption and trapping efficiencies close to the unit pointing out negligible self-absorption and transport losses. We should call the attention for the fact that this LSC is made of glass that remains transparent even after the application of the luminescent coating, which is can be seen as ideal for PV windows applications.

The short-length cylindrical LSCs showed more promising results. The optimized cylindrical LSC displays effective η_{opt} and PCE values of 20.7±1.3 % and 2.5±0.2 %, respectively, considering the absorbed photons in the 300-380 nm range and taking into account the spectral mismatch in the UV spectral region between the AM1.5G solar irradiance and that of the Xe lamp of the solar simulator.

Although those values decrease to 1.2±0.1 % (η_{opt}) and 0.14±0.01 % (*PCE*) when considering the total AM1.5G incident radiation, they are among the higher ones reported for transparent UV-excited LSCs. All these results underline the great potential of this innovative procedure to fabricate high-efficiency, lightweight, flexible and cost-effective waveguiding photovoltaics. Indeed, the use of low attenuation POFs envisages the possible fabrication of longer LSCs with larger *G* and *F* values. High *G* values will allow the reduction of the PV area, decreasing concomitantly the general cost per unit of generated energy. Unlike conventional planar LSCs, usually made of rigid glass or plastics with limited mechanical flexibility, this cylindrical LSC design can be implemented in ultrathin, mechanically bendable formats allowing high-efficiency flexible waveguiding photovoltaics (as, for instance, the integration in a single structure of poly-Si PV cells, a PDMS waveguide, a TiO_2-doped backside reflector and a microlens array to increase the light harvesting ability [260]). The LSC structures may open new opportunities for cost-effective sunlight collection and wearable solar-harvesting fabrics for mobile energy making LSCs market competitive.

The intriguing results achieved for fibre-based LSCs compared to that of planar ones, drove the work to optimize and develop new cylindrical LSCs.

Chapter 5. Fibre-based LSCs in the NIR-visible

5.1 Introduction

Most of the LSCs in the literature are based on luminescent species with visible emission (mostly organic dyes) [18,23,28,47,80,82,89,93-108], which is not the wavelength range correspondent to the maximum efficiency for c-Si PV cells, due to their bandgap of ~1.1 eV. Thus, red-shifting of the emission range of optically active centres used in LSCs to the NIR has clear advantages.

Theoretical works focus the potential of NIR-emitting LSCs based on semiconducting QDs [35,36,46,261,262], pointing out that the optical conversion efficiency may reach values up to 14.6 % [262]. Nevertheless, very few reports experimentally quantify the performance of planar NIR-based LSCs, in which the optical active layers are based on QDs of PbS [32,43], PbS/CdS [48] and CISeS/ZnS [34], with η_{opt} values below 6.1 % [48]. Despite the absence of η_{opt} values, NIR-emitting LSCs based on hexanuclear metal halide clusters [63] and on a cyanine derivative [29] were also demonstrated.

The latter mentioned works also reported *EQE* curves to highlight that they resemble the absorption spectra of the active layers, rather than to make a comparison with the *EQE* of the bare PV cell in use [29,63]. Even for visible emitting LSCs, which represent the most part of LSCs reported in the literature, *EQE* values are not analysed in terms of increase in the PV cell efficiency [42,65,107,245].

Given the importance of the geometry of the LSCs in its performance and following the previous results for cylindrical LSCs, here we will combine cylindrical and visible-NIR emitting LSCs, with short length (~10×10^{-2} m) based on hollow-core POFs with triangular shape (Figure 5.1 and Figure 5.2). The geometry was chosen with the objective of allowing an easier coupling between the LSCs, giving the possibility of having a bundle structure, with each hollow-core POF behaving as an individual LSC [27] with optimized coverage of a square PV cell. Considering a square PV cell with surface dimensions 2.0×0.2 cm^2, and a bundle of cylindrical LSCs with d= 0.2 cm, the maximum number of LSCs that could be coupled to the PV cell would

be 10; otherwise, if we consider a bundle of triangular LSCs, each side of the triangle with 0.2 cm, the maximum number of LSCs that could be coupled to the PV cell should be 20. Using these example dimensions, the overall covered area of the PV cell would be 0.31 cm^2 and 0.34 cm^2 for the cylindrical and triangular LSCs bundle, respectively. The portion of the PV cell not covered would correspond to ~22 % and ~15 % of its total area. Thus, by using the triangular geometry instead of the cylindrical one, the coverage of the PV surface could be improved in ~7 %.

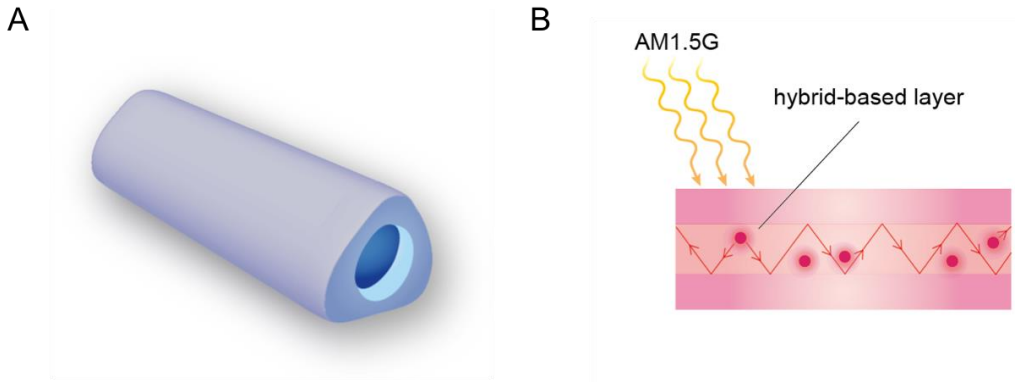

Figure 5.1 *Schematic representation of the (A) fabricated LSC made of hollow-core POFs and (B) of the LSC working principle. The optical active layer is the Eu^{3+}-, Rh6G- or Rh800-doped t-U(5000) organic-inorganic hybrid embedded into its hollow core.*

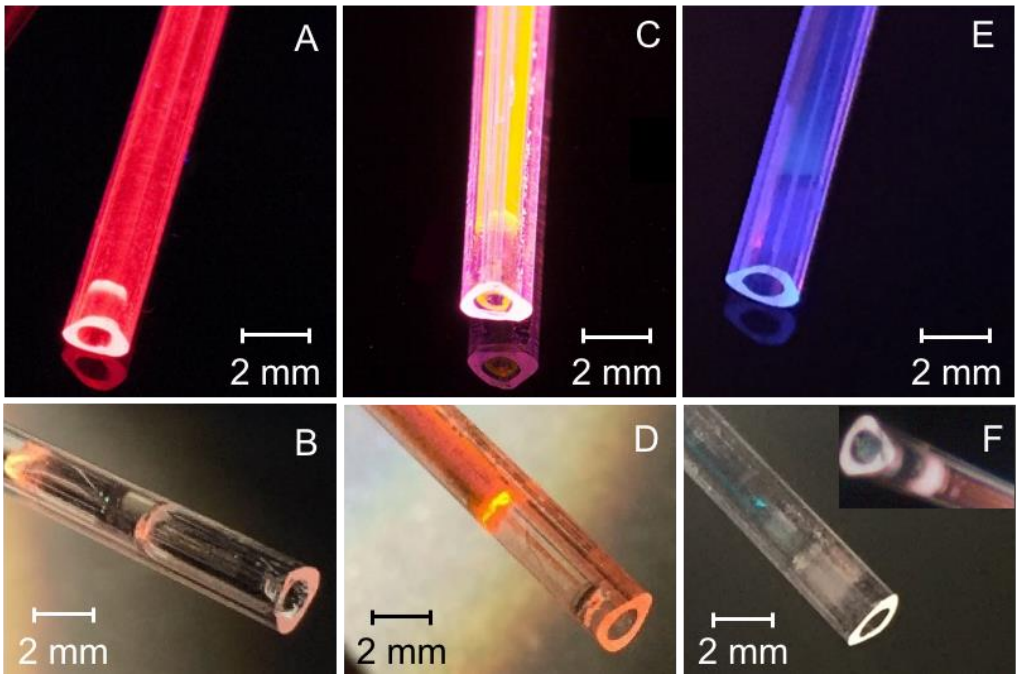

Figure 5.2 *Fabricated (A,B) Eu-LSC, (C,D) Rh6G-LSC and (E,F) Rh800-LSC under UV radiation at 365 nm (top) and solar simulator AM1.5G irradiance (bottom). The inset on (F) is a photograph of the Rh800-LSC taken with an infrared camera.*

The LSCs were placed side by side to fabricate a bundle in such a way that the exposed area is maximized. Although bundles of fibre LSCs have already been suggested [249], this is the first time a LSC bundle structure is coupled to a PV cell with characterization of its electrical performance in terms of *EQE* gain comparing with the bare PV cell. The LSCs core is circular and filled with t-U(5000) tripodal organic-inorganic hybrid (Figure 2.1B, section 2.1) modified with PTMS and doped with $Eu(tta)_3 \cdot 2H_2O$ complex (Figure 2.2B, section 2.1), Rh6G (Figure 2.2C, section 2.1) or Rh800 (Figure 2.2D, section 2.1). These hollow-core LSCs confer mechanical and environmental protection of the optical active layer, which is an advantage for real outdoor applications.

The bundle structure performance was evaluated by *EQE* measurements of the PV cell when coupled to the Eu, Rh6G and Rh800 bundles, respectively. The Si PV cell *EQE* absolute increase was ~50 % in the 300-400 nm range, higher than the record value of 40 % reported for a DS layer based on Lumogen 300 organic dye dispersed in PMMA on a Si PV cell [263].

5.2 Hollow-core LSCs fabrication

The hollow-core POFs were fabricated in UNESP - Institute of Chemistry, São Paulo State University, using a semi-industrial fibre optic manufacturing facility designed to draw optical fibres (described in detail in the next chapter, section 6.2). The hollow-core was filled with t-U(5000) hybrid doped with Rh800, Rh6G or $Eu(tta)_3 \cdot 2H_2O$ complex, using a syringe. The hybrid layers have an average thickness of $(1.11 \pm 0.03) \times 10^{-3}$ m (Figure 5.3). The average edge area of the PMMA portion of the POFs were estimated using ImageJ 1.50i software, giving values of $(1.41 \pm 0.03) \times 10^{-6}$ m^2 (Figure 5.4). The devices will be designated as Rh800-LSC, Rh6G-LSC or Eu-LSC, as to represent the hollow-core fibre filled with Rh800, Rh6G or $Eu(tta)_3 \cdot 2H_2O$-doped t-U(5000), respectively.

The LSCs were placed side by side to fabricate a bundle in such a way that the exposed area is maximized. Although bundles of fibre LSCs have already been suggested [249], this is the first time a LSC bundle structure is coupled to a PV cell with characterization of its electrical performance in terms of *EQE* gain comparing with the bare PV cell. The LSCs core is circular and filled with t-U(5000) tripodal organic-inorganic hybrid (Figure 2.1B, section 2.1) modified with PTMS and doped with $Eu(tta)_3 \cdot 2H_2O$ complex (Figure 2.2B, section 2.1), Rh6G (Figure 2.2C, section 2.1) or Rh800 (Figure 2.2D, section 2.1).

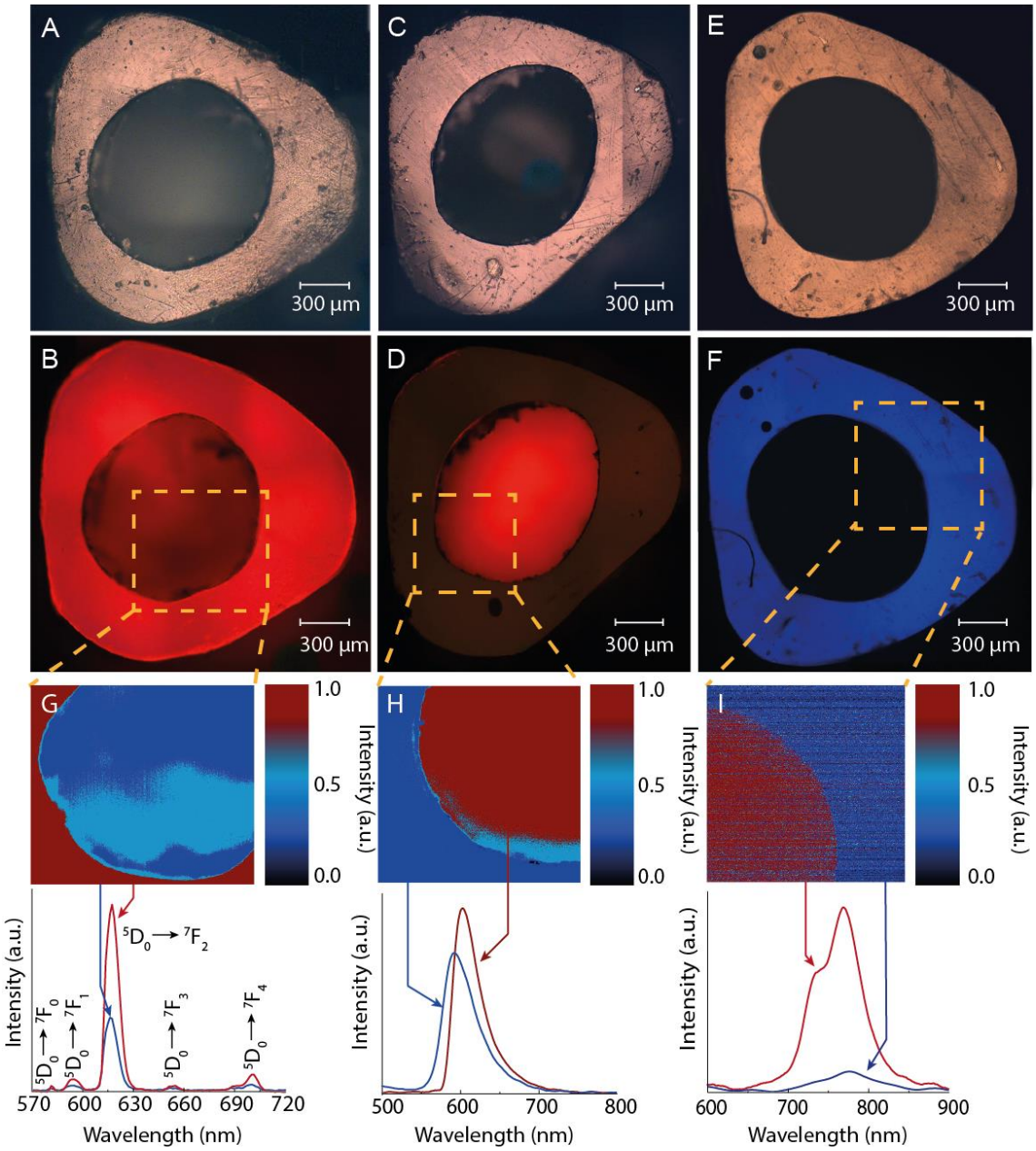

Figure 5.3 *Cross-section optical microscopy images of the (A,B) Eu-LSC, (C,D) Rh6G-LSC and (E,F) Rh800-LSC under white light illumination (A,C,E) and UV irradiation at 365 nm (B,D,F). Hyperspectral camera images of selected areas of (G) Eu-LSCs, (H) Rh6G-LSCs and (I) Rh800-LSCs and respective emission spectra in the core and POF regions are also presented.*

Optical microscopy images were obtained using the equipments described in Appendix A. The η_{opt} and *EQE* were estimated using a photodiode (normalized response curve provided by the manufacturer is presented in Figure 5.5) and a monocrystalline silicon PV cell when working with the bundles, respectively, according to the details and coupling scheme described in Appendix A.

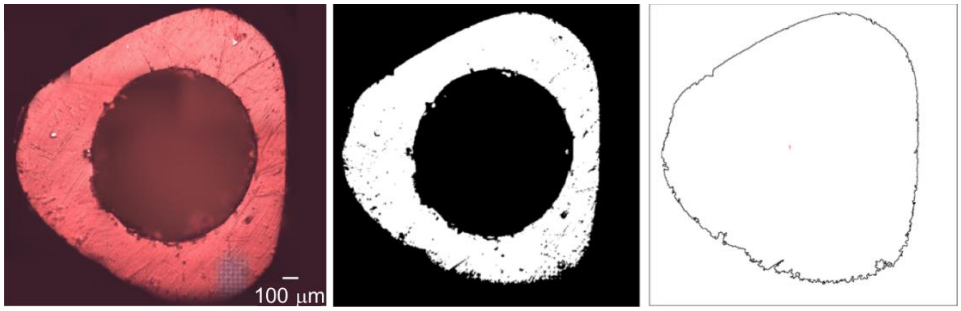

Figure 5.4 *ImageJ software steps to perform the edge area calculation.*

5.4 Results and discussion

Figure 5.2 and Figure 5.3 show the LSCs under UV illumination and solar simulator AM1.5G radiation. The emission that is guided through total internal reflection to the edges of the device is ascribed to the $^5D_0 \rightarrow {}^7F_{0-4}$ transitions for Eu-LSC and that of Rh6G- and Rh800-LSC is attributed to the dyes fluorescence (Figure 5.5A).

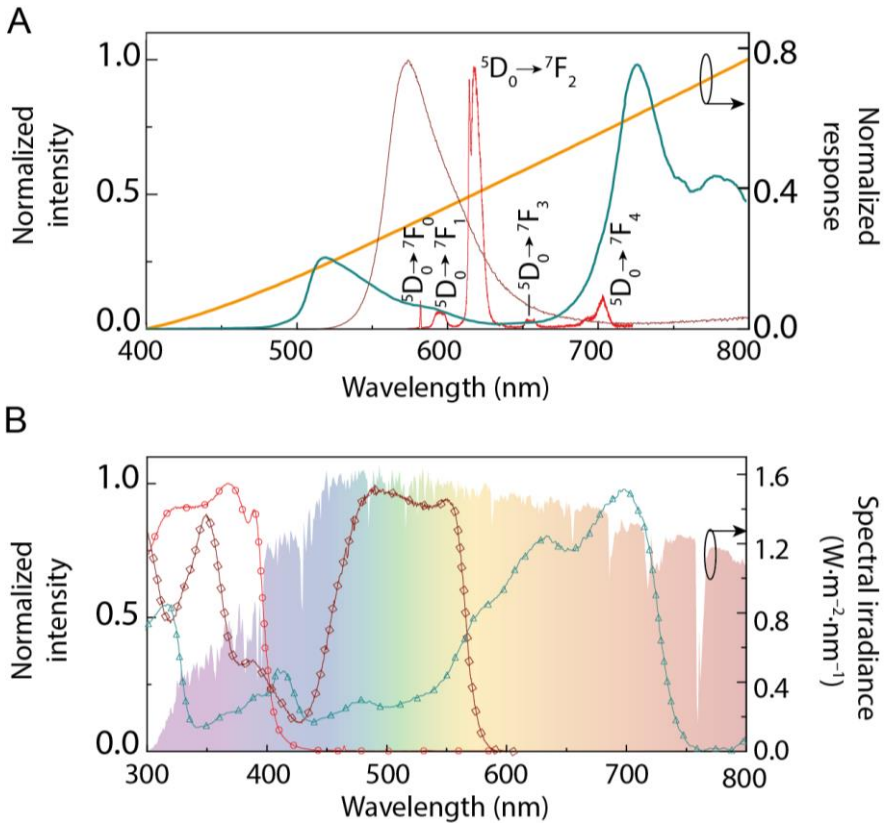

Figure 5.5 *(A) Emission spectra excited at 370 nm, 480 nm and 620 nm for Eu-LSCs (solid red line), Rh6G-LSCs (solid brown line) and Rh800-LSCs (solid blue line), respectively. The orange line is the normalized response curve of c-Si photovoltaic devices. (B) Excitation spectra monitored at 615 nm, 590 nm and 715 nm for Eu-LSCs (red circles), Rh6G-LSCs (brown squares) and Rh800-LSC (blue triangles), respectively, and AM1.5G spectral irradiance.*

The excitation spectra of the dye-doped hybrid layers were monitored within the emission peak position, namely around 590 nm and 715 nm, for Rh6G- and Rh800-LSC, respectively, and within the $^5D_0 \rightarrow {}^7F_2$ transition for the Eu-LSC (Figure 5.5B). The excitation spectra of the Rh6G- and Rh800-LSC overlaps the hybrid host excitation region (240-450 nm) and present broad bands (450-550 nm for Rh6G-LSC and 550-720 nm for Rh800-LSC) ascribed to direct excitation of the dye related states that result in the formation of *J*-dimers [264,265]. In the case of the Rh800-LSC, the excitation spectrum presents a shoulder at ~630 nm and peaks at ~690 nm. The absence of the emission bands typically of the undoped host [232] in the emission spectra of the LSCs points an effective hybrid-to-optically active centre energy transfer [266].

The optically active layers were also characterized in terms of η_{yield}, with values of 0.89±0.09 and 0.21±0.02 (excitation at 320 nm) for Eu- and Rh800-LSCs, respectively, and 0.95±0.10 (excitation at 560 nm) for Rh6G-LSC.

In order to quantify the ability of the LSCs to absorb the sunlight available for conversion, we calculate the overlap integral, given by Eq. 3.8, section 3.3. The larger values for the overlap integral were found for the Rh800-based hybrids, with a value of 230 $W \cdot m^{-2}$ compared with 44 $W \cdot m^{-2}$ and 196 $W \cdot m^{-2}$ found for the Eu- and Rh6G-based ones. If I_x is replaced by absorbance (A) values (Figure 5.6A), similar overlap integral values are found, according to the approximation discussed in section 3.3. We should note that, from the 46 $W \cdot m^{-2}$ of the AM1.5G spectrum, correspondent to the spectral irradiance between 300 and 400 nm, which typical Si PV cells would not absorb, the Eu-, Rh6G- and Rh800-based hybrids would harvest 88 %, 51 % and 19 %, respectively. Despite the fact that Rh800-based active layer presents less ability to absorb the radiation that Si PV cells would not absorb and less ability to convert the harvested sunlight (lower η_{yield}) than Eu- or Rh6G-based active layers, it will convert it to the NIR range, which is the region of Si PV cells maximum response.

Following the approach described in section 3.2, light propagation will be discussed as function of the active layer being Eu-, Rh6G- or Rh800-based, taking into account the refractive index contrast, $\Delta n_{i,j} = n_i - n_j$ with i,j=1,2,3, between the (1) air, (2) hybrid layer and (3) PMMA [239]. As highlighted in sections 3.1 and 3.2, when the incident radiation is absorbed and re-emitted, two main mechanisms may contribute to optical losses: the escape cone, that accounts for losses at the surface and the absorption within the optically active layers themselves.

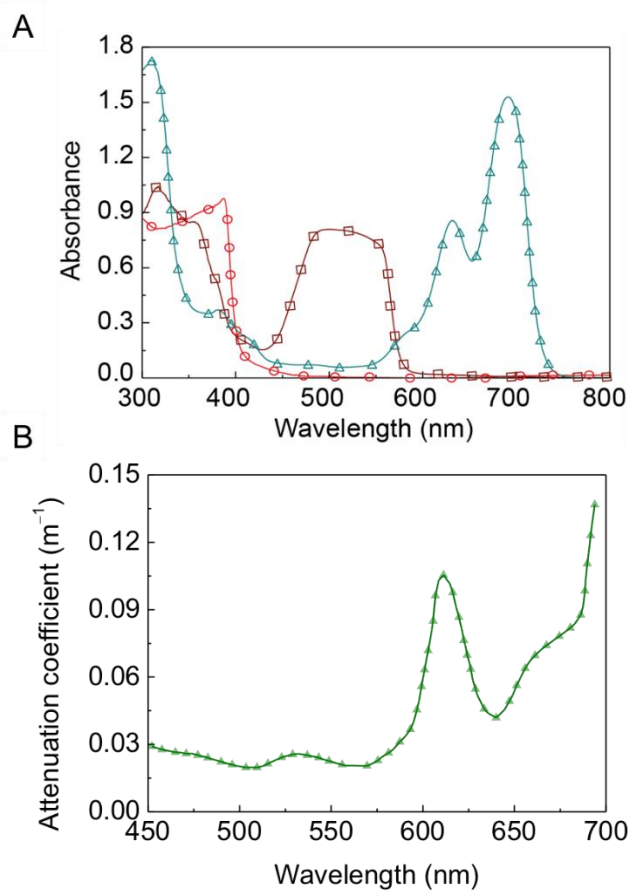

Figure 5.6 *(A) Absorption spectra of the Eu-LSC (red circles), Rh6G-LSC (brown squares) and Rh800-LSC (blue triangles) optically active layers and (B) attenuation coefficient curve for PMMA POFs [267].*

The refractive index dispersion curves for the hybrids and of the PMMA are shown in Figure 5.7A. For the Eu- and Rh800-based LSC, $\measuredangle n_{2,3}$ is very small as the refractive index values of the hybrid and POF are very close, yielding η_{trap}~73 %, meaning that the remaining light will be lost through the escape cone. In these cases, it is expected that propagation of converted radiation would occur mostly in the PMMA that in the hybrid layer, which is true for Eu-LSCs (emission intensity 2.5 times higher in the PMMA than in the hybrid layer, Figure 5.3) but, for Rh800-LSCs, due to the increased PMMA attenuation in the Rh800 emission range (Figure 5.6B), light propagation is more intense in the hybrid layer by a factor of 5.5 (Figure 5.3). For the Rh6G- LSC, the PMMA refractive index is lower than the active layer one, thus, trapping will occur in the PMMA and also in the hybrid layer, yielding η_{trap}~78 %. The light confinement will occur in the hybrid and PMMA layers and only in the hybrid layer for photons emitted within $82° < \theta_c \leq 90°$, and thus the emission intensity in the hybrid and in the PMMA layers is approximately the same (Figure 5.3).

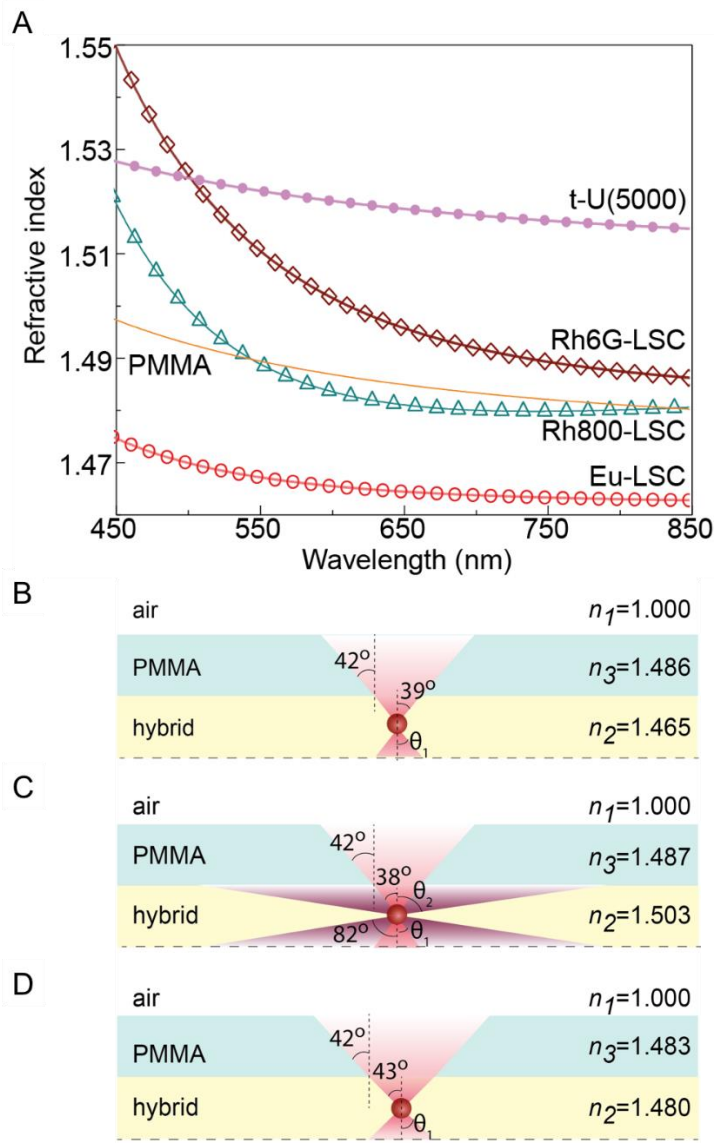

Figure 5.7 *(A) Refractive index dispersion curves for the LSCs optically active layers, POF and undoped t-U(5000) organic-inorganic hybrid and schematic representation of the cross section of the hollow-core LSCs with the escape cones and light trapped in the POF and hybrid (θ_1) and only in the hybrid (θ_2) for (B) Eu-LSC, (C) Rh6G-LSC and (D) Rh800-LSC. The critical angles θ_c are also indicated.*

Since the diameter of the hybrid layer is ~$1.11\pm0.03\times10^{-3}$ m, the same order as the PMMA thickness, the probability of absorption of the emitted photons with higher order modes (photons emitted with an angle closer to θ_c) is increased, due to the fact that the optical path is greater for these photons than for the lower mode ones. Furthermore, there is an additional attenuation of the optical signal evanescent electromagnetic field propagated through the PMMA. In summary, the light is also guided within the hybrid layer, besides the PMMA cladding. Thus, the discussion of the light propagation must also take into account the absorption spectra of the hybrid and PMMA layers, shown in Figure 5.6.

As the hybrid layer contributes larger for the light guidance, additional losses are predicted as the absorption coefficient of the hybrid material is larger than that of POF (Figure 5.6). Thus, light will travel a shorter length compared to the total length of the LSCs fabricated. Such length was experimentally quantified by a "piano" test [49], in which the LSCs were covered by pieces of black paper cut into 1 cm-wide piano-key-like strips. The P_{out} was quantified under natural daylight conditions as function of the distance, L, of the illuminated area to the detector (Figure 5.8). Due to the short length of the LSCs, the data were analysed in logarithmic scale and fitted to a linear function, in which the slope would be considered as the LSC attenuation coefficient (α_{at}). Therefore α_{at} is ~26.4 m^{-1}, ~26.2 m^{-1} and ~28.7 m^{-1} for Rh6G-LSC, Eu-LSC and Rh800-LSC, respectively. For all types of LSCs fabricated, Rh6G-, Eu- or Rh800-based LSCs, the effective length L_c (equivalent length for a fibre without attenuation) is ~3.0×10^{-2} m. The fibre maximum effective L_c was estimated to be ~4.0×10^{-2} m by replacing the α_{at} values into the following equation:

$$L_c = \lim_{L\to\infty} \frac{(1-e^{-\alpha_{at}L})}{\alpha_{at}} \qquad (5.2)$$

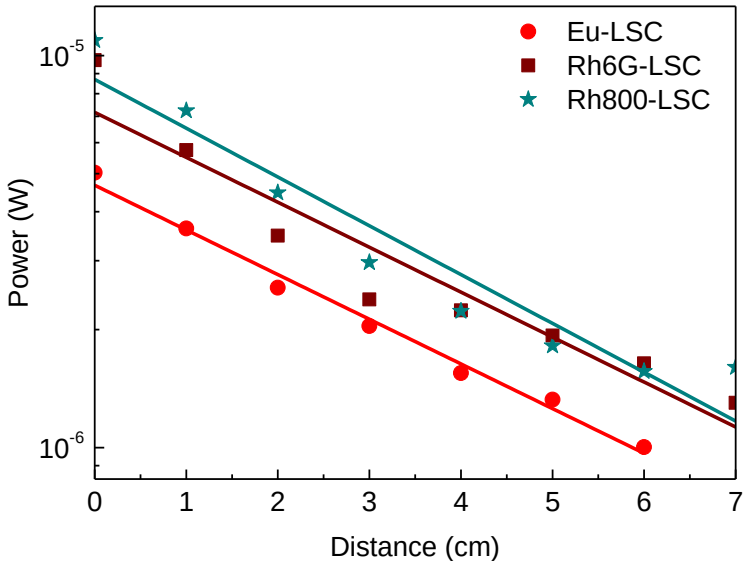

Figure 5.8 *Output power as function of the distance measured in the "piano" test [49]. The solid lines correspond to the data best fit (R^2>0.90). The data is in logarithmic scale.*

The experimental η_{opt} values were determined by illuminating the top surface of the LSCs with natural daylight illumination (~690 $W\cdot m^{-2}$). We should note that the dependence of optical path on the geometry is weighted through the G parameter, by considering in the calculus of A_s the L_c value for each LSC and A_e as the area of the two edges, as it is expected the same light

concentration at each LSC end. Considering the total incident spectral range, the η_{opt} values were 3.4 %, 1.3 % and 1.5 % for Rh6G-, Eu- and Rh800-LSC, which are of the same order of the η_{opt} values reported for LSCs based on organic-inorganic hybrids (Table 1.1).

Aiming at comparing the performance of the fabricated NIR LSC with the very few works in the literature, the alternative η_{opt} expression in Eq. (3.14), section 3.3 was used, yielding a η_{opt} value of ~4.3 % for the Rh800-LSC. This value is of the same order of the ones known for NIR-emitting transparent LSCs based on PbS QDs in a toluene solution, η_{opt}=1.4 % [43], or embedded in PMMA, η_{opt}=6.5 % [32], and PbS/CdS QDs in poly(laurylmethacrylate), η_{opt}=6.1 % [48]. Meinardi *et al.* [34] reported a CISeS/ZnS-based NIR LSC with η_{opt}=3.27 % without, however, mentioning the definition behind it.

The triangular design of the LSCs fabricated allows an easier coupling between them, giving the possibility of having a bundle structure, with each fibre behaving as an individual LSC [27]. The LSCs were placed side by side to fabricate a bundle in such a way that the exposed area is maximized (Figure 5.9). Additionally, as an attempt of having a LSC with the ability of working in a wider range of c-Si PV cell spectral response, a bundle incorporating simultaneously Eu-, Rh6G and Rh800-based LSCs was also fabricated.

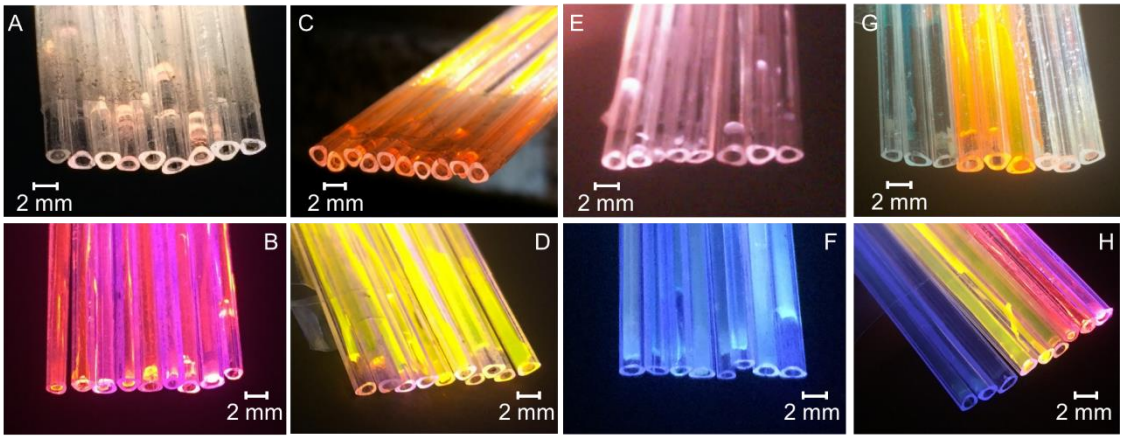

Figure 5.9 *Photographs of the bundles of (A,B) Eu-LSCs, (C,D) Rh6G-LSCs, (E,F) Rh800-LSCs and (G,H) bundle incorporating simultaneously Eu-, Rh6G- and Rh800-LSCs under AM1.5G radiation (top) and UV radiation at 365 nm (bottom). The photograph on (E) was taken with an infrared camera.*

For the bundles, the performance was evaluated in spectral terms by measuring the I_{sc} values and calculating the *EQE* of the c-Si PV cell coupled to the bundles (through Eq. (3.18), section 3.3) and compare those results with the bare c-Si PV cell *EQE* curve (Figure 5.10). As

can be noticed in Figure 5.10A-D, for all the bundles fabricated, the PV cell *EQE* is well correlated to the excitation spectra of the active layers.

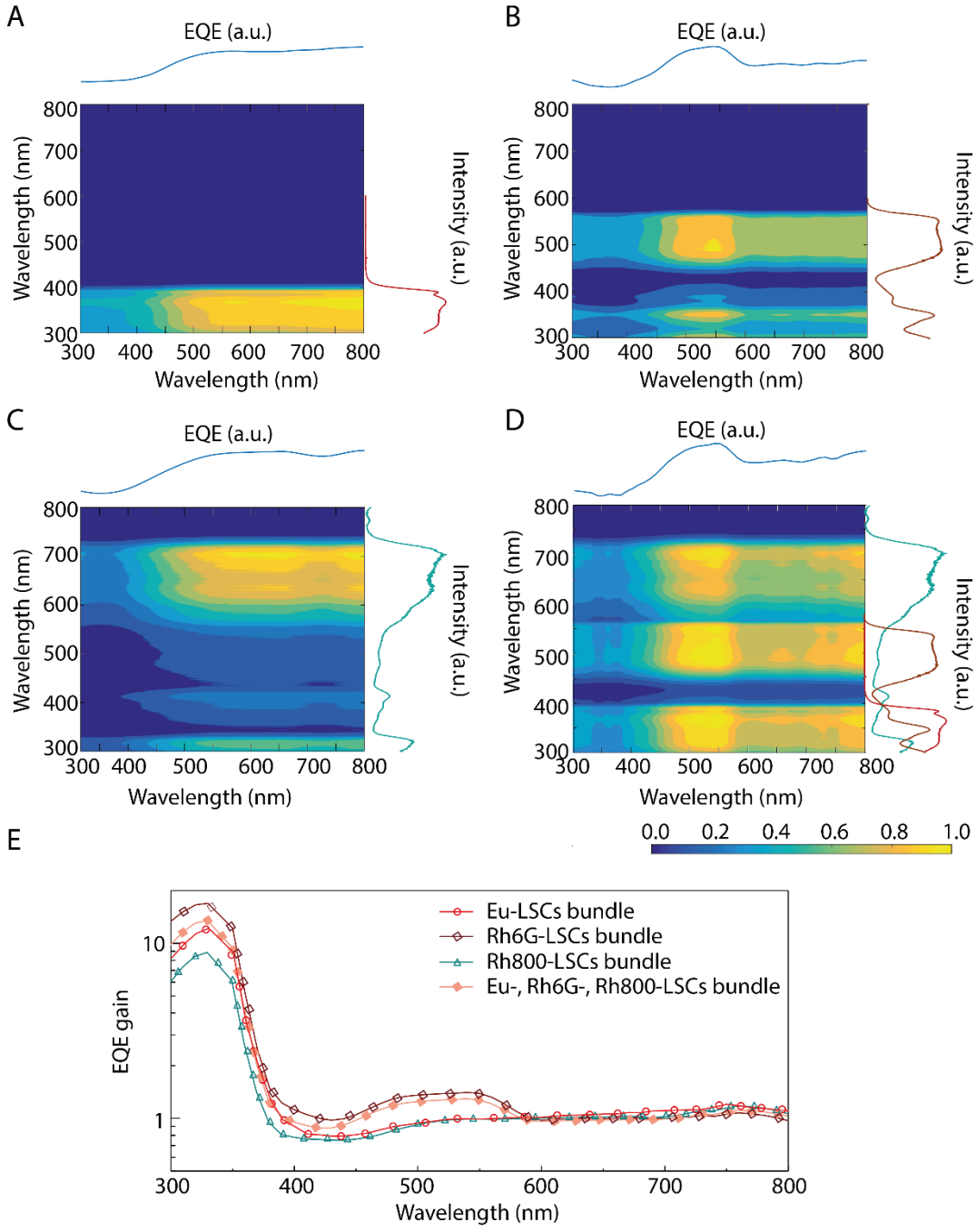

Figure 5.10 *Cross correlation between PV cell EQE and the excitation spectra of the coupled bundle active layer in the presence of the (A) Eu, (B) Rh6G and (C) Rh800 bundles. The same results for the bundle incorporating simultaneously Eu-, Rh6G- and Rh800-LSCs are also presented in (D). The EQE gain (in logarithmic scale) of the Si PV cell when coupled to the bundles is shown in (E).*

The *EQE* gain was estimated by calculating the ratio between the *EQE* of the c-Si PV cell coupled to each bundle (normalized to the *EQE* curve of the bare c-Si PV cell) and the *EQE* of the bare c-Si PV cell:

$$EQE\ gain = \frac{EQE_{PV\,cell\text{-}bundle}}{EQE_{PV\,cell}} \tag{5.3}$$

The *EQE* gain variation according to the incident wavelength radiation is presented in Figure 5.10E. The *EQE* gain is more noticeable in the UV region (up to 17 for the Rh6G-LSCs bundle) for all the bundles tested, since it is the range where Si PV cells have lower performance. Furthermore, for the Rh6G, Rh800 bundles and for the bundle incorporating all types of LSCs, an increase of *EQE* in the visible region can also be observed (Figure 5.10). However, it can also be seen a small loss in the *EQE* in the 400-500 nm range, which can originate from parasitic absorption (Figure 5.6A) of the active layers. Despite that, the overall *EQE* of the PV cell increased 8 %, 20 % and 4 % when coupled to the Eu, Rh6G and Rh800 bundles, respectively. For the bundle with Eu-, Rh6G- and Rh800-based LSCs, the overall *EQE* increase was 14 %, showing that, in these conditions, there is no advantages of using such configuration, comparing with the bundle with the Rh6G-based LSCs. As far as we know, there are no comparable studies in the literature and, so, we compare to reported DS layers. The maximum obtained value in this work is 20 %, correspondent to an absolute *EQE* increase of ~50 % in the 300-400 nm range, higher than the 40 % absolute increase recently reported for a down-shifting layer based on Lumogen 300 organic dye dispersed in PMMA on a Si PV cell [263]. We should note that, when performing these measurements, due to limitations of the setup used, the bundles were not illuminated in their full length.

5.5 Conclusions

A new geometry for hollow-core LSCs was presented, whose core was filled with a tripodal organic-inorganic hybrid doped with an Eu^{3+} complex, Rh6G and Rh800. The Rh800 dye allowed the fabrication of NIR emitting LSCs, which are scarce in the literature. For the first time, the produced LSCs were assembled to form a bundle structure, coupled to a Si PV cell and characterized in terms of electrical performance.

We verify an increase of Si PV cell *EQE* values at the energy values corresponding to the excitation spectra of the optically active layers, being the *EQE* gain more evident in the UV region, which is the range that Si PV cells present lower performance. An overall increase of

8 %, 20 % and 4 % of the PV cell when coupled to the Eu, Rh6G and Rh800 bundles, respectively, was obtained. The correspondent absolute *EQE* increase in the 300-400 nm range was ~50 %, higher than the 40 % value reported for a down-shifting layer based on Lumogen 300 organic dye dispersed in PMMA on a Si PV cell [263]. Additionally, a bundle incorporating simultaneously Eu-, Rh6G- and Rh800-LSCs was fabricated, but with no advantages over the Rh6G-LSCs bundle (overall *EQE* gain of 14 %). We should note that, when performing these measurements, due to limitations of the setup used, the bundles were not illuminated in their full length.

The values obtained pointed out the suitability of these LSCs in real applications, with the advantage of mechanical and environmental protection of the optical active layer incorporated in the hollow-core.

Chapter 6. Scale-up the collection area of LSCs towards metre-length flexible waveguiding photovoltaics

6.1 Introduction

The typical LSC dimensions reported so far (less than 10^{-1} m) impose that *G* values do not change significantly and, then, the comparison of distinct LSC performances is often based on η_{opt} values. The current record value is 28 % (attained with white diffusers) for dye-doped PMMA LSCs [22]. However, for scale-up devices (dimension values of the order of 1-100 m) working in real operating conditions (daylight illumination) and featuring commercial applications, the comparison of the LSC performance should be based on the *F* values.

Whereas for cylindrical LSCs there are no previous reports of *F* values, for planar devices the reported values generally consider the total spectral irradiance on Earth (1000 $W \cdot m^{-2}$) and are always lower than 1 (Table 6.1), although ray-tracing simulations predict *F* values up to 24 [27,268]. The only example with higher values (*e.g.*, *F*=4.4) [37] considers only the spectral absorption region (480-600 nm), Table 6.1. All the *F* values are well below the theoretical thermodynamic limit that predicts *F*~100 for LSC-based on optical active centres with low-Stokes-shift (*e.g.* organic dyes and QDs) [269,270].

Table 6.1 *Figure of merit of F values for distinct LSCs with planar geometry.*

Active layer	***Dimension*** ($\times 10^{-9}$ m^3)	***F***
PMMA/Red305 [28]	(50×50×6)	0.34
PMMA/Oxazine 750/benzene [259]	(15.3×7.5×3)	0.50
PMMA/CdSe/CdS QDs [37]	(215×13×5)	4.4 [a]
Red F/toluene [31]	(75×25×0.5)	0.54 [b]
Rhodamine B/toluene [31]	(75×25×5)	0.42
CdSe/ZnS/toluene [31]	(75×25×5)	0.05
PbS/toluene [31]	(45×12×4)	0.15

[a] *This example considers only the absorbed spectral region (480-600 nm), contrarily to the results reported on refs. [28] and [259].* [b] *The F values are calculated using reported G and* η_{opt} *(total spectral range values).*

Several strategies have been, therefore, proposed to enhance F using additional structures. One approach comprises a resonance-shifting LSC in which the luminescent thin film is separated from the substrate by a low refractive index spacer layer [268]. A second example, reports the use of a TiO_2-doped backside reflector in which the embedded TiO_2 nanoparticles behave as scattering centres and the resulting layer serves as a flexible backside reflector, increasing the probability of light trapping inside the waveguide [260]. Both solutions fail in demonstrating their real capacity to produce large-area LSCs with F>1.

Therefore, processing LSCs with larger surface area is a technological challenge that has been limited by the difficulty in scaling-up its design as it generally involves spin- or dip-coating techniques or the use of moulds to produce homogeneously doped substrates. The coating techniques are advantageous since the luminescence emitted from the film is mostly trapped in the transparent substrate while parasitic losses due to self-absorption and scattering from impurities can be greatly reduced comparing to bulk doped plates, usually prepared using moulds [257].

Featuring improved concentration factors, as mentioned above, the cylindrical geometry has a large potential compared with that of planar [32,219,220,247]. Moreover, the cylindrical geometry allows an easier coupling with optical fibres that could transport light to a remote place for lighting or power production [248,271,272] and renders easier photovoltaics urban integration. As far as we know, only a single example of metre-size cylindrical LSCs (length of 1 m) was reported using QDs-doped acrylic fibres embedded into a PMMA [248,271,272] with a η_{opt} of 0.0263 % [248].

Here, we present a simple approach to scale up the length of fibre waveguiding LSCs (FWLSCs), using a semi-industrial facility designed to draw optical fibres (Figure 6.1). This methodology enables the production of metre-length (up to ~2.5 m) bulk POFs coated with d-U(600) (Figure 2.1A, section 2.1) doped with Rh6G or $Eu(tta)_3{\cdot}2H_2O$ complex (Figure 2.2, section 2.1). Moreover, the same semi-industrial facility is used to fabricated metre-length FWLSCs based on hollow-core fibres, whose core was filled with d-U(600) or t-U(5000) (Figure 2.1B, section 2.1) modified with PTMS and doped with Rh6G or $Eu(tta)_3{\cdot}2H_2O$. As highlighted in the previous chapter, these hollow-core FWLSCs confer mechanical and environmental protection of the optical active layer incorporated in the hollow-core. Light propagation is dependent on the geometry being observed that, in the case of the bulk-coated FWLSCs, propagation is essentially confined to the POF regions and, for the hollow-core FWLSCs, the

hybrid layer also contributes to guide the light. Therefore, the low attenuation values of the POFs in the visible spectral range enables light propagation in the total fibre length (2.5 m) for the bulk coated-LSCs, whereas for the hollow-core based devices light propagation is confined to shorter distances (9-6×10^{-2} m) due to the hybrids intrinsic absorption.

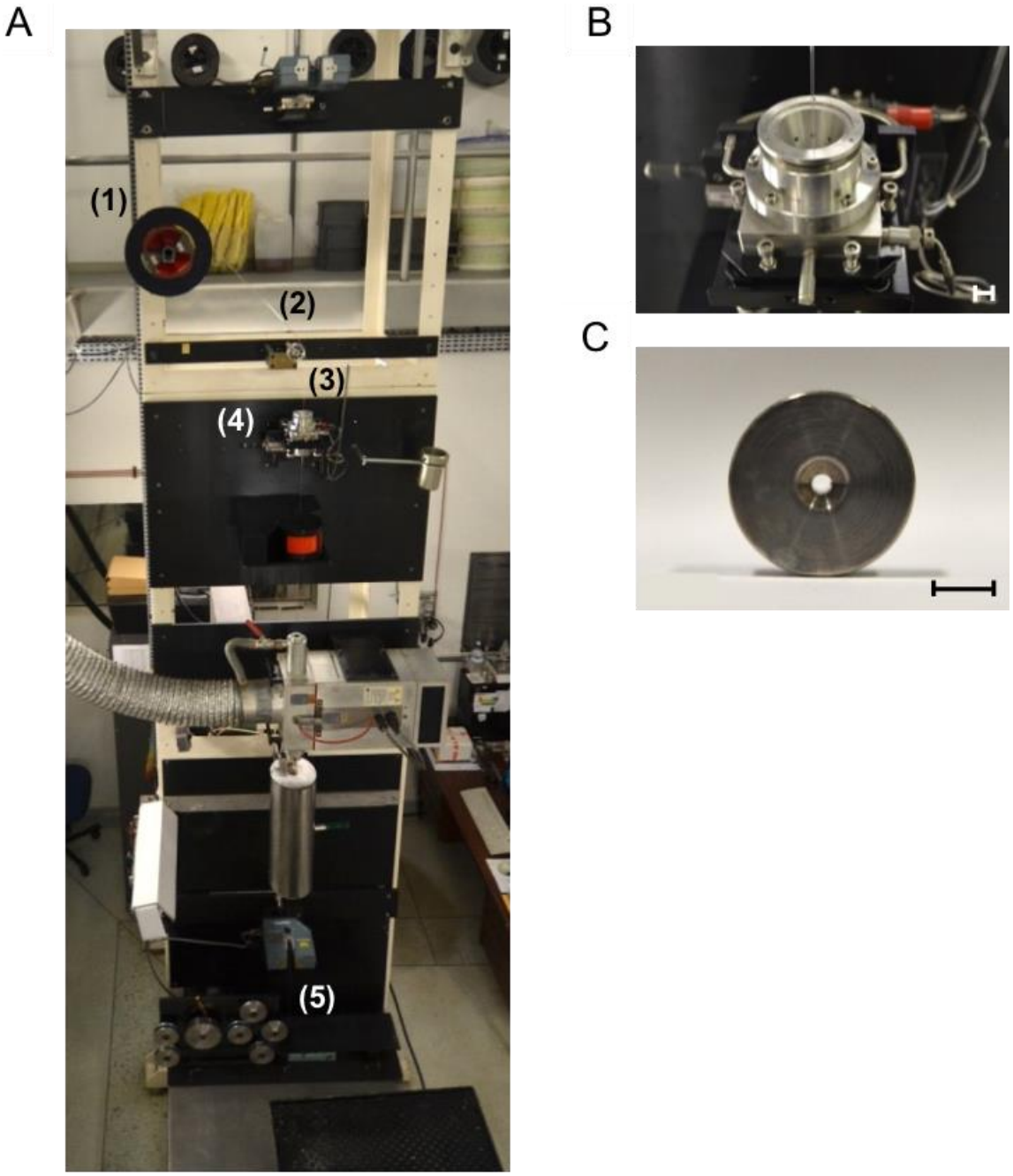

Figure 6.1 *Photographs of the (A) fibre optic manufacturing facility (total height of 8.5 m) and a detailed view of the (B) coating region and of the (C) die are also shown, scale bars 5×10^{-3} m. (1) Fibre spool; (2) bare POF; (3) pinch wheel; (4) coating applicator and (5) pulling tractor assembly.*

6.2 LSC fabrication

6.2.1 Bulk-coated LSCs fabrication

Commercial POFs (HFBR-RUS100Z, Avago Technologies, $1.00\pm0.06\times10^{-3}$ m diameter and ~2.5 m long) with low attenuation values in the visible spectral range were coated with the Eu- or Rh6G-doped d-U(600) layers (Figure 6.2A) using the semi-industrial fibre optic manufacturing facility in Figure 6.1. The setup consists of a spool containing the uncoated fibre, at the upper part of the tower, a pinch wheel, to guide the fibre, and a coating applicator, where the hybrid suspensions are deposited onto the fibre surface. At the lower part, there is the pulling tractor assembly, which drives down the fibre through the system at constant speed.

The doped organic-inorganic hybrid materials synthesis routine is described in section 2.1.

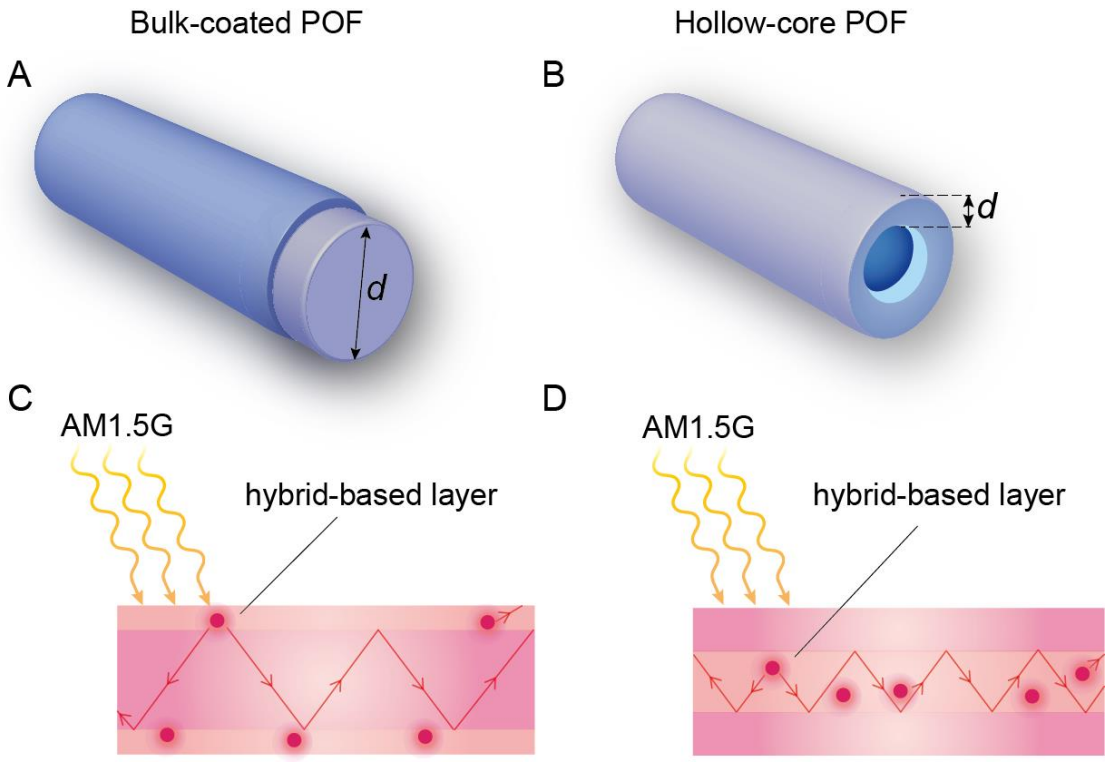

Figure 6.2 *Schematic representation of a LSC made of (A,C) bulk-coated or (B,D) hollow-core POFs with PMMA thickness values of d~10^{-3} m and d~10^{-4} m , respectively. The optical active layer is the Eu^{3+}- or Rh6G-doped d-U(600) or t-U(5000) hybrids coated at the surface of the POFs or embedded into its hollow-core, respectively.*

The pulling tractor assembly drove down the fibre through the system at constant speed of 6 $m{\cdot}s^{-1}$. The hybrids' time to gel was adjusted to ~2 min allowing the pulling of 2.5 m in such

a way that the viscosity of the precursor solution does not change, yielding, therefore, a uniform coating thickness. The thickness of the coating is controlled by the so-called die (Figure 6.1A), which consist of a 4×10^{-3} m thick stainless still disc with a pinhole in the centre. All the devices are aligned to the centre of the pinhole to produce coatings with homogeneous thickness. The pinholes have diameters of 1.6×10^{-3} m and 1.1×10^{-3} m, giving coating thickness values of $\sim95\times10^{-6}$ m and $\sim70\times10^{-6}$ m, respectively (Figure 6.3). All the FWLSCs were kept vertically in the tower until the gelation of the hybrids was completed.

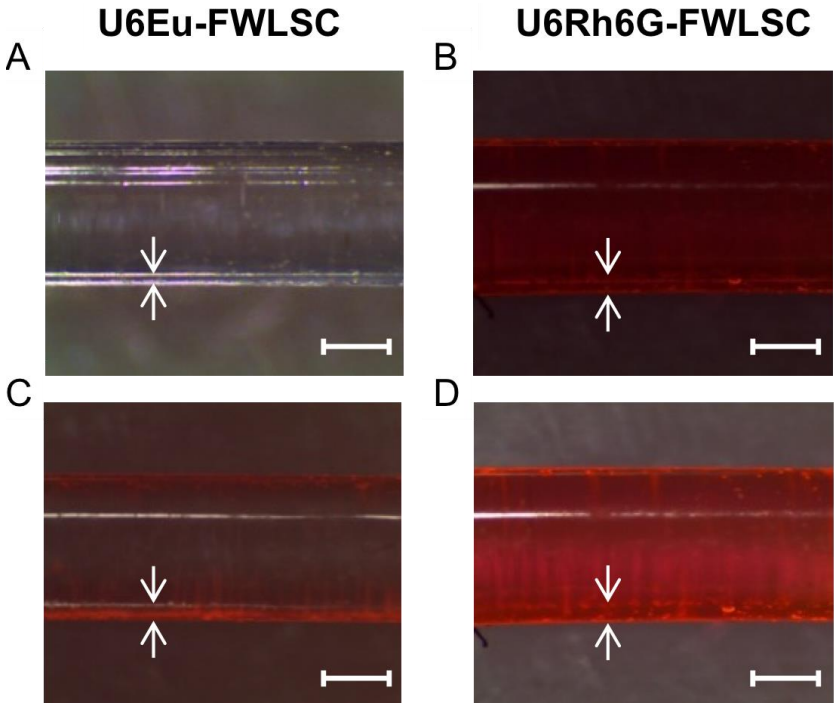

Figure 6.3 *Top view optical microscopy images of some of the bulk-coated FWLSCs under white light illumination (top) and UV irradiation at 365 nm (bottom). The arrows indicate the optically active layer. Scale bars of 5×10^{-4} m.*

6.2.2 Hollow-core LSCs fabrication

PMMA-based hollow-core POFs (Figure 6.2B) were fabricated using the previously mentioned semi-industrial fibre optic manufacturing facility. The drawing speed was controlled to tune the fibre length, namely fibres with length of 2.0 m and 1.5 m were produced at 1.3 $m\cdot min^{-1}$ and 4.1 $m\cdot min^{-1}$, respectively (Table 6.2). The hollow-core was filled with d-U(600) or t-U(5000) hybrids doped with Rh6G or $Eu(tta)_3\cdot2H_2O$, using a vacuum pump (TE-058, Tecnal). The doped organic-inorganic hybrid materials synthesis routine is described in section 2.1. To decrease the viscosity of the hybrids and allow an easier and complete filling of the hollow-core

fibres, the amount of HCl used in the synthesis of the hybrid layers was reduced relatively to that used in the bulk-coated fibres. The hybrid layers based on the d-U(600) and t-U(5000) have an average thickness of ~4.7×10^{-4} and ~8.4×10^{-4} m, respectively (Figure 6.4 and Table 6.2).

The devices will be designated as UYM-FWLSC, where Y=6 or 5 represents the d-U(600) and t-U(5000) hybrids, respectively and M=Eu or Rh6G.

Table 6.2 *Outer d_{out} (m) and inner diameter d_{in}, (m) and length L (m) of the PMMA-preforms and of the hollow-core FWLSCs. The d (m) denotes the PMMA thickness.*

Designation	Preform			Hollow-core fibre			
	d_{out} ($\times10^{-3}$)	d_{in} ($\times10^{-3}$)	L	d_{out} ($\times10^{-3}$)	d ($\times10^{-4}$)	d_{in} ($\times10^{-4}$)	L
U6Eu-FWLSC[a]	15.0	9.0	90.0×10^{-3}	0.95±0.07	2.4±0.2	4.7±0.1	1.5
U6Rh6G-FWLSC[a]							1.5
U5Eu-FWLSC[b]	5.0	3.0	1.5	1.6±0.2	4.2±0.3	8.4±0.6	1.9
U5Rh6G-FWLSC[b]							2.0

The drawing speed was [a]1.3 m·min^{-1} and [b]4.1 m·min^{-1}.

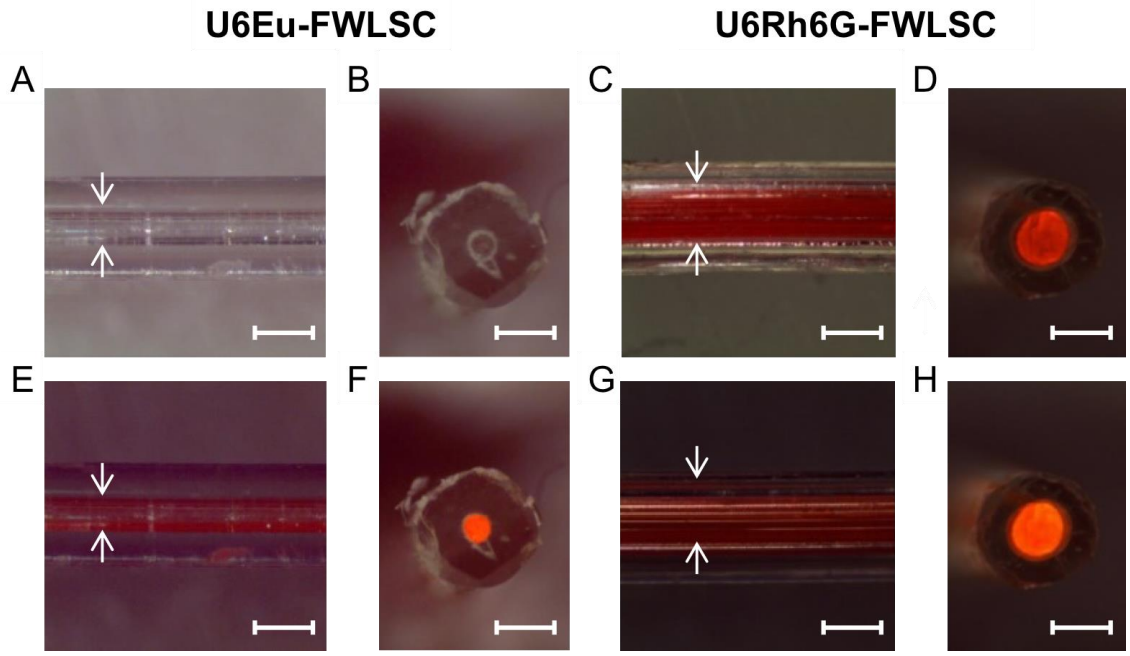

Figure 6.4 *Optical microscopy images of some of the hollow-core FWLSCs under white light illumination (top) and UV irradiation at 365 nm (bottom). The arrows indicate the optically active layer. Scale bars of 5×10^{-4} m.*

6.3 LSCs characterization

The optical characterization (excitation and emission spectra, absorption, refractive index dispersion curves and absolute emission quantum yield) of the doped organic-inorganic hybrids used as active layer in the FWLSCs was performed using the same equipments and conditions described in Appendix A. The optical power at the FWLSCs output was estimated using the same photodiode mentioned in section 5.3, according to Figure A.1A, Appendix A. All I–V measurements were performed under daylight conditions, whose solar irradiance was monitored in real time (Table 6.3).

Table 6.3 *Solar irradiance[a] and weather condition details during the optical characterization of the FWLSCs.*

Device	*Substrate*	*Date*	*Time*	*Irradiance ($W \cdot m^{-2}$)*	*Weather condition*	*Weather station*
U6Rh6G-FWLSC	bulk-coated	26/03/2015	13h:25m	822	sunny	University of Aveiro, Portugal (http://climet ua.fis.ua.pt/)
U6Eu-FWLSC			13h:40m	822		
U6Rh6G-FWLSC	hollow-core	07/04/2015	10h:35m	576	partially cloudy	
U6Eu-FWLSC			10h:50m	580		
U5Rh6G-FWLSC		31/08/2015	17h:20	528	cloudy	
U5Eu-FWLSC			17h30	517		

[a]*The solar irradiance values were monitored in real-time (with a 10 min interval) using data obtained from weather station located in Portugal (Aveiro).*

6.4 Results and discussion

The photographs in Figure 6.5 to Figure 6.7 shows the Rh6G- and Eu-FWLSCs illuminated with UV radiation and natural daylight (Table 6.4). For the bulk-coated and hollow-core FWLSCs the light emitted at the surface (bulk-coated fibres) or emitted in the hollow-core (hollow-filled fibres) is guided through total internal reflection to the edges of the fibres, appearing in a concentrated form at the FWLSCs edges, thus, pointing out that all the fibres can be used as LSCs (Figure 6.5 to Figure 6.7).

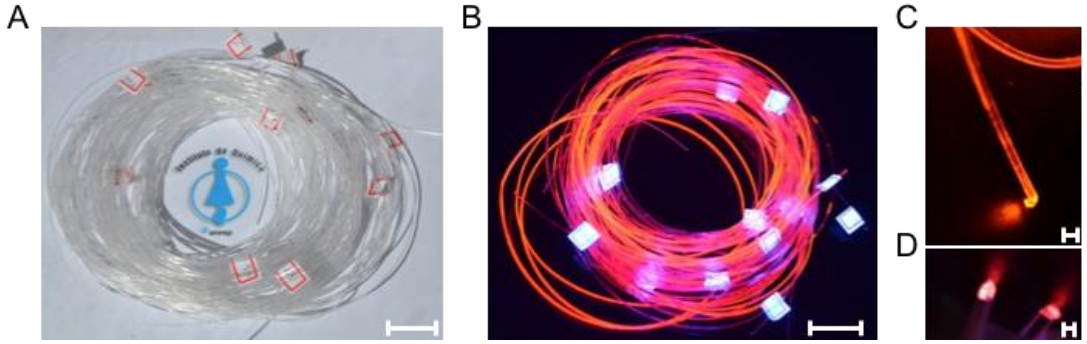

Figure 6.5 *Photographs of the U6Eu-FWLSCs under (A) daylight conditions and (B) UV irradiation, respectively, scale bars of 10^{-2} m. (C,D) Detailed view of the FWLSCs extremities under UV irradiation highlighting the light concentration, scale bars of 10^{-3} m.*

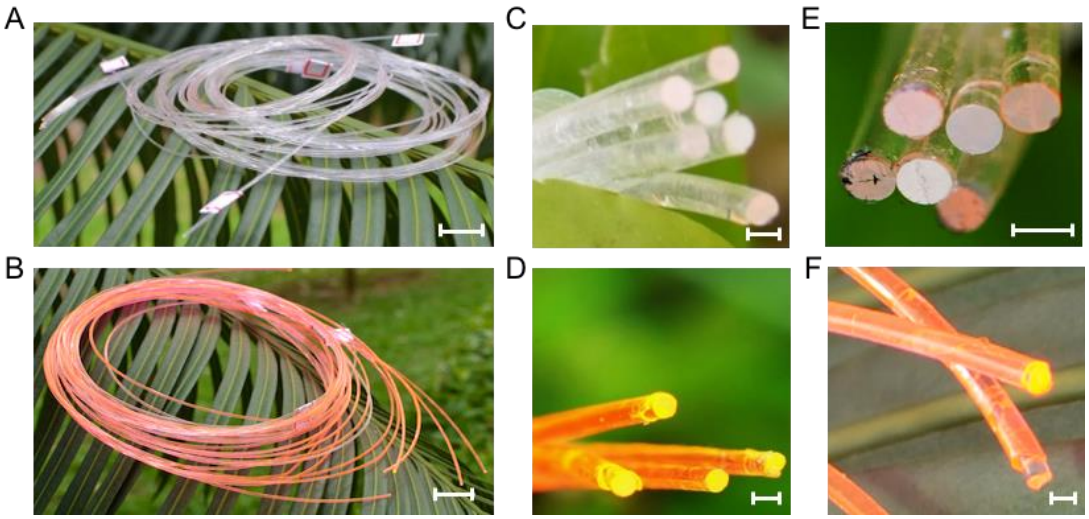

Figure 6.6 *Outdoor photographs of bulk-coated (A) U6Eu-FWLSC and (B) U6Rh6G-FWLSC scale bars of 10^{-2} m. Magnification of the FWLSC extremity for (C, E) U6Eu-FWLSC and (D, F) U6Rh6G-FWLSCs under distinct weather conditions (Table 6.4); scale bars of 10^{-3} m.*

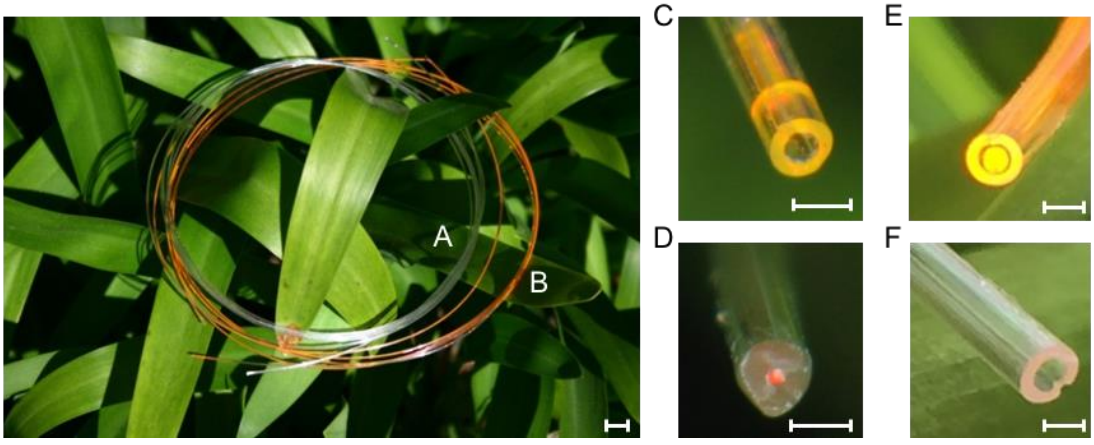

Figure 6.7 *Outdoor photographs of the hollow-core (A) U6Eu-FWLSCs and (B) U6Rh6G-FWLSCs scale bars of 10^{-2} m. Magnification of the FWLSC extremity of (C, E) U5Rh6G-FWLSC and (D, F) U5Eu-FWLSCs under distinct weather conditions (Table 6.4); scale bars of 10^{-3} m.*

Table 6.4 *Solar irradiance[a] and weather condition details during the acquisition of the photos in Figure 6.6 and Figure 6.7.*

Figure	*Date*	*Time*	*Irradiance ($W \cdot m^{-2}$)*	*Weather condition*	*Weather station*
6.6A	25/02/2014	14h:55m	375	partially cloudy	Bauru, Brazil (http://www.ipmet.unesp.br)
6.6B		11h:32m	461		
6.6C		14h:36m	669	sunny	
6.6E		14h:50m	492	partially cloudy	
6.6F		11h:32m	461		
6.6D	28/02/2014	11h:22m	784	sunny	Institute of Chemistry at Araraquara, Brazil
6.7A	14/05/2014	9h:30m	443	partially cloudy	University of Aveiro, Portugal (http://climetua.fis.ua.pt/)
6.7B					
6.7C	17/09/2015	15h:39m	678	sunny	
6.7D		15h:36m			
6.7E		16h:01m	636		
6.7F		16h:02m			

[a] *The solar irradiance values were monitored in real-time (with 10 min interval) using data obtained from weather stations located in Portugal (Aveiro) and in Brazil (Araraquara and Bauru).*

Figure 6.8A shows the emission spectra of the FWLSCs collected at the fibre surface. The emission of the Eu^{3+}-based devices is attributed to the $^5D_0 \rightarrow {}^7F_{0-4}$ transitions and that of Rh6G-FWLSC is ascribed to the dye fluorescence (Figure 6.8A).

The excitation spectra of the hybrid layers were monitored within the emission peak position, namely around 590 nm, U6Rh6G-FWLSCs, and within the $^5D_0 \rightarrow {}^7F_2$ transition, U6Eu-FWLSC (Figure 6.8A). The excitation spectrum of the Eu-FWLSC is formed of a broad band (fwhm ~130nm) in the UV spectral region (300–375 nm) with two main components at ~280 nm and at ~330–370 nm mainly ascribed to the hybrid host and to the tta triplet states [39,45]. The high relative intensity of the tta-related band readily indicates that the ligand-excited states are the main intra-$4f^6$ population path. The excitation spectrum of the Rh6G-FWLSC shows a series of Rh6G-related maxima overlapping the hybrid host excitation region (240–425 nm) and a broad band (450– 550 nm) ascribed to direct excitation of the Rh6G-related states (Figure 6.8B). The absence of the emission bands typically of the undoped d-U(600) host [46] in the

emission spectra of the U6Eu- and U6Rh6G-FWLSCs and of the tta- excited states in the former case [45] points an effective d-U(600)-to-Eu^{3+} energy transfer [47].

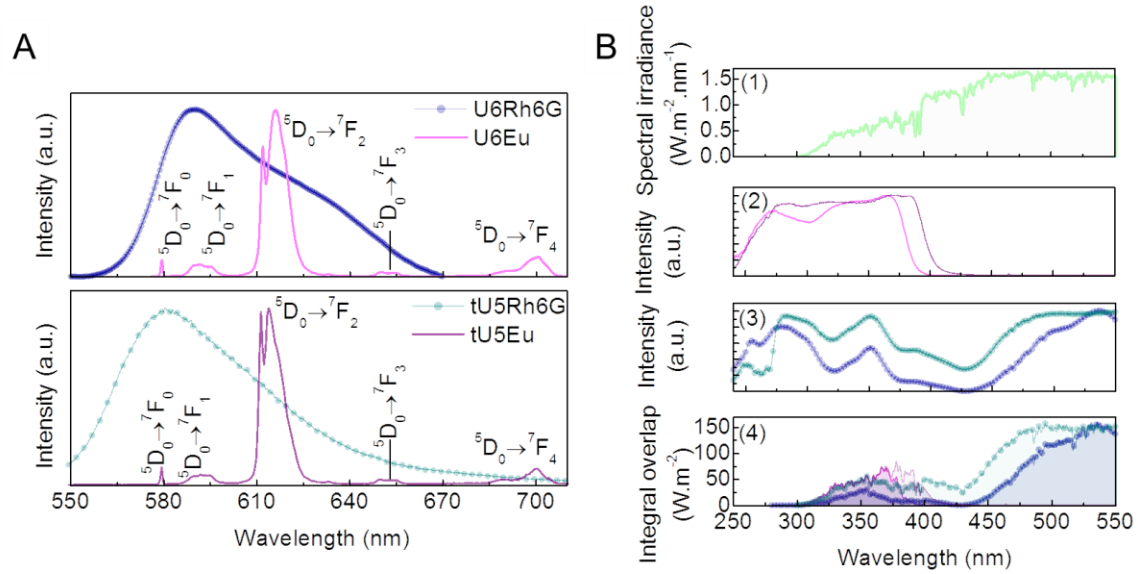

Figure 6.8 *(A) Emission spectra of the bulk-coated U6-FWLSCs (top) and of the U5-FWLSC (bottom) excited at 520 nm (U6Rh6G-FWLSC and U5Rh6G-FWLSC) and at 360 nm (U6Eu-FWLSC and U5Eu- FWLSC), respectively. (B) (1) AM1.5G emission spectrum; excitation spectra monitored at (2) 615 nm for the Eu-FWLSCs and (3) 590 nm for Rh6G-FWLSCs. (4) Overlap integral between the AM1.5 emission spectrum and the excitation spectra of the Rh6G- FWLSCs (blue) and Eu-FWLSCs (purple).*

The ability of the optical active layers to harvest the sunlight on Earth is inferred through the estimation of the overlap integral given by Eq. (3.8), section 3.3. The larger values for the overlap integral (Figure 6.8B) are found for the Rh6G-based hybrids, compared with that found for the Eu^{3+}-based ones, as listed in Table 6.5. Independently of the optical active centres, the LSCs based on the t-U(5000) host have larger values due to the presence of the chromophore PTMS. Thus, the t-U(5000)-based Rh6G- and Eu-FWLSCs have the potential to convert, respectively, 84 % and 16 % of the sunlight intensity available for DS conversion (~262 $W \cdot m^{-2}$) [2,3,13,73].

The ability of the optical active layer to convert the harvested sunlight is quantified by the measurement of the η_{yield}, listed in Table 6.5, being the maximum values for U5Rh6G- and U5Eu-FWLSCs.

Here, light propagation will be discussed as function of the two geometries here presented (bulk-coated and hollow-core, Figure 6.2), using the same geometrical optics model used in section 5.4 and mentioned in section 3.2, that takes into account the refractive index contrast, $\Delta n_{i,j}=n_i-n_j$ with $i,j=1,2,3$, (Figure 6.9) between the (1) air, (2) hybrid layer and (3) PMMA [239].

As mentioned in the previous chapter, two main mechanisms will contribute to the optical losses. In particular, losses will occur at the surface through a so-called escape cone (pink cone in Figure 6.9) and through absorption within the propagation layers.

Table 6.5 *Overlap integral (O, $W \cdot m^{-2}$) and η_{yield} of Eu-FWLSCs and Rh6G-FWLSCs.*

Designation	***O***	η_{yield}
U6Eu-FWLSC	31	0.30±0.03 (270-400 nm)
U6Rh6G-FWLSC	115	0.78±0.08 (350; 536 nm)
U5Eu-FWLSC	43	0.85±0.09 (360 nm)
U5Rh6G-FWLSC	221	0.93±0.09 (550 nm)

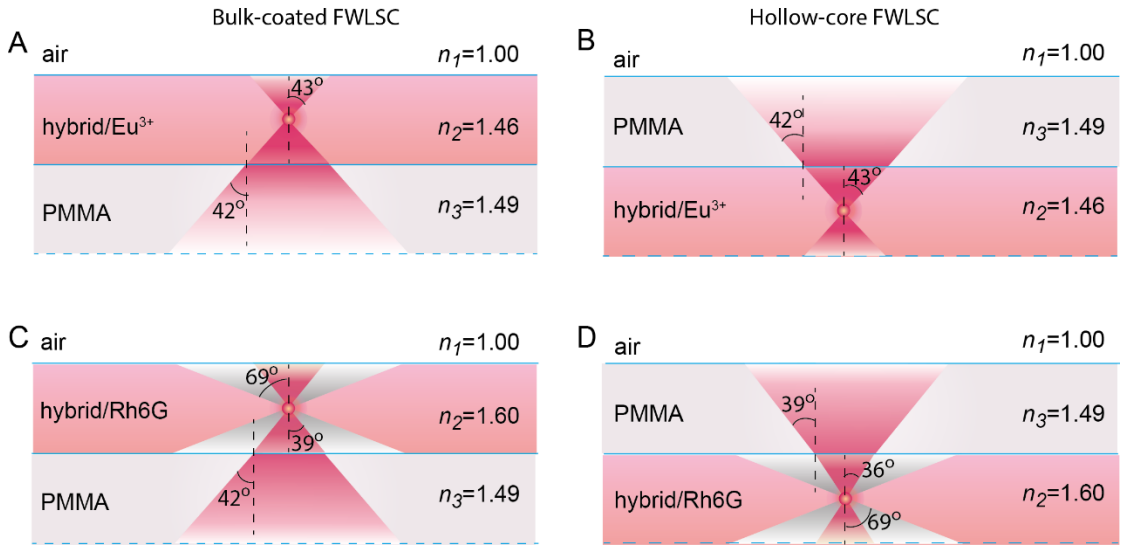

Figure 6.9 *Schematic representation of the cross-section of the (A,C) bulk-coated and (B,D) hollow-core FWLSCs with the escape cones and light trapped in the POF and hybrid (pink) and only in the hybrid (grey). The critical angles θ_c are also indicated.*

The refractive index dispersion curves for the hybrids and of the POFs are presented in Figure 6.10A. For all the Eu^{3+}-based FWLSCs (Figure 6.9A,B), $\Delta n_{2,3}$ is very small as the refractive index values of the hybrid and PMMA are very close, yielding η_{trap} ~73 %, independently of the geometry. The remaining light (27 %) will be lost through the escape cone. For all the Rh6G-based FWLSCs (Figure 6.9C,D), $\Delta n_{2,3}$ is larger (~0.1), thus, trapping will occur within the external interface with air and also in the film-substrate interface, yielding η_{trap} ~80 %. The light confinement will occur in the hybrid and PMMA layers and only in the hybrid layer for photons emitted within $69° < \theta_c \leq 90°$ (pink cone). In general, a decrease of η_{trap} may occur

if the device temperature is elevated above room-temperature, due to the thermal optical coefficients of POF and of the hybrid layer. As highlighted in section 5.4, the thermal optical coefficient of POF and of the hybrid are similar ($\sim -10^{-4}$ °C^{-1}) [273], so that a small decrease of 0.2 % per 10 °C in η_{trap} may be expected. We should note that, comparing the refractive index contrast for Rh6G-LSC optically active layer here reported with the one previously reported in section 5.4, here we found values ~5 % higher. This may be due to differences in the condensation process during the sol-gel reactions.

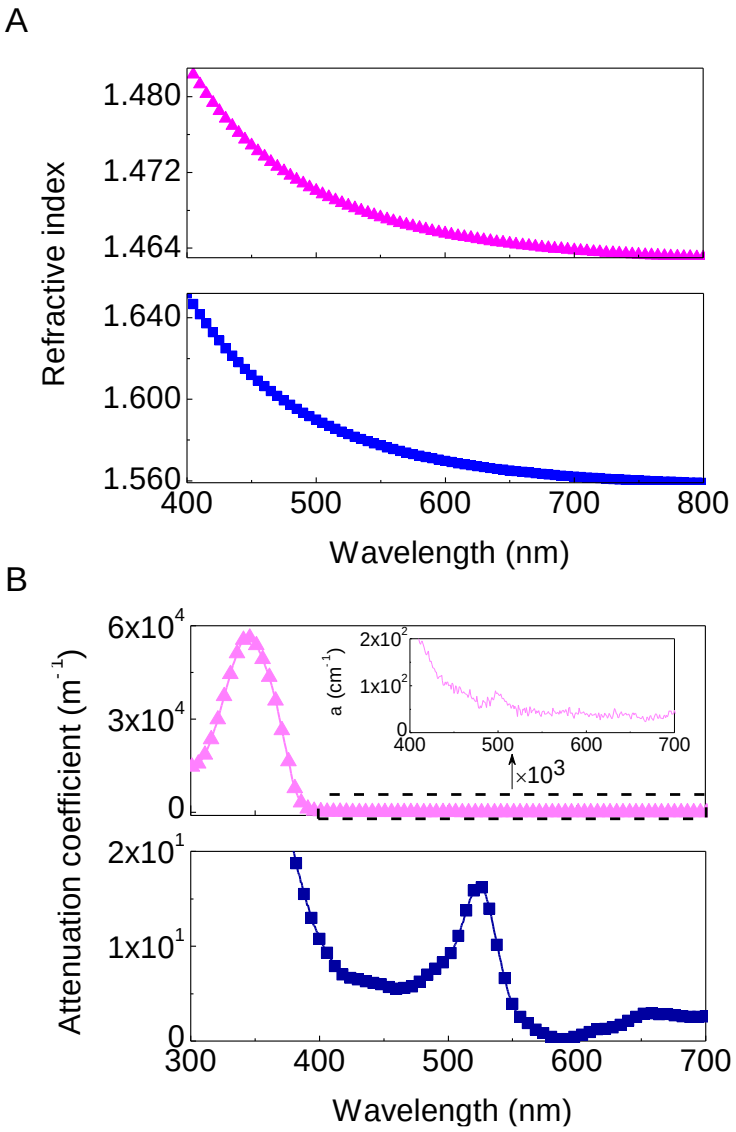

Figure 6.10 *(A) Refractive index dispersion curves and (B) absorption spectra of Eu-FWLSCs (top) and Rh6G-FWLSCs (bottom). The inset shows the magnification in the 400–700 nm spectral region for Eu-FWLSCs.*

Despite a small increase (~6 %) of the η_{trap} value found for the hollow-core FWLSCs compared with that of the bulk-coated devices, we note that the absorption losses are more significant in the hollow-core geometry. This is due to the higher thickness of the hybrid layer in the hollow-core FWLSC ($4.7\text{-}8.4\times10^{-4}$ m) compared with that in the bulk-coated ones ($\sim70\text{-}95\times10^{-6}$ m) that increases the probability of absorption of the emitted photons with higher order modes (photons emitted with an angle closer to θ_c). Moreover, the effective diameter (d in Figure 6.2 and Table 6.2) of the hollow-core fibre is smaller ($\sim10^{-4}$ m) than that of the bulk-coated fibres ($\sim10^{-3}$ m), thus, the optical path for the emitted photons in the PMMA layer is favoured for the bulk-coated geometry. Furthermore, the higher hybrid thickness also contributes for an additional attenuation of the evanescent electromagnetic field of the optical signal propagated thought the PMMA. In summary, for bulk-coated fibres LSCs light propagation occurs essentially at the PMMA layer, whereas for the hollow-core based devices the light is also guided within the hybrid layer. In agreement with the methodology adopted in section 5.4, the discussion of the light propagation must also take into account the absorption spectra of the hybrid and PMMA layers.

The PMMA α_{at} values were calculated by weighting the PMMA absorption spectrum (Figure 5.6B, section 5.4) by the emission of the hybrids' layer yielding to 0.107 m^{-1} and 0.095 m^{-1} for the Eu-FWLSC and Rh6G-FWLSC, respectively, regardless of the hybrid host. Such low α_{at} values indicate that light propagation may occur in the total length (2.5 m) of the bulk-coated FWLSC.

In the case of the hollow-core FWLSC, as the hybrid layer contributes larger for the light guidance (Figure 6.9), additional losses are predicted as the absorption coefficient of the hybrid material is larger than that of PMMA (Figure 6.10B). Thus, light will travel a shorter length compared with that found in the bulk-coated FWLSCs. Similarly to what is reported in section 5.4 of the previous chapter, such length was experimentally quantified by a "piano" test [49], using 5 cm-wide pieces of black paper. In this case, due to the longer length of the FWLSCs comparing to the ones described in the previous chapter, the data are well described by a single exponential function given by:

$$P_{out}=P_0 e^{-aL} \tag{6.1}$$

where P_0 is the maximum power value (Figure 6.11). The α_{at} values found were ~10.8 m^{-1}, 14.9 m^{-1}, 8.8 m^{-1} and 17.6 m^{-1} for U6Eu-FWLSC, U6Rh6G-FWLSC, U5Eu-FWLSC and U5Rh6G-FWLSC, respectively. The fibre L_c values were estimated by replacing the α_{at} values into Eq. (5.2), section 5.4. For U6Eu-FWLSC, U6Rh6G-FWLSC, U5Eu-FWLSC and U5Rh6G-FWLSC, L_c is ~8.2×10^{-2} m, ~6.4×10^{-2} m, ~9.4×10^{-2} m and ~5.5×10^{-2} m, respectively, that are of the same order of the ones reported in section 5.4, for the hollow-core triangular LSCs.

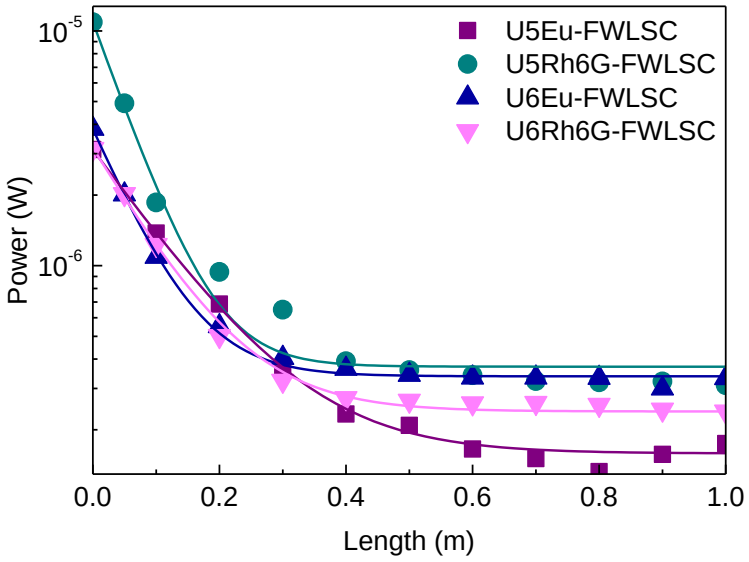

Figure 6.11 *Output power as function of the distance measured in the "piano" test [49]. R^2>0.997 for all the fittings.*

The overall performance of the FWLSCs is quantified by the calculation of η_{opt} under natural daylight illumination (Table 6.3) through Eq. (3.10), section 3.3. We should keep in mind that the dependence of travelling distance on the geometry, is weighted through the geometrical gain, *G*, by considering in the calculus of A_s the traveling distance (2.5 m for all the bulk coated and the corresponding L_c values for each hollow-core FWLSC) and A_e as the area of the two extremities, as it is expected the same light concentration at each FWLSC end. The measure is based on the ratio (P_e) between the electrical power delivered by photodiode directly exposed to AM1.5G radiation and the electrical power delivered by the photodiode coupled to the FWLSC (Table 6.6). Considering the total incident spectral range, the maximum η_{opt}=8.0 % was measured for the U5Rh6G-FWLSC. This is the larger value known for single layer LSC devices without external devices (*e.g.* mirrors and white diffusers) to boost light trapping. In particular,

the η_{opt} value is larger than that recently reported for LSCs based on CdSe and CdS QDs in PMMA (~1 %) [37] and $CuInSe_2$/ZnS QDs in poly(lauryl methacrylate) (~3.3 %) [34]. When considering the absorbing region, the larger η_{opt} values are found for the U5Eu-FWLSC (~72.4 %), as the Eu^{3+}-doped layer is essentially transparent in the visible, when compared with that found for the Rh6G-doped ones (Figure 5.6A, section 5.4).

Table 6.6 *Electrical power ratio (P_e), optical conversion efficiency (η_{opt}, %) and concentration factor (F) values of Eu-FWLSCs and Rh6G-FWLSCs.*

Device	Geometry	P_e	η_{opt}	F
U6Eu-FWLSC	bulk-coated	0.24	0.01 0.6 [a]	0.1 6.5 [a]
U6Rh6G-FWLSC		0.52	0.08 0.5 [a]	0.4 2.3 [a]
U6Eu-FWLSC	hollow-core	0.03	0.2 5.2 [a]	0.05 1.4 [a]
U5Eu-FWLSC		0.13	2.3 72.4 [a]	0.4 12.3 [a]
U6Rh6G-FWLSC		0.32	1.6 6.4 [a]	0.4 1.6 [a]
U5Rh6G-FWLSC		0.29	8.0 32.6 [a]	0.9 3.7 [a]

[a] *Values calculated considering the absorbed spectral region 300-380 nm (Eu-FWLSC) and 300-540 nm (Rh6G-FWLSC).*

The values for the concentration factor *F* are also listed in Table 6.6. We compare the performance of the Rh6G- and Eu-FWLSCs with that of planar LSCs, as there are no previous reports for cylindrical ones. In fact, the calculated *F* values are among the highest reported so far being approximately twice than the maximum values reported for LSCs based on PMMA/Oxazine 750/benzene [259] and Red F/toluene [31] (*F*~0.5) in the case of U5Rh6G-FWLSC (*F*~0.9). We note that the *F* value found for the U5Eu-FWLSC (12.3) is approximately three times higher than the current world-record measured considering only the LSC absorbing region, *F*=4.4 (Table 6.1) [37]. Whereas for the planar LSCs listed in Table 6.1 the improvement in the *F* factor is strongly prevented by the difficulties in scaling-up the planar geometry, in the case of the coated Eu-FWLSCs, *F* can be enhanced one order of magnitude by simply increasing the fibre length until a critical value (~10 m).

6.5 Conclusions

We have demonstrated a new approach for the fabrication of long-length fibre FWLSCs with different geometries, by obtaining large area LSCs based on bulk-coated and hollow-core POFs with unprecedented concentration factors (up to 12.3), compared with those known for planar LSCs, and with the further advantages of being lighter-weight, flexible and cost-effective. The hollow-core FWLSCs presents a higher trapping efficiency and a better protection of the optical active layer from handling damage and direct exposure to adverse weather (relatively to the bulk-coated FWLSCs) making them ideal for exterior applications, such as wearable power source for personal electronic devices [274]. For the bulk-coated FWLSCs, longer devices (up to 10 m) can be easily fabricated with much better performance, with F values one order of magnitude higher than those listed in Table 6.1 and Table 6.6, illustrating the impact of the approach here discussed on the development of innovative lightweight and mechanically flexible high-performance waveguiding photovoltaics.

Chapter 7. General conclusions and perspectives

The synergy between the intrinsic characteristics of sol-gel derived organic–inorganic hybrids and the easiness to incorporate luminescent species and process them as thin films or monoliths affords hybrid materials real potential for applications in LSCs.

In this work, organic-inorganic hybrids were used to incorporate Eu^{3+} ions and organic dyes, such as Rhodamine 6G and Rhodamine 800, for application in LSCs. Although a short-length (10^{-2} m) planar LSC was fabricated, most of the work done was based on short (centimetre) and long (metre) scale cylindrical LSCs, due to its increased *G* factor, that would, consequently, increase the overall concentration factor, *F*.

The first fabricated cylindrical LSCs, with lengths of the order of 10^{-2} m, whose optically active layer was based in a d-U(600) hybrid doped with an Eu^{3+} complex and used as a coating of the POF, showed η_{opt} values of ~26 % and *PCE*~3 %, considering the number of absorbed photons, which made promising the use of commercial POFs in LSCs.

Therefore, accordingly to the previous results, POFs were used to produce hollow-core LSCs, also with length ~10^{-2} m. In this case, three types of optically active layers were used to fill the hollow-core of the POFs: t-U(5000) organic-inorganic hybrid doped with an Eu^{3+} complex, with Rhodamine 6G or with Rhodamine 800 organic dyes. The LSCs were quantified in terms of $\eta_{opt,}$ with a maximum of 3.4 % for the Rhodamine 6G-based LSC, considering the total incident photons. The use of Rhodamine 800 in LSCs was of great interest due to its NIR emission, which is the spectral range of c-Si PV cells maximum response. In this case, the obtained η_{opt} value was of the same order of the NIR-emitting LSCs reported in the literature. The particularity of these LSCs lies on the fact that the outer geometry of the POFs used is triangular, allowing an easier coupling between the POFs. Thus, a fibre bundle structure was formed for the LSCs with each type of optically active layer and, then, coupled to a c-Si PV cell, to evaluate its performance by measuring the *EQE*. The results showed an overall *EQE* increase of up to 20 %, for the Rh6G-LSCs based bundle, with the most evident gain in the UV spectral region, which is the range where c-Si PV cell present lower performance. The correspondent

absolute *EQE* increase in the 300-400 nm range was ~50 %, higher than the 40 % value reported for a down-shifting layer based on Lumogen 300 organic dye dispersed in PMMA on a Si PV cell [263]. A light guidance analysis was performed for the LSCs according to the optically active layer, since the differences in the refractive index would lead to different optical propagation paths. For instance, for Eu-based LSC, light guidance occurred mostly in the POF (refractive index of the active layer lower than that of the POF), while for the Rhodamine 6G-based LSC, light propagation occurs both in POF and in the active layer (refractive index of the POF is lower than that of the active layer). Due to the fact that the thickness of the hybrid layer is the same order as the POF's, the probability of absorption of the emitted photons by active layer itself is increased, and thus the effective length of the produced LSCs is ~3×10^{-2} m.

The usage of low attenuation POFs in the LSCs showed the possibility of fabricating long-length cylindrical LSCs, at the metre scale. With the goal of increasing the exposed area to improve the concentration ability of the LSC and increase the concentration factor *F*, both bulk-coated and hollow-core LSCs were fabricated with lengths of up to ~2 m. Also in these cases, the light propagation was an addressed issue, to investigate the differences of light propagation paths in function of the geometry, bulk-coated or hollow-core, and of the optically active layer being based on Eu^{3+}- or Rhodamine 6G-doped t-U(5000). Although the bulk-coated LSCs analysis showed that, in this configuration, LSCs with length of up to ~10 m could be attained, for hollow-core LSCs, light guidance is limited to ~10^{-2} m, for the reason mentioned above for the triangular hollow-core LSCs. Nevertheless, the maximum η_{opt}=72.4 % and a *F* factor of 12.3 were obtained for the Eu^{3+}-doped t-U(5000)-based LSC, considering the number of absorbed photons

The LSCs field is, however, in its infancy and much remains to be investigated before prototypes become a commercial reality. Here are some of the research themes deserving particular attention:

a) Dye alignment. An attractive strategy that emerged very recently and represents an extraordinarily promising path to performance enhancement of dye-doped LSCs is dye alignment. This exciting concept, first introduced by Verbunt *et al.* [45], led to several interesting technological advances, such as the development of LSCs in which the dye molecules are either perpendicularly aligned to the plane of the substrate [275] or in a linear fashion in the plane of the substrate [45,276]. Anisotropic LSCs exhibit a series of benefits with regard to isotropic LSCs. In conventional dye-doped LSCs, randomly oriented luminescent molecules embedded

in a transparent substrate (or waveguide) absorb diffuse light incident on the substrate and collectively re-emit these photons isotropically at a lower energy. Approximately ~75 % of the re-emitted photons are trapped in the substrate through total internal reflection (considering a refractive index ~1.5). A fraction of the absorbed photons is lost from the substrate if they are re-emitted above the critical angle through the face of the LSC, or scattered outside of the substrate. In anisotropic LSCs, η_{trap} may be improved by increasing the fraction of re-emitted photons that are trapped in the substrate through the control of the orientation of the dye molecules [45].

Mulder *et al.* [275] reported an increase of the η_{trap} value from 66 % for randomly oriented LSCs, relying on a hybrid system composed of isotropic Coumarin 6 (1 % solid weight content) and host PMMA, to 81 % for a vertically-aligned LSC employing the rod shaped dye molecule Coumarin 6 (1 % solid weight content) and a homeotropic polymerizable liquid crystal mixture including a polymerizable nematic liquid crystal, homeotropic dopant molecules, and a photo-initiator. Orienting the molecules perpendicularly to the substrate weakens the absorption of the perpendicular incident radiation. To correct this, an external holographic diffuser was successfully used above the LSC to scatter the incident light (Figure 7.1A). These authors demonstrated that the enhancement of η_{trap} was preserved for G up to 30. We note that an increase of G without compromising η_{trap} is a key factor to reduce the cost of solar electricity.

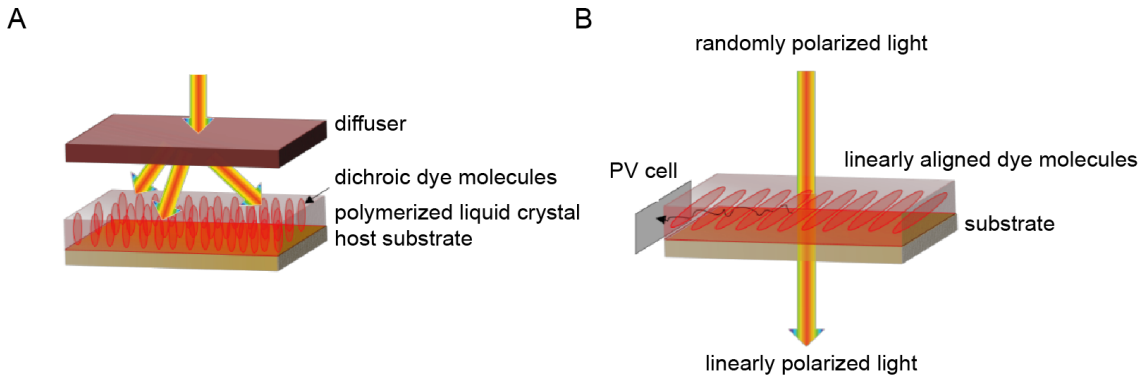

Figure 7.1 *Schematic representation of a (A) vertically-aligned LSC [275] and a (B) horizontally-aligned LSC [276]. Taken from refs. [275] and [276].*

Linearly Polarized LSCs (LPLSCs), in which the dye molecules are aligned in-plane with the substrate, represent another challenging approach, since they are expected to replace classical linear polarizers for light harvesting applications (e.g., portable devices with flat panel displays). The absorption of LPLSCs is linearly polarized, meaning that light is absorbed very

strongly for polarizations parallel to the dipole moment of the dye molecules, but, in contrast, perpendicularly polarized light is transmitted, leaving the substrate. As a consequence, LPLSCs resemble ordinary polarizers. However, instead of dissipating the absorbed photons as heat, a LPLSC funnels the captured photons to photocell elements placed at the edges of the substrate (Figure 7.1B). Mulder *et al.* [276] aligned Coumarin 6 linearly in the plane of a glass substrate using the same polymerizable liquid crystal host used in the vertically-aligned LSC described above. To improve the harvesting of indoor radiation across the visible spectrum, a horizontally-aligned LSC hosting two dye molecules cascading in energy (Coumarin 6 and 4-dicyanomethyl-6-dimethylaminostiryl-4H-pyran) was also created. Up to 38% of the photons polarized on the long axis of the dye molecules could be coupled to the edge of the device with an order parameter of 0.52.

b) Surface losses. The major issue associated with current LSCs has to do with the low efficiency they present that still doesn't make them cost-competitive with electric energy obtained from fossil fuels, since an efficiency value of 30 % would be needed to make LSCs a commercially viable solution [31]. Great part of total losses is due to the escape cone of the matrix (radiation that escape through the surface of the matrix instead of being internally reflected) and re-absorption of the emitted photons by the luminescent entities themselves, caused by overlap of absorption and emission spectra. It is then imperative to search for new optically active centres and LSC configurations to reduce losses and, consequently, increase the efficiency of these devices. Periodic surface patterning of the photoluminescent emitting layer may be envisaged in order to reduce the light escape though the surface [277]. The patterning of the organic-inorganic hybrid host is easily achieved incorporating photo responsive species, e.g. Zr(IV) *n*-propoxide chelated with methacrylic acid, at the LSC surface [250,278-280].

c) Geometry. The LSC geometry is crucial for further improvements on the conversion efficiency. Besides the use of the cylindrical geometry which allows an increase of the concentration factor (compared with planar structures), yielding more efficient LSCs [32,219,247], as demonstrated in this thesis, a luminescent concentrator PV system that embeds large scale, interconnected arrays of microscale Si PV cells (μ-cells) in thin matrix layers doped with luminophores was proposed as an alternative to conventional LSC planar geometry [281]. The dimensions and designs of the μ-cells allow the capture of light not only through their top surfaces, but also through their sidewalls and bottom surfaces increasing further their power output by more than 300 % [281]. This unusual LSC design offers improved performance

compared with conventional layouts, and a variety of engineering options with particular value in ultrathin, lightweight and bendable systems.

d) Building integration. The LSCs development can also be seen as an attractive way of dropping the solar energy costs, as they can assist the urban integration of PV components into buildings [282,283], for example as photovoltaic windows that would transform energy-passive building façades into large-area energy generation units [66], solar harvesting urban furniture, allowing electronic devices charging [284] or, even, as wearable solar harvesting fabrics, such as backpacks, for mobile energy [285]. With LSCs, the PV structure becomes part of the building itself such as, for instance, as windows, balancing contributions towards natural lighting, as well as creating electrically active elements and increasing the visual impact of the building [239,286,287]. The multi-coloured glass panels that adorn the exterior of MUSAC, the contemporary art museum of Castilla and León, in Léon, Spain, and the Congress Palace, in Montreal, Canada, are good examples that illustrate the huge potential of this idea (Figure 7.2), although in these cases their functionality is simply aesthetic.

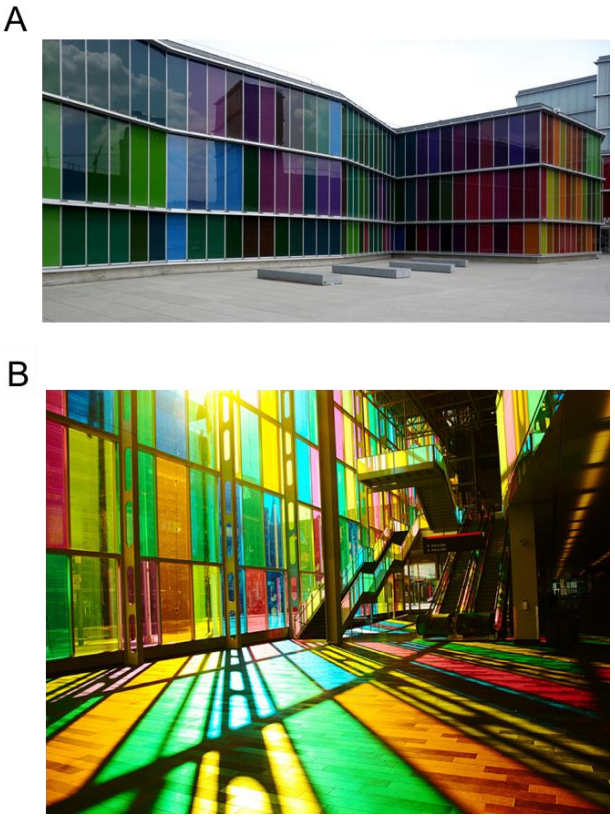

Figure 7.2 *Photograph of the (A) MUSAC museum in Léon, Spain (taken by Olga Cuesta, courtesy of MUSAC, http://www.musac.es) and of the (B) Congress Palace in Montreal, Canada.*

e) DC hybrid materials. DC Ln^{3+}-containing hybrid materials have not yet been successfully demonstrated, despite the potential addition of up to 7 absolute % to the conversion yield [3].

f) DC and UC processes working together. This is a subject clearly unexplored. An interesting example involving a hybrid nanostructure formed by Gd_2O_3:Yb(2 %)/Er(0.3 %) NPs coated with the $Eu(dbm)_3$phen complex was reported by Singh *et al.* [214]. The nanocomposite displays green and red UC, upon excitation at 976 nm, together with a red DS, when excited at 355 nm (ligands levels) or 521 nm ($^2H_{11/2}$ intra f^{11} level). Although the anticipated beneficial effects of combining DC and UC processes (in a single layer or in a multilayer structure) should be demonstrated, once coupled to PV devices this type of materials might be able to improve the conversion yields of Si-based (dye-sensitized) PV cells by as much as 5-8 absolute % and of dye-sensitized cells by 5.5-6.5 absolute % [3].

A short note about the potential supply disruption of lanthanides, or more generally rare earth elements. These elements are crucial in the transition to a green economy, due to their essential role in a large variety of technologies (permanent magnets, lamp phosphors, catalysts, rechargeable batteries and photonics) and are, therefore, in high demand [288,289]. The low concentration in which they are present in the Earth's crust makes economic exploitation difficult and consequently the potential risk of a supply disruption is a present concern [290,291]. Although that risk analysis lies completely outside the scope of this thesis, the relatively small amount of these elements that are used for LSCs (the emissive organic and organic-inorganic hybrid layers contain typically an amount of Ln^{3+} ions less than 10-15 %, in weight) makes that potential shortage not so problematic, relatively to what can be anticipated in other research areas.

Future research should be directed to the production of hollow-core LSCs, because they provide additional protection of the active layer, with enlarged L_c in order to increase the exposed area and, consequently, the concentration factor. In this work, the maximum L_c values was of the order of 10^{-2}, mostly due to the reduced refractive index contrast between the active layer and the PMMA of the POF, which induce that light propagation occur also in active layer, instead of in the PMMA exclusively. Thus, future work should be done towards increasing the refractive index contrast between the active layer and the waveguide, for instance, by using different types of polymer for the POF waveguide with increased refractive index. This would

be a step forward to make LSCs market competitive and helping the necessary turnover of the world energy consumption scenario.

Appendix A. Experimental techniques

A.1 Elemental analysis

Elemental analysis for C, H and N were performed with a CHNS-932 elemental analyser with standard combustion conditions and handling of the samples at air.

A.2 Fourier transform spectroscopy: infrared spectroscopy (FT-IR)

The spectra were collected over the range 4000-400 cm^{-1} by averaging 64 scans at a maximum resolution of 4 cm^{-1} using a MATTSON 7000 FTIR Spectrometer. The compounds were finely ground (about 2 mg), mixed with approximately 175 mg of dried KBr (Merck, spectroscopic grade), and pressed into pellets. Consecutive spectra were recorded until reproducible results were obtained.

A.3 Fourier transform spectroscopy: attenuated total reflectance (FT-ATR)

The FT-ATR spectra were recorded using a MATTSON 7000 FTIR spectrometer equipped with a Specac Golden Gate Mk II ATR accessory having a diamond top-plate and KRS-5 focusing lenses. The spectra were collected over the range 4000-250 cm^{-1} by averaging 128 scans at a maximum resolution of 4 cm^{-1}.

A.4 Photoluminescence

Emission and excitation spectra were recorded at 300 K using a modular double grating excitation spectrofluorimeter with an emission monochromator (Fluorolog-3 2-Triax, Horiba Scientific) coupled to a photomultiplier (R928 Hamamatsu), using the front face acquisition mode. The excitation source was a 450 W xenon arc lamp. The emission spectra were corrected for detection and optical spectral response of the spectrofluorimeter and the excitation spectra were weighed for the spectral distribution of the lamp intensity using a photodiode reference detector.

A.5 Emission quantum yield

The absolute emission quantum yields were measured at room temperature using a system (C9920-02, Hamamatsu) with a 150 W xenon lamp coupled to a monochromator for wavelength discrimination, an integrating sphere as the sample chamber, and a multichannel analyser for signal detection. The method is accurate to within 10%.

A.6 Absorption spectroscopy

Absorption spectra in the UV/vis range were performed with a spectrometer (Lambda 950, Perkin Elmer) with a 150 mm diameter Spectralon integrating sphere, using a scan rate of 150 $nm \cdot min^{-1}$ and a resolution of 1 nm.

A.7 Spectroscopic ellipsometry

The dispersion curves of the POFs and of the hybrid layers were experimentally determined through spectroscopic ellipsometry using an AutoSE ellipsometer (HORIBA Scientific). The measurements were made with a total of 250 points in the wavelength range 450-850 nm, an incidence angle of 70 °, a signal quality of 30 and a measurement spot area of 250×250 μm^2.

A.8 LSCs optical power

The optical power at the cylindrical LSCs output was estimated using a commercial photodiode (IF D91, Industrial Fiber Optics, Inc.), with a wall plug efficiency to the AM1.5G solar spectrum distribution of 4 % coupled to the LSCs, according to the coupling scheme in Figure A.1A.

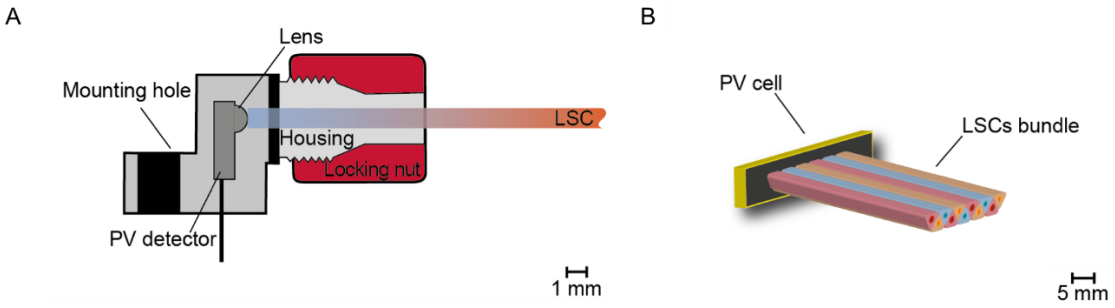

Figure A.1 *Diagram of (A) the photodiode coupling to the LSC and (B) the PV cell coupling to the LSCs bundle. The scale refers to the device dimensions.*

A.9 External quantum efficiency (*EQE*) measurements

When working with the bundle, the *EQE* was estimated using a monocrystalline silicon PV cell (KXOB22-12X1L, IXYS), according to the coupling scheme in Figure A.1B. I_{sc} measurements according to excitation wavelength were performed (to estimate *EQE* values) using a 150 W xenon lamp as the light source coupled to a monochromator (Triax 180, Horiba Scientific), controlled by a LabVIEW routine. The I_{sc} values of the PV cell were measured using a semiconductor device analyser (B1500A, Keysight Technologies). The power of the incident beam (P_{in}) was measured with an integrating sphere (ISP 150L, Instrument Systems) connected to a detector (MAS40-121, Instrument Systems).

A.10 Optical microscopy

Optical microscopy images in Chapters 3 and 6 were obtained with a stereomicroscope (EZ40 HD, Leica). The hybrid layer thickness was estimated in 5 distinct points of the LSCs surface. Optical microscopy images in Chapter 5 were obtained by an Olympus BX51 brightfield microscope (10× objective), in the reflection mode, equipped with a hyperspectral imaging system (CytoViva Inc., Auburn, AL). The system integrates an optical imaging CCD camera (QImaging Retiga 4000R), a visible-NIR hyperspectral camera (Cytoviva®), a motorized stage and a halogen light source (Fiber-lite®, DC-950). The light scattered from the sample in the 400 to 1000 nm spectral region was captured by the hyperspectral camera at each line for each pixel in the sample combining motion of the microscope stage. The hyperspectral scanning is vertical and each image results from 696 lines with each pixel field-of-view on the hyperspectral images corresponding to 1.3×1.3 μm^2 on the sample plane. All the hyperspectral data were acquired and analysed using ENVI 4.8 software.

Appendix B. List of publications

1. **S.F.H. Correia**, P.P. Lima, E. Pecoraro, S.J.L. Ribeiro, P.S. André, R.A.S. Ferreira and L.D. Carlos, Scale up the collection area of luminescent solar concentrators towards meter-length flexible waveguiding photovoltaics, *Progress in Photovoltaics: Research and Applications*, 24, 1178, 2016.

2. **S.F.H. Correia**, P.P. Lima, P.S. André, R.A.S. Ferreira and L.D. Carlos, High-efficiency luminescent solar concentrators for flexible waveguiding photovoltaics, *Solar Energy Materials* & *Solar Cells*, 138, 51, 2015.

3. **S.F.H. Correia**, P.P. Lima, V. De Zea Bermudez, S.J.L. Ribeiro, P.S. André, R.A.S. Ferreira and L.D. Carlos. Luminescent solar concentrators: challenges for lanthanide-based organic–inorganic hybrid materials*, Journal of Materials Chemistry A*, 2, 5580, 2014.

4. **S.F.H. Correia**, P.P. Lima, L.D. Carlos, R.A.S. Ferreira and P.S. André, Luminescent solar concentrators based on plastic optical fibres, OECC/ACOFT 2014, 6-10 July, Melbourne, Australia.

5. R. Rondão, A.R. Frias, **S.F.H. Correia**, L. Fu, V. de Zea Bermudez, P.S. André, R.A.S. Ferreira and L.D. Carlos, High performance near infrared luminescent solar concentrators, *submitted to ACS Applied Materials* & *Interfaces*

6. **S.F.H. Correia**, A.R. Frias, L. Fu, R. Rondão, E. Pecoraro, S.J.L. Ribeiro, F.C. Polachini, P.S. André, R.A.S. Ferreira and L.D. Carlos, Bundle structure of hollow-core triangular luminescent solar concentrators based on visible and NIR emitting tripodal organic-inorganic hybrids, *to be submitted.*

References

[1] S. C. W. Krauter, *Solar Electric Power Generation - Photovoltaic Energy Systems*, **2006**, Springer Berlin Heidelberg, New York.

[2] X. Huang, S. Han, W. Huang, X. Liu, *Chem. Soc. Rev.,* **2013**, 42, 173.

[3] J.-C. G. Bünzli, A.-S. Chauvin, *Lanthanides in Solar Energy Conversion* in *Handbook on the Physics and Chemistry of Rare-Earths*, J.-C.G. Bünzli and V.K. Pecharsky (Eds.), Elsevier B. V., Amsterdam, **2014**, pp. 169-282.

[4] E. W. McFarland, *Energ. Environ. Sci.,* **2014**, 7, 846.

[5] *NREL - National Renewable Energy Laboratory,* Accessed 28th October 2016, Available from: http://www.nrel.gov/pv/assets/images/efficiency_chart.jpg.

[6] M. A. Green, K. Emery, Y. Hishikawa, W. Warta, E. D. Dunlop, *Prog. Photovolt: Res. Appl.,* **2016**, 24, 3.

[7] R. Harikisun, H. Desilvestro, *Sol. Energy,* **2011**, 85, 1179.

[8] J. Seo, J. H. Noh, S. I. Seok, *Accounts Chem. Res.,* **2016**, 49, 562.

[9] G. Hodes, *Science,* **2013**, 342, 317.

[10] C. B. Cornell, *Perovskite Solar Cell: Key To A Brighter Solar Future?,* The Huffington Post, Accessed 28th September 2016, Available from: http://www.huffingtonpost.com/clayton-b-cornell/perovskite-solar-cell-key_b_11069628.html.

[11] *PolyU Develops Perovskite-Silicon Tandem Solar Cells with the World's Highest Power Conversion Efficiency,* Accessed 28th September 2016, Available from: https://www.polyu.edu.hk/web/en/media/media_releases/index_id_6208.html.

[12] W. Shockley, H. J. Queisser, *J. Appl. Phys.,* **1961**, 32, 510.

[13] B. S. Richards, *Sol. Energ. Mat. Sol. C.,* **2006**, 90, 2329.

[14] J. Grandidier, D. M. Callahan, J. N. Munday, H. A. Atwater, *IEEE J. Photovolt.,* **2012**, 2, 123.

[15] F. Dimroth, *Phys. Status Solidi C,* **2006**, 3, 373.

[16] M. J. Currie, J. K. Mapel, T. D. Heidel, S. Goffri, M. A. Baldo, *Science,* **2008**, 321, 226.

[17] G. Maggioni, A. Campagnaro, S. Carturan, A. Quaranta, *Sol. Energ. Mat. Sol. C.,* **2013**, 108, 27.

[18] W. H. Weber, J. Lambe, *Appl. Optics,* **1976**, 15, 2299.

[19] C. Tummeltshammer, A. Taylor, A. J. Kenyon, I. Papakonstantinou, *Opt. Lett.,* **2016**, 41, 713.

[20] W. Zhou, M. C. Wang, X. J. Zhao, *Sol. Energy,* **2015**, 120, 419.

[21] Y. Zhang, S. Sun, R. Kang, J. Zhang, N. N. Zhang, W. H. Yan, W. Xie, J. J. Ding, J. Bao, C. Gao, *Energ. Convers. Manage.,* **2015**, 95, 187.

[22] C. H. Wang, R. Winston, W. Y. Zhang, L. Jiang, D. Pelka, S. Carter, *AIP. Conf. Proc,* **2011**, 1407, 163.

[23] A. F. Mansour, *Polym. Test.,* **1998**, 17, 153.

[24] C. Liu, B. Li, *J. Optics,* **2015**, 17, 025901.

[25] A. Kaniyoor, B. McKenna, S. Comby, R. C. Evans, *Adv. Opt. Mater.,* **2015**, 4, 444.

[26] S. F. Daorta, A. Proto, R. Fusco, L. C. Andreani, M. Liscidini, *Appl. Phys. Lett.,* **2014**, 104, 153901.

[27] E. H. Banaei, A. F. Abouraddy, *Proc. SPIE,* **2013**, 8821, 882102-1.

[28] P. T. M. Albers, C. W. M. Bastiaansen, M. G. Debije, *Sol. Energy,* **2013**, 95, 216.

[29] Y. M. Zhao, G. A. Meek, B. G. Levine, R. R. Lunt, *Adv. Opt. Mater.,* **2014**, 2, 606.

[30] S. M. El-Bashir, F. M. Barakat, M. S. AlSalhi, *Renew. Energ.,* **2014**, 63, 642.

[31] V. Sholin, J. D. Olson, S. A. Carter, *J. Appl. Phys.,* **2007**, 101, 123114.

[32] R. H. Inman, G. V. Shcherbatyuk, D. Medvedko, A. Gopinathan, S. Ghosh, *Opt. Express,* **2011**, 19, 24308.

[33] F. Purcell-Milton, Y. K. Gun'ko, *J. Mater. Chem.,* **2012**, 22, 16687.

[34] F. Meinardi, H. McDaniel, F. Carulli, A. Colombo, K. A. Velizhanin, N. S. Makarov, R. Simonutti, V. I. Klimov, S. Brovellii, *Nat. Nanotechnol.,* **2015**, 10, 878.

[35] L. R. Bradshaw, K. E. Knowles, S. McDowall, D. R. Gamelin, *Nano Lett.,* **2015**, 15, 1315.

[36] K. E. Knowles, T. B. Kilburn, D. G. Alzate, S. McDowall, D. R. Gamelin, *Chem. Commun.,* **2015**, 51, 9129.

[37] F. Meinardi, A. Colombo, K. A. Velizhanin, R. Simonutti, M. Lorenzon, L. Beverina, R. Viswanatha, V. I. Klimov, S. Brovelli, *Nat. Photonics,* **2014**, 8, 392.

[38] I. Coropceanu, M. G. Bawendi, *Nano. Lett.,* **2014**, 14, 4097.

[39] C. S. Erickson, L. R. Bradshaw, S. McDowall, J. D. Gilbertson, D. R. Gamelin, D. L. Patrick, *ACS Nano,* **2014**, 8, 3461.

[40] Z. Krumer, S. J. Pera, R. J. A. van Dijk-Moes, Y. M. Zhao, A. F. P. de Brouwer, E. Groeneveld, W. G. J. H. M. van Sark, R. E. I. Schropp, C. D. Donega, *Sol. Energ. Mat. Sol. C.,* **2013**, 111, 57.

[41] U. Aeberhard, R. Vaxenburg, E. Lifshitz, S. Tomic, *Phys. Chem. Chem. Phys.,* **2012**, 14, 16223.

[42] J. Bomm, A. Büchtemann, A. J. Chatten, R. Bose, D. J. Farrell, N. L. A. Chan, Y. Xiao, L. H. Slooff, T. Meyer, A. Meyer, W. G. J. H. M. van Sark, R. Koole, *Sol. Energ. Mat. Sol. C.,* **2011**, 95, 2087.

[43] G. V. Shcherbatyuk, R. H. Inman, C. Wang, R. Winston, S. Ghosh, *Appl. Phys. Lett.,* **2010**, 96, 191901.

[44] M. G. Hyldahl, S. T. Bailey, B. P. Wittmershaus, *Sol. Energy,* **2009**, 83, 566.

[45] P. P. C. Verbunt, A. Kaiser, K. Hermans, C. W. M. Bastiaansen, D. J. Broer, M. G. Debije, *Adv. Funct. Mater.,* **2009**, 19, 2714.

[46] M. Kennedy, S. J. McCormack, J. Doran, B. Norton, *Sol. Energy,* **2009**, 83, 978.

[47] W. G. J. H. M. van Sark, K. W. J. Barnham, L. H. Slooff, A. J. Chatten, A. Büchtemann, A. Meyer, S. J. McCormack, R. Koole, D. J. Farrell, R. Bose, E. E. Bende, A. R. Burgers, T. Budel, J. Quilitz, M. Kennedy, T. Meyer, C. D. M. Donegá, A. Meijerink, D. Vanmaekelbergh, *Opt. Express,* **2008**, 16, 21773.

[48] Y. Zhou, D. Benetti, Z. Fan, H. Zhao, D. Ma, A. O. Govorov, A. Vomiero, F. Rosei, *Adv. Energy Mater. ,* **2016**, 6, 1501913.

[49] W. Wu, T. Wang, X. Wang, S. Wu, Y. Luo, X. Tian, Q. Zhang, *Sol. Energy,* **2010**, 84, 2140.

[50] T. X. Wang, J. Zhang, W. Ma, Y. H. Luo, L. J. Wang, Z. J. Hu, W. X. Wu, X. Wang, G. Zou, Q. J. Zhang, *Sol. Energy,* **2011**, 85, 2571.

[51] D. K. Boer, D. J. Broer, M. G. Debije, W. Keur, A. Meijerink, C. R. Ronda, P. P. C. Verbunt, *Opt. Express,* **2012**, 20, A395.

[52] M. M. Nolasco, P. M. Vaz, V. T. Freitas, P. P. Lima, P. S. André, R. A. S. Ferreira, P. D. Vaz, P. Ribeiro-Claro, L. D. Carlos, *J. Mater. Chem. A,* **2013**, 1, 7339.

[53] J. Graffion, A. M. Cojocariu, X. Cattoën, R. A. S. Ferreira, V. R. Fernandes, P. S. André, L. D. Carlos, M. Wong Chi Man, J. R. Bartlett, *J. Mater. Chem.,* **2012**, 22, 13279.

[54] J. Graffion, X. Cattoën, M. Wong Chi Man, V. R. Fernandes, P. S. André, R. A. S. Ferreira, L. D. Carlos, *Chem. Mater.,* **2011**, 23, 4773.

[55] V. T. Freitas, L. S. Fu, A. M. Cojocariu, X. Cattoen, J. R. Bartlett, R. Le Parc, J. L. Bantignies, M. W. C. Man, P. S. Andre, R. A. S. Ferreira, L. D. Carlos, *ACS Appl. Mater. Inter.,* **2015**, 7, 8770.

[56] M. Tonezzer, G. Maggioni, A. Campagnaro, S. Carturan, A. Quaranta, M. della Pirriera, D. G. Tauste, *Prog. Photovol.: Res. Appl.,* **2015**, 23, 1037.

[57] C. Liu, R. J. Deng, Y. L. Gong, C. Zou, Y. Liu, X. Zhou, B. J. Li, *Int. J. Photoenergy,* **2014**, 2014, 290952.

[58] A. Sanguineti, A. Monguzzi, G. Vaccaro, F. Meinardi, E. Ronchi, M. Moret, U. Cosentino, G. Moro, R. Simonutti, M. Mauri, R. Tubino, L. Beverina, *Phys. Chem. Chem. Phys.,* **2012**, 14, 6452.

[59] I. S. Grigoryev, L. G. Klapshina, S. A. Lermontova, V. V. Semenov, V. M. Treushnikov, V. V. Treushnikov, B. A. Bushuk, S. Clement, W. E. Douglas, *Nanotechnologies in Russia,* **2012**, 7, 492.

[60] X. Wang, T. Wang, X. Tian, L. Wang, W. Wu, Y. Luo, Q. Zhang, *Sol. Energy,* **2011**, 85, 2179.

[61] J. Graffion, X. Cattoen, M. W. C. Man, V. R. Fernandes, P. S. Andre, R. A. S. Ferreira, L. D. Carlos, *Chem. Mater.,* **2011**, 23, 4773.

[62] B. Jezowskatrzebiatowska, E. Lukowiak, W. Strek, A. Buczkowski, S. Patela, J. Radojewski, J. Sarzynski, *Sol. Energ. Mater.,* **1986**, 13, 267.

[63] Y. M. Zhao, R. R. Lunt, *Adv. Energy Mater.,* **2013**, 3, 1143.

[64] H. Hernandez-Noyola, D. H. Potterveld, R. J. Holt, S. B. Darling, *Energ. Environ. Sci.,* **2012**, 5, 5798.

[65] W. G. J. H. M. van Sark, *Renew. Energ.,* **2013**, 49, 207.

[66] M. G. Debije, P. P. C. Verbunt, *Adv. Energ. Mater.,* **2012**, 2, 12.

[67] L. D. Carlos, R. A. S. Ferreira, V. de Zea Bermudez, S. J. L. Ribeiro, *Adv. Mater.,* **2009**, 21, 509.

[68] A. Goetzberger, W. Greubel, *Appl. Phys.,* **1977**, 14, 123.

[69] R. Reisfeld, S. Neuman, *Nature,* **1978**, 274, 144.

[70] R. Reisfeld, Y. Kalisky, *Nature,* **1980**, 283, 281.

[71] R. Reisfeld, C. K. Jorgensen, *Struct. Bond.,* **1982**, 49, 1.

[72] R. Reisfeld, *Mater. Sci. Eng.,* **1985**, 71, 375.

[73] B. C. Rowan, L. R. Wilson, B. S. Richards, *IEEE J. Sel. Top. Quant.,* **2008**, 14, 1312.

[74] R. Reisfeld, *Opt. Mater.,* **2010**, 32, 850.

[75] N. M. Jose, L. A. S. D. Prado, *Quim. Nova,* **2005**, 28, 281.

[76] C. Sanchez, P. Belleville, M. Popall, L. Nicole, *Chem. Soc. Rev.,* **2011**, 40, 696.

[77] C. J. Brinker, G. W. Scherrer, *Sol-Gel Science: The Physics and Chemistry of Sol-Gel Processing,* **1990**, Academic Press, San Diego, California.

[78] C. Sanchez, B. Julian, P. Belleville, M. Popall, *J. Mater. Chem.,* **2005**, 15, 3559.

[79] L. H. Slooff, E. E. Bende, A. R. Burgers, T. Budel, M. Pravettoni, R. P. Kenny, E. D. Dunlop, A. Büchtemann, *Phys. Status Sol. - R.,* **2008**, 2, 257.

[80] A. F. Mansour, H. M. A. Killa, S. Abd El-Wanees, M. Y. El-Sayed, *Polym. Test.,* **2005**, 24, 519.

[81] I. Meazzini, N. Willis-Fox, C. Blayo, J. Arlt, S. Clement, R. C. Evans, *J. Mater. Chem. C,* **2016**, 4, 4049.

[82] R. Reisfeld, D. Shamrakov, C. Jorgensen, *Sol. Energ. Mat. Sol. C,* **1994**, 33, 417.

[83] M. Buffa, S. Carturan, M. G. Debije, A. Quaranta, G. Maggioni, *Sol. Energ. Mat. Sol. C.,* **2012**, 103, 114.

[84] S. J. Gallagher, B. Norton, P. C. Eames, *Sol. Energy,* **2007**, 81, 813.

[85] V. Misra, H. Mishra, *J. Chem. Phys.,* **2008**, 128, 244701.

[86] K. Machida, H. Li, D. Ueda, S. Inoue, G. Adachi, *J. Lumin,* **2000**, 87-9, 1257.

[87] C. Li, W. Chen, D. Wu, D. H. Quan, Z. M. Zhou, J. J. Hao, J. Qin, Y. W. Li, Z. B. He, K. Wang, *Sci. Rep.-UK,* **2015**, 5, 1.

[88] H. C. Lin, P. Xie, Y. Liu, X. Zhou, B. J. Li, *Nanotechnology,* **2015**, 26, 335401.

[89] M. G. Debije, P. P. C. Verbunt, B. C. Rowan, B. S. Richards, T. L. Hoeks, *Appl. Optics,* **2008**, 47, 6763.

[90] J. C. Goldschmidt, M. Peters, M. Hermle, S. W. Glunz, *J. Appl. Phys.,* **2009**, 105, 114911.

[91] K. Bhaumik, J. D. Hurst, P. J. Nadkarni, N. Sankaran, S. Velate, US2010043880, **2010**.

[92] U. Resch-Genger, M. Grabolle, S. Cavaliere-Jaricot, R. Nitschke, T. Nann, *Nat. Methods,* **2008**, 5, 763.

[93] J. A. Levitt, W. H. Weber, *Appl. Optics,* **1977**, 16, 2684.

[94] J. S. Batchelder, A. H. Zewail, T. Cole, *Appl. Optics,* **1981**, 20, 3733.

[95] A. M. Hermann, *Sol. Energy,* **1982**, 29, 323.

[96] M. A. El-Shahawy, A. F. Mansour, *J. Mater. Sci.-Mater. El.,* **1996**, 7, 171.

[97] B. A. Swartz, T. Cole, A. H. Zewail, *Opt. Lett.,* **1977**, 1, 73.

[98] J. M. Drake, M. L. Lesiecki, J. Sansregret, W. R. L. Thomas, *Appl. Optics,* **1982**, 21, 2945.

[99] I. Baumberg, O. Berezin, A. Drabkin, B. Gorelik, L. Kogan, M. Voskobojnik, M. Zaidman, *Polym. Degrad. Stab.,* **2001**, 73, 403.

[100] R. Kinderman, L. H. Slooff, A. R. Burgers, N. J. Bakker, A. Buchtemann, R. Danz, J. A. M. van Roosmalen, *J. Sol. Energ.-T. Asme,* **2007**, 129, 277.

[101] M. G. Debije, P. P. C. Verbunt, P. J. Nadkarni, S. Velate, K. Bhaumik, S. Nedumbamana, B. C. Rowan, B. S. Richards, T. L. Hoeks, *Appl. Optics,* **2011**, 50, 163.

[102] R. Reisfeld, M. Eyal, V. Chernyak, R. Zusman, *Sol. Energ. Mater.,* **1988**, 17, 439.

[103] L. R. Wilson, B. S. Richards, *Appl. Optics,* **2009**, 48, 212.

[104] G. Seybold, G. Wagenblast, *Dyes Pigments,* **1989**, 11, 303.

[105] A. F. Mansour, M. G. El-Shaarawy, S. M. El-Bashir, M. K. El-Mansy, M. Hammam, *Polym. Int.,* **2002**, 51, 393.

[106] F. Castiglione, G. Lanzani, A. Mele, A. Monguzzi, M. Passarello, A. Ruggirello, F. Scotognella, V. T. Liveri, *J. Mater. Sci.,* **2011**, 46, 6402.

[107] G. Griffini, M. Levi, S. Turri, *Sol. Energ. Mat. Sol. C,* **2013**, 118, 36.

[108] A. Sanguineti, M. Sassi, R. Turrisi, R. Ruffo, G. Vaccaro, F. Meinardi, L. Beverina, *Chem. Commun.,* **2013**, 49, 1618.

[109] D. B. Murphy, M. W. Davidson, *Fundamentals of Light Microscopy and Electronic Imaging*, **2013**, John Wiley & Sons, Inc.

[110] P. Reiss, M. Protiere, L. Li, *Small,* **2009**, 5, 154.

[111] Isnaeni, K. H. Kim, D. L. Nguyen, H. Lim, T. N. Pham, Y. H. Cho, *Appl. Phys. Lett.,* **2011**, 98, 012109.

[112] U. Banin, M. Bruchez, A. P. Alivisatos, T. Ha, S. Weiss, D. S. Chemla, *J. Chem. Phys.,* **1999**, 110, 1195.

[113] W. G. J. H. M. van Sark, P. L. T. M. Frederix, A. a. Bol, H. C. Gerritsen, A. Meijerink, *ChemPhysChem,* **2002**, 3, 871.

[114] M. Nirmal, B. O. Dabbousi, M. G. Bawendi, J. J. Macklin, J. K. Trautman, T. D. Harris, L. E. Brus, *Nature,* **1996**, 383, 802.

[115] M. Kuno, D. P. Fromm, H. F. Hamann, A. Gallagher, D. J. Nesbitt, *J. Chem. Phys.,* **2000**, 112, 3117.

[116] L. M. Shao, J. Q. Zhao, Z. G. Xia, X. P. Jing, *J. Electrochem. Soc.,* **2011**, 158, J300.

[117] G. Zucchi, V. Murugesan, D. Tondelier, D. Aldakov, T. Jeon, F. Yang, P. Thuery, M. Ephritikhine, B. Geffroy, *Inorg. Chem.,* **2011**, 50, 4851.

[118] O. Moudam, B. C. Rowan, M. Alamiry, P. Richardson, B. S. Richards, A. C. Jones, N. Robertson, *Chem. Commun.,* **2009**, 6649.

[119] O. L. Malta, H. F. Brito, J. F. S. Menezes, F. R. G. Silva, C. de Mello Donegá, S. Alves Junior, *Chem. Phys. Lett.,* **1998**, 282, 233.

[120] P. P. Lima, M. M. Nolasco, F. A. A. Paz, R. A. S. Ferreira, R. L. Longo, O. L. Malta, L. D. Carlos, *Chem. Mater.,* **2013**, 25, 586.

[121] D. W. Dong, S. C. Jiang, Y. F. Men, X. L. Ji, B. Z. Jiang, *Adv. Mater.,* **2000**, 12, 646.

[122] Y. H. Li, H. J. Zhang, S. B. Wang, Q. G. Meng, H. R. Li, X. H. Chuai, *Thin Solid Films,* **2001**, 385, 205.

[123] H. R. Li, L. S. Fu, J. Lin, H. J. Zhang, *Thin Solid Films,* **2002**, 416, 197.

[124] P. Lenaerts, A. Storms, J. Mullens, J. D'Haen, C. Gorller-Walrand, K. Binnemans, K. Driesen, *Chem. Mater.,* **2005**, 17, 5194.

[125] Y. L. Sui, B. Yan, *J. Photoch. Photobio. A,* **2006**, 182, 1.

[126] E. O. Oh, Y. H. Kim, C. M. Whang, *J. Electroceram.,* **2006**, 17, 335.

[127] D. Zhao, S. J. Seo, B. S. Bae, *Adv. Mater.,* **2007**, 19, 3473.

[128] E. Pecoraro, R. A. Sá Ferreira, C. Molina, S. J. L. Ribeiro, Y. Messsaddeq, L. D. Carlos, *J. Alloy. Compd.,* **2008**, 451, 136.

[129] B. Yan, Y. L. Sui, J. L. Liu, *J. Alloy Compd.,* **2009**, 476, 826.

[130] Y. Wang, H. R. Li, Y. Feng, H. J. Zhang, G. Calzaferri, T. Z. Ren, *Angew. Chem., Int. Ed.,* **2010**, 49, 1434.

[131] Z. E. Chamas, X. M. Guo, J. L. Canet, A. Gautier, D. Boyer, R. Mahiou, *Dalton Trans.,* **2010**, 39, 7091.

[132] H. S. He, M. Dubey, A. G. Sykes, P. S. May, *Dalton Trans.,* **2010**, 39, 6466.

[133] L. Armelao, G. Bottaro, S. Quici, C. Scalera, M. Cavazzini, G. Accorsi, M. Bolognesi, *Chemphyschem,* **2010**, 11, 2499.

[134] P. P. Lima, R. A. S. Ferreira, R. O. Freire, F. A. A. Paz, L. S. Fu, S. Alves, L. D. Carlos, O. L. Malta, *ChemPhysChem,* **2006**, 7, 735.

[135] P. P. Lima, F. A. A. Paz, R. A. S. Ferreira, V. de Zea Bermudez, L. D. Carlos, *Chem. Mater.,* **2009**, 21, 5099.

[136] S. Chandra, S. McCormack, J. Doran, M. Kennedy, A. Chatten, *New Concepts for Luminescent Solar Concentrators*, in 25th European Photovoltaic Solar Energy Conference and Exhibition, **2010**, Valencia, Spain.

[137] S. M. El-Bashir, F. M. Barakat, M. S. AlSalhi, *J. Lumin.,* **2013**, 143, 43.

[138] R. Reisfeld, T. Saraidarov, G. Panzer, V. Levchenko, M. Gaft, *Opt. Mater.,* **2011**, 34, 351.

[139] M. Fukushima, H. Yanagi, S. Hayashi, N. Suganuma, Y. Taniguchi, *Thin Solid Films,* **2003**, 438, 39.

[140] V. Levchenko, M. Grouchko, S. Magdassi, T. Saraidarov, R. Reisfeld, *Opt. Mater.,* **2011**, 34, 360.

[141] M. Iosin, P. Baldeck, S. Astilean, *Nucl. Instrum. Meth. B,* **2009**, 267, 403.

[142] J. Zhu, K. Zhu, L. Q. Huang, *Phys. Lett. A,* **2008**, 372, 3283.

[143] R. Reisfeld, V. Levchenko, T. Saraidarov, *Polym. Advan. Technol.,* **2011**, 22, 60.

[144] R. Reisfeld, M. Pietraszkiewicz, T. Saraidarov, V. Levchenko, *J. Rare Earth,* **2009**, 27, 544.

[145] R. Reisfeld, T. Saraidarov, V. Levchenko, *J. Sol-Gel Sci. Techn.,* **2009**, 50, 194.

[146] T. Saraidarov, V. Levchenko, R. Reisfeld, *Phys. Status Solidi C,* **2010**, 7, 2648.

[147] D. Brusilovsky, M. Eyal, R. Reisfeld, *Chem. Phys. Lett.,* **1988**, 153, 203.

[148] R. Reisfeld, M. Eyal, D. Brusilovsky, *Chem. Phys. Lett.,* **1988**, 153, 210.

[149] J. R. Lakowicz, K. Ray, M. Chowdhury, H. Szmacinski, Y. Fu, J. Zhang, K. Nowaczyk, *Analyst,* **2008**, 133, 1308.

[150] J. R. Lakowicz, *Plasmonics,* **2006**, 1, 5.

[151] W. G. J. H. M. van Sark, J. de Wild, J. K. Rath, A. Meijerink, R. E. I. Schropp, *Nanoscale Res. Lett.,* **2013**, 8, 81.

[152] F. Auzel, *Chem. Rev.,* **2004**, 104, 139.

[153] F. Wang, X. G. Liu, *Chem. Soc. Rev.,* **2009**, 38, 976.

[154] F. Wang, Y. Han, C. S. Lim, Y. H. Lu, J. Wang, J. Xu, H. Y. Chen, C. Zhang, M. H. Hong, X. G. Liu, *Nature,* **2010**, 463, 1061.

[155] G. Y. Chen, C. H. Yang, P. N. Prasad, *Accounts Chem. Res.,* **2013**, 46, 1474.

[156] H. Dong, L. D. Sun, C. H. Yan, *Nanoscale,* **2013**, 5, 5703.

[157] H. Lian, Z. Hou, M. Shang, D. Geng, Y. Zhang, J. Lin, *Energy,* **2013**, 57, 270.

[158] P. Gibart, F. Auzel, J. C. Guillaume, K. Zahraman, *Jpn. J. Appl. Phys.,* **1996**, 35, 4401.

[159] B. S. Richards, A. Shalav, *IEEE T. Electron. Dev.,* **2007**, 54, 2679.

[160] J. de Wild, J. K. Rath, A. Meijerink, W. G. J. H. M. van Sark, R. E. I. Schropp, *Sol. Energ. Mat. Sol. C.,* **2010**, 94, 2395.

[161] M. Liu, Y. Lu, Z. B. Xie, G. M. Chow, *Sol. Energ. Mat. Sol. C.,* **2011**, 95, 800.

[162] G. B. Shan, G. P. Demopoulos, *Adv. Mater.,* **2010**, 22, 4373.

[163] J. de Wild, A. Meijerink, J. K. Rath, W. G. J. H. M. van Sark, R. E. I. Schropp, *Sol. Energ. Mat. Sol. C,* **2010**, 94, 1919.

[164] A. Shalav, B. S. Richards, T. Trupke, K. W. Krämer, H. U. Güdel, *Appl. Phys. Lett.,* **2005**, 86, 013505.

[165] T. Trupke, A. Shalav, B. S. Richards, P. Wurfel, M. A. Green, *Sol. Energ. Mat. Sol. C.,* **2006**, 90, 3327.

[166] X. D. Zhang, X. Jin, D. F. Wang, S. Z. Xiong, X. H. Geng, Y. Zhao, *Phys. Status Solidi C,* **2010**, 7, 1128.

[167] D. F. Wang, X. D. Zhang, Y. J. Liu, C. Y. Wu, C. S. Zhang, C. C. Wei, Y. Zhao, *Chinese Phys. B,* **2013**, 22, 027801.

[168] Y. C. Chen, T. M. Chen, *J. Rare Earth,* **2011**, 29, 723.

[169] J.-l. Adam, *Chem. Rev.,* **2002**, 102, 2461.

[170] C. B. de Araújo, L. S. Menezes, G. S. Maciel, L. H. Acioli, A. S. L. Gomes, Y. Messaddeq, A. Florez, M. A. Aegerter, *Appl. Phys. Lett.,* **1996**, 68, 602.

[171] T. Catunda, L. A. O. Nunes, A. Florez, Y. Messaddeq, M. A. Aegerter, *Phys. Rev. B,* **1996**, 53, 6065.

[172] G. S. Maciel, C. B. de Araújo, Y. Messaddeq, M. A. Aegerter, *Phys. Rev. B,* **1997**, 55, 6335.

[173] L. H. Acioli, J.-T. Guo, C. B. de Araújo, Y. Messaddeq, M. Aegerter, *J. Lumin.,* **1997**, 72-74, 68.

[174] C. B. de Araújo, G. S. Maciel, L. S. Menezes, N. Rakov, E. L. Falcão-Filho, V. A. Jerez, Y. Messaddeq, *CR. Chim.,* **2002**, 5, 885.

[175] L. de Araújo, A. Gomes, C. de Araújo, Y. Messaddeq, A. Florez, M. Aegerter, *Phys. Rev. B,* **1994**, 50, 16219.

[176] I. R. Martín, V. D. Rodríguez, V. Lavín, U. R. Rodríguez-Mendoza, *J. Alloy. Compd.,* **1998**, 275-277, 345.

[177] E. Martins, C. B. de Araújo, J. R. Delben, A. S. L. Gomes, B. J. da Costa, Y. Messadeq, *Opt. Commun.,* **1998**, 158, 61.

[178] E. Pecoraro, D. F. de Sousa, R. Lebullenger, A. C. Hernandes, L. A. O. Nunes, *J. Appl. Phys.,* **1999**, 86, 3144.

[179] W. Lozano, C. B. de Araújo, C. Egalon, A. S. L. Gomes, B. J. Costa, Y. Messadeq, *Opt. Commun.,* **1998**, 153, 271.

[180] I. R. Martín, J. Méndez-Ramos, V. D. Rodríguez, J. J. Romero, J. García-Solé, *Opt. Mater.,* **2003**, 22, 327.

[181] I. R. Martín, V. D. Rodríguez, V. Lavín, U. R. Rodríguez-Mendoza, *Spectrochim. Acta A,* **1999**, 55, 941.

[182] P. Haro-González, I. R. Martín, N. E. Capuj, F. Lahoz, *Opt. Mater.,* **2010**, 32, 1349.

[183] H. Q. Wang, M. Batentschuk, A. Osvet, L. Pinna, C. J. Brabec, *Adv. Mater.,* **2011**, 23, 2675.

[184] C. Strümpel, M. McCann, G. Beaucarne, V. Arkhipov, A. Slaoui, V. Švrček, C. del Cañizo, I. Tobias, *Sol. Energ. Mat. Sol. C.,* **2007**, 91, 238.

[185] J. de Wild, A. Meijerink, J. K. Rath, W. G. J. H. M. van Sark, R. E. I. Schropp, *Energ. Environ. Sci.,* **2011**, 4, 4835.

[186] X. C. Ye, J. E. Collins, Y. J. Kang, J. Chen, D. T. N. Chen, A. G. Yodh, C. B. Murray, *Proc. Natl. Acad. Sci. USA,* **2010**, 107, 22430.

[187] Y. L. Dai, P. A. Ma, Z. Y. Cheng, X. J. Kang, X. Zhang, Z. Y. Hou, C. X. Li, D. M. Yang, X. F. Zhai, J. Lin, *ACS Nano,* **2012**, 6, 3327.

[188] S. Chen, G. H. Zhou, F. F. Su, H. L. Zhang, L. X. Wang, M. J. Wu, M. B. Chen, L. K. Pan, S. W. Wang, *Mater. Lett.,* **2012**, 77, 17.

[189] S. K. W. MacDougall, A. Ivaturi, J. Marques-Hueso, K. W. Krämer, B. S. Richards, *Opt. Express,* **2012**, 20, A879.

[190] J. C. Goldschmidt, S. Fischer, P. Löper, K. W. Krämer, D. Biner, M. Hermle, S. W. Glunz, *Sol. Energ. Mat. Sol. C.,* **2011**, 95, 1960.

[191] E. Verhagen, L. Kuipers, A. Polman, *Opt. Express,* **2009**, 17, 14586.

[192] S. Fischer, F. Hallermann, T. Eichelkraut, G. von Plessen, K. W. Krämer, D. Biner, H. Steinkemper, M. Hermle, J. C. Goldschmidt, *Opt. Express,* **2012**, 20, 271.

[193] C. Andriamiadamanana, A. Ferrier, L. Lombez, A. L. Joudrier, N. Naghavi, P. Ghenuche, N. Bardou, J. L. Pelouard, S. Collin, F. Pelle, J. F. Guillemoles, *Proc. SPIE,* **2012**, 8256, 825608.

[194] B. M. van der Ende, L. Aarts, A. Meijerink, *Phys. Chem. Chem. Phys.,* **2009**, 11, 11081.

[195] P. Vergeer, T. Vlugt, M. Kox, M. den Hertog, J. van der Eerden, A. Meijerink, *Phys. Rev. B,* **2005**, 71, 014119.

[196] L. J. Borrero-Gonzalez, G. Galleani, D. Manzani, L. A. O. Nunes, S. J. L. Ribeiro, *Opt. Mater.,* **2013**, 35, 2085.

[197] Y. Xu, X. Zhang, S. Dai, B. Fan, H. Ma, J.-l. Adam, J. Ren, G. Chen, *J. Phys. Chem. C.,* **2011**, 115, 13056.

[198] K. Deng, X. Wei, X. Wang, Y. Chen, M. Yin, *Appl. Phys. B-Lasers O.,* **2011**, 102, 555.

[199] Q. J. Chen, W. J. Zhang, X. Y. Huang, G. P. Dong, M. Y. Peng, Q. Y. Zhang, *J. Alloy. Compd.,* **2012**, 513, 139.

[200] A. Guille, A. Pereira, C. Martinet, B. Moine, *Opt. Lett.,* **2012**, 37, 2280.

[201] B. M. van der Ende, L. Aarts, A. Meijerink, *Adv. Mater.,* **2009**, 21, 3073.

[202] J. T. van Wijngaarden, S. Scheidelaar, T. J. H. Vlugt, M. F. Reid, A. Meijerink, *Phys. Rev. B,* **2010**, 81, 155112.

[203] D. Serrano, A. Braud, J. L. Doualan, P. Camy, A. Benayad, V. Ménard, R. Moncorgé, *Opt. Mater.,* **2011**, 33, 1028.

[204] G. Lakshminarayana, H. Yang, S. Ye, Y. Liu, J. Qiu, *J. Phys. D Appl. Phys.,* **2008**, 41, 175111.

[205] X. F. Liu, Y. Teng, Y. X. Zhuang, J. H. Xie, Y. B. Qiao, G. P. Dong, D. P. Chen, J. R. Qiu, *Opt. Lett.,* **2009**, 34, 3565.

[206] J. J. Eilers, D. Biner, J. T. van Wijngaarden, K. Krämer, H. U. Güdel, A. Meijerink, *Appl. Phys. Lett.,* **2010**, 96, 151106.

[207] L. J. Borrero-Gonzalez, L. A. Nunes, *J. Phys. Condens. Mat.,* **2012**, 24, 385501.

[208] J. J. Zhou, Y. Teng, S. Ye, G. Lin, J. R. Qiu, *Opt. Mater.,* **2012**, 34, 901.

[209] P. Song, C. Jiang, *AIP Adv.,* **2012**, 2, 042130.

[210] P. Escribano, B. Julián-López, J. Planelles-Aragó, E. Cordoncillo, B. Viana, C. Sanchez, *J. Mater. Chem.,* **2008**, 18, 23.

[211] K. Binnemans, *Chem. Rev,* **2009**, 109, 4283.

[212] J.-C. G. Bünzli, S. V. Eliseeva, *J. Rare Earth.,* **2010**, 28, 824.

[213] S. Sivakumar, P. R. Diamente, F. C. van Veggel, *Chem.- Eur. J.,* **2006**, 12, 5878.

[214] S. K. Singh, A. K. Singh, S. B. Rai, *Nanotechnology,* **2011**, 22, 275703.

[215] W. Q. Zou, C. Visser, J. A. Maduro, M. S. Pshenichnikov, J. C. Hummelen, *Nat. Photonics,* **2012**, 6, 560.

[216] X. J. Xie, X. G. Liu, *Nat. Mater.,* **2012**, 11, 842.

[217] G. Griffini, M. Levi, S. Turri, *Prog. Org. Coat.,* **2014**, 77, 528.

[218] W. Zhou, M. C. Wang, X. J. Zhao, *Sol. Energy,* **2015**, 115, 569.

[219] K. R. McIntosh, N. Yamada, B. S. Richards, *Appl. Phys. B,* **2007**, 88, 285.

[220] O. Y. Edelenbosch, M. Fisher, L. Patrignani, W. G. J. H. M. van Sark, A. J. Chatten, *Opt. Express,* **2013**, 21, A503.

[221] H. J. Hovel, R. T. Hodgson, J. M. Woodall, *Sol. Energ. Mater.,* **1979**, 2, 19.

[222] T. Jin, S. Inoue, K. Machida, G. Adachi, *J. Electrochem. Soc.,* **1997**, 144, 4054.

[223] S. M. Geyer, J. M. Scherer, N. Moloto, F. B. Jaworski, M. G. Bawendi, *ACS Nano,* **2011**, 5, 5566.

[224] S. D. Hodgson, W. S. M. Brooks, A. J. Clayton, G. Kartopu, V. Barrioz, S. J. C. Irvine, *Nano Energy,* **2013**, 2, 21.

[225] T. Fukuda, S. Kato, E. Kin, K. Okaniwa, H. Morikawa, Z. Honda, N. Kamata, *Opt. Mater.,* **2009**, 32, 22.

[226] A. C. Pan, C. del Canizo, E. Canovas, N. M. Santos, J. P. Leitão, A. Luque, *Sol. Energ. Mat. Sol. C,* **2010**, 94, 1923.

[227] J. Liu, K. Wang, W. Zheng, W. Huang, C. H. Li, X. Z. You, *Prog. Photovoltaics,* **2013**, 21, 668.

[228] A. Le Donne, M. Acciarri, D. Narducci, S. Marchionna, S. Binetti, *Prog. Photovoltaics,* **2009**, 17, 519.

[229] R. Rothemund, *Sol. Energ. Mat. Sol. C.,* **2014**, 120, 616.

[230] U. Schubert, N. Husing, A. Lorenz, *Chem. Mater.,* **1995**, 7, 2010.

[231] V. de Zea Bermudez, L. D. Carlos, L. Alcácer, *Chem. Mater.,* **1999**, 11, 569.

[232] V. T. Freitas, P. P. Lima, R. A. S. Ferreira, E. Pecoraro, M. Fernandes, V. de Zea Bermudez, L. D. Carlos, *J. Sol-Gel Sci. Techn.,* **2013**, 65, 83.

[233] M. Fernandes, V. de Zea Bermudez, R. A. S. Ferreira, L. D. Carlos, N. V. Martins, *J. Lumin.,* **2008**, 128, 205.

[234] M. Fernandes, V. de Zea Bermudez, R. A. S. Ferreira, L. D. Carlos, A. Charas, J. Morgado, M. M. Silva, M. J. Smith, *Chem. Mater.,* **2007**, 19, 3892.

[235] R. G. Charles, R. C. Ohlmann, *J. Inorg. Nucl. Chem.,* **1965**, 27, 255.

[236] C. Molina, K. Dahmouche, Y. Messaddeq, S. J. L. Ribeiro, M. A. P. Silva, V. de Zea Bermudez, L. D. Carlos, *J. Lumin.,* **2003**, 104, 93.

[237] M. Fischer, J. Georges, *Chem. Phys. Lett.,* **1996**, 260, 115.

[238] W. A. Shurcliff, R. C. Jones, *J. Opt. Soc. Am.,* **1949**, 39, 912.

[239] J. W. E. Wiegman, E. van der Kolk, *Sol. Energ. Mat. Sol. C.,* **2012**, 103, 41.

[240] M. D. Hughes, C. Maher, D.-A. Borca-Tasciuc, D. Polanco, D. Kaminski, *Renew. Energ.,* **2013**, 52, 266.

[241] T. Dienel, C. Bauer, I. Dolamic, D. Bruhwiler, *Sol. Energy,* **2010**, 84, 1366.

[242] D. Şahin, B. Ilan, D. F. Kelley, *J. Appl. Phys.,* **2011**, 110, 033108.

[243] X. Sheng, L. Shen, T. Kim, L. F. Li, X. R. Wang, R. Dowdy, P. Froeter, K. Shigeta, X. L. Li, R. G. Nuzzo, N. C. Giebink, J. A. Rogers, *Adv. Energy Mater.,* **2013**, 3, 991.

[244] J. L. Banal, K. P. Ghiggino, W. W. H. Wong, *Phys. Chem. Chem. Phys.,* **2014**, 16, 25358.

[245] M. Pravettoni, D. J. Farrell, A. J. Chatten, R. Bose, R. P. Kenny, K. W. J. Barnham, *External quantum efficiency measurements of luminescent solar concentrators: a study of the impact of backside reflector size and shape*, in 24th European Photovoltaic Solar Energy Conference, **2009**, Hamburg, Germany.

[246] J.-M. Liu, *Principles of Photonics*, **2016**, Cambridge University Press, Cambridge, United Kingdom.

[247] G. Colantuono, A. Buckley, R. Erdélyi, *J. Lightwave Technol.,* **2013**, 31, 1033.

[248] C. Wang, H. Abdul-Rahman, S. P. Rao, *Energ. Buildings,* **2010**, 42, 717.

[249] E.-H. Banaei, A. F. Abouraddy, *Prog. Photovolt: Res. Appl.,* **2014**, 23, 403.

[250] C. M. S. Vicente, R. Venkatachaam, B. M. Ferreira, P. G. Marques, C. A. F. Marques, E. Pecoraro, L. D. Carlos, P. S. André, R. A. S. Ferreira, *Phys. Status Sol. - R.,* **2011**, 5, 280.

[251] T. X. Wang, B. Yu, B. Chen, Z. J. Hu, Y. H. Luo, G. Zou, Q. J. Zhang, *J. Optics-UK,* **2013**, 15, 055709.

[252] M. Fox, *Optical Properties of Solids*, **2001**, Oxford University Press, New York.

[253] V. R. Fernandes, C. M. S. Vicente, N. Wada, P. S. André, R. A. S. Ferreira, *Opt. Express,* **2010**, 18, 16580.

[254] J. H. Kuang, P. C. Chen, Y. C. Chen, *Sensors,* **2010**, 10, 101998.

[255] S. S. Nobre, P. P. Lima, L. Mafra, R. A. S. Ferreira, R. O. Freire, L. S. Fu, U. Pischel, V. de Zea Bermudez, O. L. Malta, L. D. Carlos, *J. Phys. Chem. C,* **2007**, 111, 3275.

[256] J.-C. G. Bünzli, *Chem. Rev.,* **2010**, 110, 2729.

[257] R. Reisfeld, D. Shamrakov, C. Jorgensen, *Sol. Energ. Mat. Sol. C.,* **1994**, 33, 417.

[258] V. Wittwer, W. Stahl, A. Goetzberger, *Sol. Energ. Mater.,* **1984**, 11, 187.

[259] A. I. Salem, A. F. Mansour, N. M. El-Sayed, A. H. Bassyouni, *Renew. Energ.,* **2000**, 20, 95.

[260] C. H. Chou, J. K. Chuang, F. C. Chen, *Sci. Rep.-UK,* **2013**, 3, 2244.

[261] S. R. Wilton, M. R. Fetterman, J. J. Low, G. J. You, Z. Y. Jiang, J. Xu, *Opt. Express,* **2014**, 22, A35.

[262] X. M. Hu, R. D. Kang, Y. Y. Zhang, L. G. Deng, H. Z. Zhong, B. S. Zou, L. J. Shi, *Opt. Express,* **2015**, 23, A858.

[263] K. R. McIntosh, G. Lau, J. N. Cotsell, K. Hanton, D. L. Batzner, F. Bettiol, B. S. Richards, *Prog. Photovolt: Res. Appl.,* **2009**, 17, 191.

[264] R. Sasai, N. Iyi, T. Fujita, F. L. Arbeloa, V. M. Martinez, K. Takagi, H. Itoh, *Langmuir,* **2004**, 20, 4715.

[265] A. Alessi, M. Salvalaggio, G. Ruzzon, *J. Lumin.,* **2013**, 134, 385.

[266] S. C. Nunes, C. B. Ferreira, J. Hummer, R. A. S. Ferreira, L. D. Carlos, P. Almeida, V. de Zea Bermudez, *J. Mater. Chem. C,* **2013**, 1, 2290.

[267] M. G. Kuzyk, *Polymer Fiber Optics: Materials, Physics, and Applications*, **2007**, Taylor & Francis Group, LLC, Boca Raton, Florida.

[268] N. C. Giebink, G. P. Wiederrecht, M. R. Wasielewski, *Nat. Photonics,* **2011**, 5, 695.

[269] G. Smestad, H. Ries, R. Winston, E. Yablonovitch, *Sol. Energ. Mater.,* **1990**, 21, 99.

[270] E. Yablonovitch, *J. Opt. Soc. Am.,* **1980**, 70, 1362.

[271] C. Wang, H. Abdul-Rahman, S. P. Rao, *J. Energ. Eng.-Asce,* **2010**, 136,

[272] C. Wang, H. Abdul-Rahman, S. P. Rao, *Int. J. Energ. Res.,* **2010**, 34, 1372.

[273] C. M. S. Vicente, P. P. Lima, V. D. Bermudez, L. D. Carlos, P. S. Andre, R. A. S. Ferreira, *Opt. Express,* **2014**, 22, 27159.

[274] S. Lee, Y. Lee, J. Park, D. Choi, *Nano Energy,* **2014**, 9, 88.

[275] C. L. Mulder, P. D. Reusswig, A. M. Velázquez, H. Kim, C. Rotschild, M. A. Baldo, *Opt. Express,* **2010**, 18, A79.

[276] C. L. Mulder, P. D. Reusswig, A. P. Beyler, H. Kim, C. Rotschild, M. A. Baldo, *Opt. Express,* **2010**, 18, A91.

[277] J. Gjessing, E. S. Marstein, A. Sudbo, *Opt. Express,* **2010**, 18, 5481.

[278] C. Molina, P. J. Moreira, R. R. Gonçalves, R. A. S. Ferreira, Y. Messaddeq, S. J. L. Ribeiro, O. Soppera, A. P. Leite, P. V. S. Marques, V. de Zea Bermudez, L. D. Carlos, *J. Mater. Chem.,* **2005**, 15, 3937.

[279] D. C. Oliveira, A. G. Macedo, N. J. O. Silva, C. Molina, R. A. S. Ferreira, P. S. André, K. Dahmouche, V. D. Bermudez, Y. Messaddeq, S. J. L. Ribeiro, L. D. Carlos, *Chem. Mater.,* **2008**, 20, 3696.

[280] C. Tummeltshammer, A. Taylor, A. J. Kenyon, I. Papakonstantinou, *Sol. Energ. Mater. Sol. C.,* **2016**, 144, 40.

[281] J. Yoon, L. F. Li, A. V. Semichaevsky, J. H. Ryu, H. T. Johnson, R. G. Nuzzo, J. A. Rogers, *Nat. Commun.,* **2011**, 2, 343.

[282] D. Chemisana, *Renew. Sust. Energ. Rev.,* **2011**, 15, 603.

[283] C. Sapia, *Sol. Energy,* **2013**, 89, 113.

[284] *Soofa - my urban hub,* Accessed 7th September 2016, Available from: http://www.soofa.co/.

[285] I.-G. Lim, S.-W. Kang, C.-h. Hyoung, K.-H. Park, S.-E. Kim, T.-W. Kang, H.-I. Park, J.-H. Hwang, B.-G. Choi, T.-Y. Kang, J.-B. Kim, K.-S. Kim, M.-A. Chung, US20140015470 A1, **2014**.

[286] G. Kocher-Oberlehner, M. Bardosova, M. Pemble, B. S. Richards, *Sol. Energ. Mat. Sol. C.,* **2012**, 104, 53.

[287] B. P. Jelle, C. Breivik, *Energy Procedia,* **2012**, 20, 68.

[288] K. Binnemans, P. T. Jones, B. Blanpain, T. Van Gerven, Y. X. Yang, A. Walton, M. Buchert, *J. Clean. Prod.,* **2013**, 51, 1.

[289] J. C. G. Bünzli, S. V. Eliseeva, *Chem. Sci.,* **2013**, 4, 1939.

[290] S. V. Eliseeva, J.-C. G. Bünzli, *New J. Chem.,* **2011**, 35, 1165.

[291] M. A. de Boer, K. Lammertsma, *ChemSusChem,* **2013**, 6, 2045.